Study of the $^{7}\mathrm{Be}(d,p)^{8}\mathrm{Be}$ Reaction and its Impact on the Cosmological Lithium Problem

Azusa Inoue

Doctor of Philosophy

Department of Physics,
Graduate School of Science,
OSAKA UNIVERSITY

February 2024

Abstract

The aim of the thesis is to potentially resolve the Cosmological Lithium Problem (CLP) with the cross-section measurements of the $^{7}\mathrm{Be}(d,p)^{8}\mathrm{Be}$ reaction. The CLP is a well-known unsolved issue in astrophysics that is an overestimation of the primordial $^{7}\mathrm{Li}$ abundance in the standard Big Bang nucleosynthesis (BBN) model compared to astrophysical observations. The majority of $^{7}\mathrm{Li}$ nuclei were produced by the electron capture decay ($t_{1/2} = 53.22$ days $= 4.6 \times 10^{6}$ seconds) of $^{7}\mathrm{Be}$. $^{7}\mathrm{Be}$ nuclei were considered to be produced in several hundred seconds during the BBN, resulting in a timescale difference of 10^{4} between the $^{7}\mathrm{Li}$ and $^{7}\mathrm{Be}$ productions.

One of the possible scenarios to resolve the CLP is that $^{7}\mathrm{Be}$ nuclei were more destroyed during the BBN with a lesser abundance of $^{7}\mathrm{Li}$ than the BBN model prediction. The $^{7}\mathrm{Be}(d,p)^{8}\mathrm{Be}$ reaction is focused in this thesis following a theoretical suggestion that the reaction played a significant role in the destruction of $^{7}\mathrm{Be}$ nuclei during the BBN [1]. The measurement of the absolute cross section in the Big Bang energy region ($E_{c.m.} = 0.1 - 0.4$ MeV) was crucial for understanding the nuclear reactions in the primordial universe.

We produced a radioactive $^{7}\mathrm{Be}$ target and measured the $^{7}\mathrm{Be}(d,p)^{8}\mathrm{Be}$ reaction cross section in the BBN energy region at the tandem facility of Kobe University. A 2.36 MeV proton beam irradiated a natural Li target with a thickness of $1.60\ \mathrm{mg/cm^{2}}$ ($= 30.0\,\mu m$), transmuting $^{7}\mathrm{Li}$ nuclei to $^{7}\mathrm{Be}$ through the $^{7}\mathrm{Li}(p,n)^{7}\mathrm{Be}$ reaction. 2.80×10^{13} $^{7}\mathrm{Be}$ nuclei were produced in the Li host target by two days of the proton irradiation. Following the target production, a deuteron beam was accelerated to energies of 1.6 and 0.6 MeV to measure the $^{7}\mathrm{Be}(d,p)^{8}\mathrm{Be}$ reaction cross section. The outgoing proton's energy and yield were measured by two sets of four-layered silicon telescopes placed at scattering angles of 45 and 30 degrees.

The thick target analysis method was applied to obtain the cross sections. The measured cross sections were 0.89 ± 0.18 (0.76 ± 0.24) mb at $\theta_{\rm lab} = 45$ $(30)^\circ$ at $E_{c.m.} = 0.35$ MeV and 0.17 ± 0.13 (0.21 ± 0.20) mb at $\theta_{\rm lab} = 45$ $(30)^\circ$ at $E_{c.m.} = 0.12$ MeV. The cross section was obtained at the lowest energy of $E_{c.m.} = 0.12$ MeV with the highest sensitivity compared to the available data [2, 3, 4]. The impact of the measured cross sections on the CLP was found to be small.

Contents

Chapter 1

Astrophysical Motivation

1.1 History of Cosmology

In modern cosmology, the consensus widely acknowledges the expansion of the universe. However, in the early 1900s, the concept of the universe undergoing expansion had yet to attain consensus. The predominant perspective of the era posited a static and unchanging universe. In the 1920s, E. Hubble measured the redshifts [1] of distant galaxies and noticed an interesting behavior: the galaxies moved away from us [5]. Hubble discovered a proportional relationship between the receding velocity V at which galaxies moved away from us and the distance r to galaxies: $V = Hr$. Here, H is a proportionality constant called the Hubble constant, and this proportional relationship is called Hubble's law of galactic recession. Hubble's discovery was a crucial indicator of the universe's expansion. In the 1940s, the primary theory formulated by G. Gamow in response to Hubble's observations was the Big Bang Theory [6]. According to this theory, the universe initiated its expansion from an extremely high-temperature and high-density state, ultimately evolving into the expansive cosmos observed today. Concurrently, F. Hoyle proposed the steady-state cosmology [7] assumes that the universe does not change over time and remains constant for eternity; however, Hubble's observations favored the Big Bang theory over the steady-state cosmology.

[1]The redshift of a galaxy represents one of the observed phenomena grounded in the Doppler effect. The redshift refers to the fact that the observed light appears red because the wavelength of the light is lengthened, and the light is shifted to a lower frequency (red light).

In the 1960s, A. Penzias and R. Wilson accidentally detected unidentified radio waves coming from all directions in the sky [8] and subsequently identified this radiation as the Cosmic Microwave Background (CMB). The CMB represented a faint glow of microwaves uniformly distributed throughout the universe, with a confirmed temperature of approximately 2.7 K. The existence of the CMB was a pivotal discovery that supported the theory of the expansion of the universe and the Big Bang, as detailed in 1.4. Subsequent observations by NASA's COBE satellite, launched in 1989, revealed that the CMB exhibited characteristics of perfect blackbody radiation, with a temperature of 2.728 $\pm$ 0.004 K [9, 10]. The observation of the Cosmic Microwave Background (CMB) has strongly supported the Big Bang cosmology, and this theory is widely accepted in contemporary astrophysics and cosmology.

1.2 Standard Big Bang Nucleosynthesis

Standard Big Bang Nucleosynthesis (SBBN) refers to the processes in the early universe as the universe expanded from an exceedingly high-temperature and high-density state, giving rise to elementary particles and ultimately leading to the synthesis of lighter elements. Primordial Big Bang nucleosynthesis (BBN) commenced when the universe was 3 minutes old and concluded in less than half an hour due to the low temperature and density conditions prevailing in the expanding universe.

Right after the Big Bang, the conditions of the primordial universe were extremely hot and dense, and particles like protons and neutrons had not yet formed. Instead, the universe existed in a state known as quark-gluon plasma, where fundamental particles such as quarks and gluons roamed freely. Approximately 10^{-6} seconds after the cosmic inception, the universe's temperature dropped to about 10^{13} K. At that time, quarks could no longer exist independently because they had reached a threshold of energy required for binding, initiating the formation of protons and neutrons. When the temperature was around ~ 11.6 GK, the universe was filled with radiation such as photons p, neutrinos n, antineutrinos, electrons e^{-}, and positrons e^{+}. Protons, neutrons, electrons, positrons, electron neutrinos ν_{e}, and electron neutrinos $\overline{\nu}_{\mathrm{e}}$ began interacting through weak interactions.

In the early universe, following reactions 1.1, 1.2, 1.3 were in equilibrium.

$$n + \nu_{\mathrm{e}} \leftrightarrow p + e^{-}. \tag{1.1}$$

$$n \leftrightarrow p + e^{-} + \overline{\nu}_{\mathrm{e}}. \tag{1.2}$$

$$n + e^{+} \leftrightarrow p + \overline{\nu}_{\mathrm{e}}. \tag{1.3}$$

As the universe expanded and the temperature decreased, the neutron-to-proton conversion reaction 1.2 became dominant, and the equilibrium in reactions 1.1, 1.2, 1.3 began to collapse.

The universe continued to expand, and when the temperature dropped from approximately 10^9 K to 10^{10} K, the reaction between neutrons and protons caused the Big Bang nuclear fusion. Neutrons and protons combined to produce deuterium (D), and deuterons and protons reacted to produce helium-3 ($^3\mathrm{He}$). $^3\mathrm{He}$ reacted with protons and produced helium-4 ($^4\mathrm{He}$).

Elements heavier than $^4\mathrm{He}$ were rarely produced during early Big Bang nucleosynthesis. The rapid drop in the temperature of the universe meant that particles no longer possessed sufficient kinetic energy to overcome the Coulomb barrier, making it difficult for reactions to occur.

When helium was formed, most of the neutrons were absorbed into the formation of $^4\mathrm{He}$ nuclei.

Since the neutron half-life is about 15 minutes, neutrons decayed back into protons if they were not involved in reactions. A surplus of photons (proportional to the number of electrons and positrons) hindered the formation of atomic nuclei, causing a delay in nucleosynthesis [11, 12]. The number of neutrons could be decreased during the delay (beyond 15 minutes). In cases of high photon density, helium nuclei could be decreased, and the ratio of hydrogen nuclei (single protons) to helium could be changed. The ratio of photons to baryons (protons and neutrons) determined the proportions in which elements were created. In the description of the early universe, this baryon-to-photon ratio was a crucial factor. The baryon-photon ratio, denoted as η, is expressed by the following Eq. (1.4):

$$\eta \equiv \frac{n_{\mathrm{b}}}{n_{\gamma}}. \tag{1.4}$$

Primordial abundances of light nuclides have been calculated based on variations in the baryon-to-photon ratio.

1.3 Astrophysical Observation

The study of light element abundances involved astrophysical observations.

The abundance of $^4\mathrm{He}$ during Big Bang nucleosynthesis was primarily determined through observations in external galaxies' $\mathrm{H\,II}$ region, where stars formed and emitted radiation. In the $\mathrm{H\,II}$ region, gas was excited by the stars' radiation, leading to helium emission at specific wavelengths. Analyzing the observed spectrum allowed us to investigate the intensity and shape of helium emission lines. This analysis helped us understand the abundance and distribution of helium. Recently, new observations were added to determine the $^4\mathrm{He}$ abundance, and those data reduced the uncertainty and led to a better-defined value of the $^4\mathrm{He}$ abundance, $^4\mathrm{He}/\mathrm{H} = 0.2449 \pm 0.0040$ [13, 14]. Another value, $^4\mathrm{He}/\mathrm{H} = 0.2515 \pm 0.0017$, was also reported by [15, 16]. Note that those differences came from how the helium abundance was determined from individual stellar objects and the sample selection [17].

The method to determine the abundance of D was observing the redshift absorption lines of quasars, which are very distant and bright galaxies. Light from selected quasars passed through the gas, and dust in the universe absorbed the light. Absorption lines were dark parts of the spectrum formed when substances absorbed light. Deuterium, possessing the property of absorbing light at a specific wavelength, allowed for estimating its abundance. Hydrogen absorption lines were also measured, allowing the D/H ratio to be determined. Since 1997, absorption lines from quasars have been measured to determine the D abundance. However, systematic errors were not accounted for, and the uncertainty needed to be clarified. In 2012, [18] reported precise observational results, referring to previous measurements, and the D abundance was determined as $\mathrm{D}/\mathrm{H} = (2.53 \pm 0.04) \times 10^{-5}$.

As in the case of $^4\mathrm{He}$, the abundance of Li was assessed by analyzing spectra obtained from low-metallicity stars. Li was produced not only during Big Bang nucleosynthesis but also through astrophysical processes that occurred after the BBN. The contribution of astrophysical reactions after BBN to Li production was considered negligible in low-metallicity stars. Therefore, low-metallicity stars were suitable objects for determining the primordial abundance of Li during Big Bang nucleosynthesis. In 1982, the abundance of Li was initially determined based on measurements from 11 stars [19]. Since then, spectra observations from ten times as many stars have been conducted. [20] reported that the abundance ratio of lithium was $\mathrm{Li/H} = (1.6 \pm 0.3) \times 10^{-10}$. According to [21]'s report, $^{6}\mathrm{Li}/^{7}\mathrm{Li} \lesssim 0.1$ suggested that the abundance ratio of $\mathrm{Li/H} = (1.6 \pm 0.3) \times 10^{-10}$ was nearly equivalent to that of $^{7}\mathrm{Li}$.

1.4 Cosmic Microwave Background Measurement

The Cosmic Microwave Background (CMB) is faint blackbody radiation that is nearly uniform across the entire universe with slight directional variations. The Wilkinson Microwave Anisotropy Probe (WMAP) [22] is a cosmic telescope designed to precisely measure the CMB.

After the Big Bang, the universe existed in a state of extremely high temperature and density. During this phase, atoms were ionized, and electrons and protons were separated, resulting in a plasma state. In this state, photons were unable to travel through the universe in a straight line. About 380,000 years after the Big Bang, the universe's temperature had cooled to around 3000 K. At this point, the universe had cooled sufficiently for stable hydrogen atoms to form, marking a process known as recombination. Recombination led to the formation of neutral atoms, allowing photons to propagate freely. The CMB represented the residual radiation of photons from the recombination moment.

Through high-precision measurements, the temperature of the CMB has been determined to be 2.728 $\pm$ 0.004 K [9, 10]. As the CMB depicted the residual radiation of photons, the determination of this temperature allowed for the prediction of the photon quantity during recombination [9, 10]. Additionally, constraints on the baryon number have been obtained by analyzing the angular spectrum and anisotropy of the CMB. Determining the photon and baryon numbers led to determining the baryon-to-photon ratio as $\eta = (6.16 \pm 0.17) \times 10^{-10}$ [23, 24], a parameter in the standard Big Bang Nucleosynthesis model.

1.5 The Cosmological Lithium Problem

Fig. 1.1 shows the abundance of light elements as a function of the baryon-to-photon ratio. Fig. 1.1 compares theoretical calculations (in blue), observations (in green), and the baryon-to-photon ratio (in orange) within the vertical band. As depicted in Fig. 1.1, the theoretical calculations successfully replicate the observed values for $^4\mathrm{He}$ and $^3\mathrm{D}$. However, for $^7\mathrm{Li}$, the result of the BBN calculation does not align with the observed values. The theoretical estimation was approximately three times higher than the observed value, leading to what is known as the Cosmological Lithium Problem (CLP). This discrepancy is notably significant, especially considering the well-reproduced abundances of other light nuclei. The overestimation of the primordial abundance of $^7\mathrm{Li}$ in the standard Big Bang Nucleosynthesis (BBN) model remains a major unresolved issue in modern astrophysics.

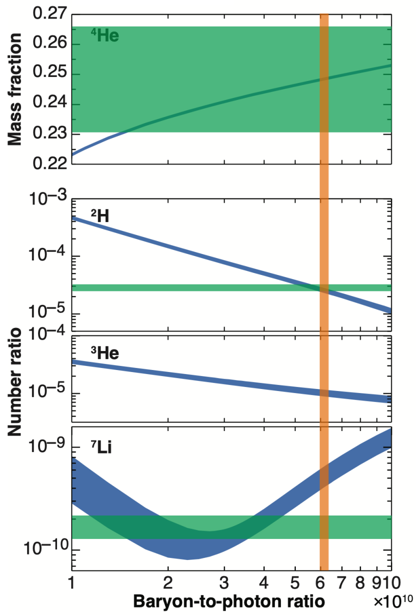

Fig. 1.1: This figure depicts the abundance ratio of elements as a function of the baryon-to-photon ratio [25, 17]. The blue curves are the theoretical calculation expressing each nuclide abundance ratio as a function of the baryon-photon ratio. The green regions show observed abundances derived from observations of low-metallicity stars. In recent years, the baryon-to-photon ratio has been determined with high precision by measurements of the CMB, as depicted by the vertical orange bar. Comparing the theoretical calculations and observed values, we see overlaps in values for ^{4}He and ^{3}D, but not for ^{7}Li. The theoretical calculation values are estimated to be approximately three times larger than the observed values.

1.6 $^{7}\mathrm{Li}$ Production

Primordial BBN began when the universe was 3 minutes old and ended less than half an hour later. The main synthesis of ^{7}Li was the electron-capturing decay of $^{7}\mathrm{Be}$, which remains after the universe cools and nuclear reactions end. $^{7}\mathrm{Be}$ nuclei were produced during the BBN, and it took just several hundred to several thousand seconds (Fig. 1.2). The electron capture decay half-life of $^{7}\mathrm{Be}$, 53.22 days [26] = 5 million seconds, was much longer than the timescale of the production of light nuclei after the Big Bang.

Thus, one possible scenario to resolve the CLP is that $^{7}\mathrm{Be}$ was destroyed in the epoch of nucleosynthesis. All of those nuclear reaction cross sections that destroy ^{7}Be have not been thoroughly constrained by experimental measurements.

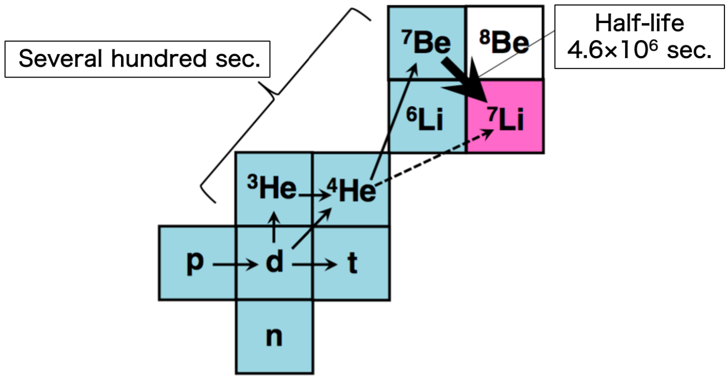

Fig. 1.2: Light nuclei were produced in several hundred seconds following the Big Bang. ^{7}Li was produced by the electron capture decay of ^{7}Be. The β decay half-life of ^{7}Be was 53.22 days (= 4.6×10^6 seconds), much longer than the timescale of BBN.

1.7 Destructive Processes of ^{7}Be

Several destructive reactions involving ^{7}Be were investigated. The $^7\mathrm{Be}(n,\alpha)^4\mathrm{He}$ reaction cross section was studied by M. Barbagallo *et al.* [27], T. Kawabata *et al.* [28], and L. Damone *et al.* [29], using a neutron beam. However, it was concluded that the $^7\mathrm{Be}(n,\alpha)^4\mathrm{He}$ reaction was insignificant to resolve the CLP. The $^7\mathrm{Be}+n$ reaction was also explored by S. Hayakawa *et al.* [30], where we identified both the $^7\mathrm{Li}+p+p$ and the $\alpha+\alpha+p$ exit channels. The $^7\mathrm{Be}(n,p_1)$ reaction led to a 10% reduction in the emitted ^{7}Li abundance comparing without the $^7\mathrm{Be}(n,p_1)$ reaction. We focused on the $^7\mathrm{Be}(d,p)^8\mathrm{Be}$ reaction since the contribution from $^7\mathrm{Be}(d,p)^8\mathrm{Be}$ was suggested to be large [1]. We measured the $^7\mathrm{Be}(d,p)^8\mathrm{Be}$ reaction with a ^{7}Be target since the available data were not sufficient enough in accuracy in the Big Bang energy region ($E_{c.m.} = 0.1 - 0.4$ MeV (0.8 GK)) [2, 3].

1.8 References of $^7\mathrm{Be}(d, p)$ Measurement

Several data points from the $^7\mathrm{Be}(d, p)^8\mathrm{Be}$ reaction cross section are available. Fig. 1.3 shows the existing data, wherein the triangular points (▲, ▼) represent measurements by R. W. Kavanagh *et al.* [2]. These measurements were conducted with forward kinematics, employing a deposited $^7\mathrm{Be}$ target. The deuteron incident energy was systematically varied to obtain this data, and the resulting cross sections were precisely measured. However, the cross sections were obtained at energies above the Big Bang nucleosynthesis region.

The data presented by C. Angulo *et al.* [3] in Fig. 1.3, marked with star symbol points ($*$), was obtained through inverse kinematics by employing a $^7\mathrm{Be}$ beam directed at a CD_2 foil target. Despite reaching the cross section relevant to the Big Bang energy region, a detailed examination of the structure within this energy region has not been conducted.

Our experiment was specifically designed to explore the details within the Big Bang energy region. We aimed for a resolution of $\Delta E_{c.m.} \sim 200$ keV within the center of mass system energy. Since the initiation of our project, data submitted by N. Rijal *et al.* [4], depicted as squares (■) in Fig. 1.3, has become available. This data was obtained through inverse kinematics, using $^7\mathrm{Be}$ as a beam and irradiating an active-gas target.

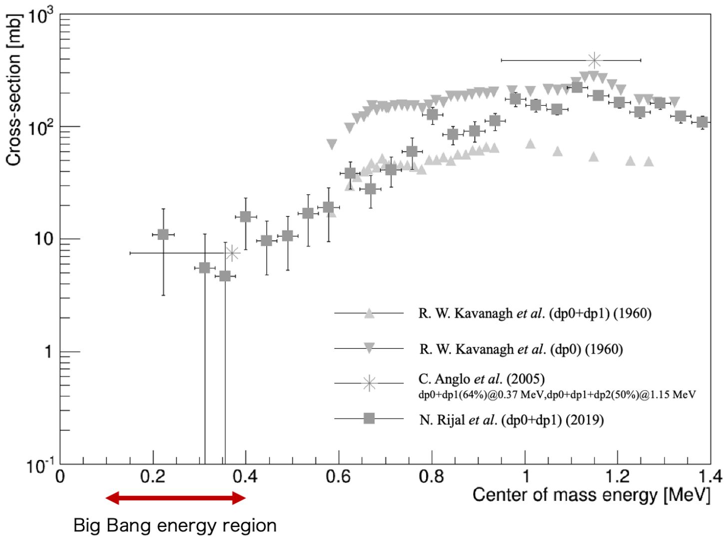

Fig. 1.3: Reference data of the $^7\mathrm{Be}(d,p)^8\mathrm{Be}$ reaction cross sections. The triangular points (▲, ▼) are from R. W. Kavanagh [2]. The star symbol points ($*$) are from C. Angulo *et al.* [3]. The square points are from N. Rijal *et al.* [4]. Those data were plotted by the author.

1.9 Measurement of $^7\mathrm{Be}(d,p)^8\mathrm{Be}$ Reaction in this Study

In this study, we measured the $^7\mathrm{Be}(d,p)^8\mathrm{Be}$ reaction using the radioactive $^7\mathrm{Be}$ target in normal kinematics (refer to 2.1 for the details on the $^7\mathrm{Be}$ target production method). Incident deuteron energies E_d were $1.6\ \mathrm{MeV}$ and $0.6\ \mathrm{MeV}$.

Chapter 2

Experimental Techniques

The distinctive features of our measurement were using a radioactive $^{7}\mathrm{Be}$ target and the thick target method. The radioactive $^{7}\mathrm{Be}$ target was enabled to measure the $^{7}\mathrm{Be}(d,p)^{8}\mathrm{Be}$ reaction in normal kinematics. The thick target method has made it possible to conduct nuclear reaction measurements at low energy bands ($E_{c.m.} = 0.1 - 0.4\ \mathrm{MeV}$), such as the energy of Big Bang nucleosynthesis.

The details of $^{7}\mathrm{Be}$ target production and the technique for measuring the $^{7}\mathrm{Be}(d,p)^{8}\mathrm{Be}$ reaction at low energy ($E_{c.m.} = 0.1 - 0.4\ \mathrm{MeV}$) are described below.

2.1 Activation Method

$^{7}\mathrm{Be}$ is known as a radioactive nucleus with a half-life of 53.22 days [26]. A distinctive approach to this experiment was producing a radioactive $^{7}\mathrm{Be}$ target. Natural lithium (with a $^{7}\mathrm{Li}$ abundance of 92.5%) was used as the host target material. The lithium target was irradiated with a proton beam. $^{7}\mathrm{Li}$ nuclei in the lithium target were activated and transmuted to $^{7}\mathrm{Be}$ through the $^{7}\mathrm{Li}(p,\ n)^{7}\mathrm{Be}$ reaction. The technique to produce the radioactive target was called an activation method [31]. Fig. 2.1 schematically illustrates the activation process. The orange circles represent $^{7}\mathrm{Li}$ nuclei, while the dark-blue circles depict the $^{7}\mathrm{Be}$ nuclei formed when the proton beam irradiates the lithium target, activating the $^{7}\mathrm{Li}$ nuclei.

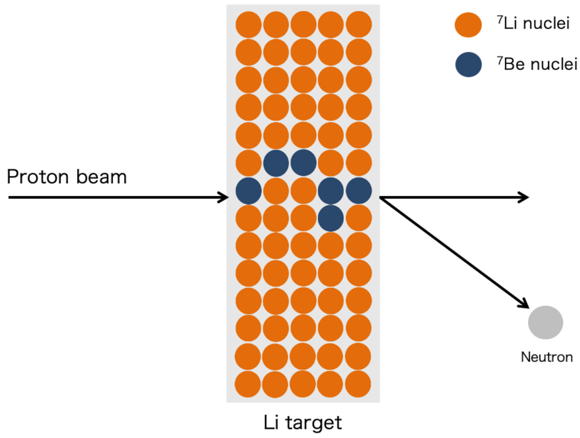

Fig. 2.1: A schematic picture of the ^{7}Be target production. ^{7}Li nuclei were activated to ^{7}Be nuclei via the ^{7}Li(p, n)^{7}Be reaction.

Fig. 2.2 shows the cross sections of the $^7\mathrm{Li}(p, n)^7\mathrm{Be}$ reaction [32]. The shaded region signifies the laboratory energy of the incident proton beam on the ^{7}Li target for producing ^{7}Be, calculated based on the energy loss in the 1.60 $\mathrm{mg/cm^2}$ (= 30.0 μm) host Li target. The ^{7}B target depth distribution was defined to follow the incident proton energy distribution of the ^{7}Li(p, n)^{7}Be cross sections.

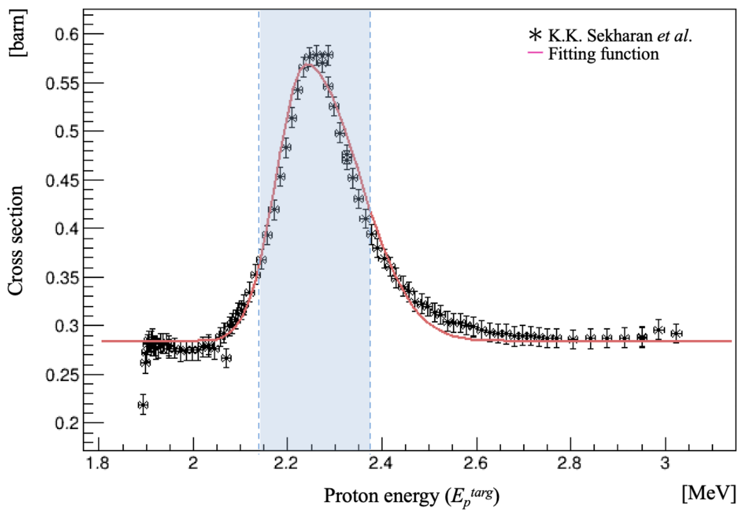

Fig. 2.2: The cross-section data of the ^{7}Li(p, n)^{7}Be reaction [32]. The shaded region shows the incident proton energy covered in the present work for the ^{7}Be target production.

Refer to 3.2 for the detailed setup and 4 for the number of produced ^{7}Be targets.

2.2 Thick Target Method

The thick target method involves conducting experiments with a thick target and a single beam of energy. The thick target method offers two distinct advantages: firstly, it allows for the measurement of multiple reactions using a single incident beam energy, and secondly, it enables the measurement of reactions with very low incident energy, nearly stopping within the target. In the analysis, a thick target was considered to be the multiplication of stacked thin targets. Fig. 2.3 shows a schematic illustration of the thick target method. In the analysis, segmented simulations were conducted, taking into account the reactions occurring in each sectored target. The simulated spectra shown at the bottom of Fig. 2.3 were calculated from each sectored target slice.

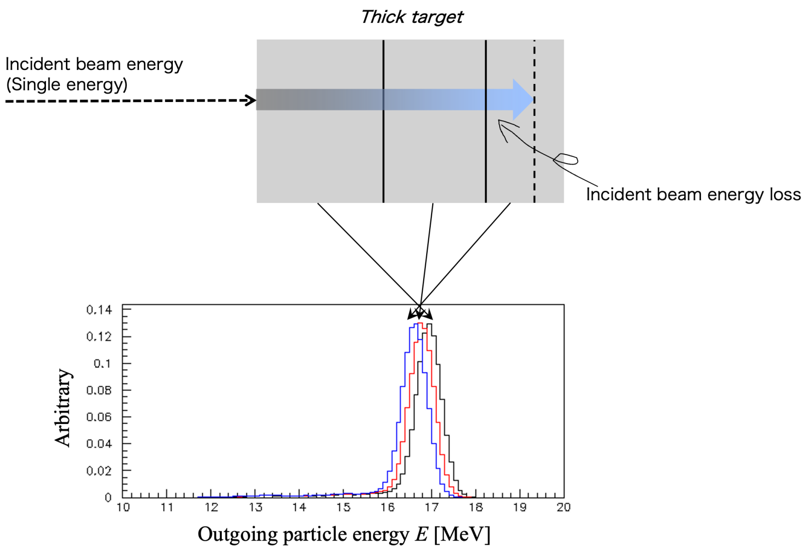

Fig. 2.3: The top image illustrates a schematic view of a single energy incident beam losing its energy in the target. The lower image depicts the results of the simulation. Simulations were conducted to predict each sectorized target's reacted outgoing particle energy spectra.

The simulations and fittings enabled the extraction of cross sections from the reactions occurring in different target sectors.

Chapter 3

Experimental Setup and Measurements

3.1 Facility and Beam Line

The experiment was carried out at Kobe University [33]. The accelerator is called Tandem PELLETRON 5SDH-2. The whole view of the facility system is shown schematically in Fig. 3.1. Cesium was heated to high temperatures using an ion source called SNICS II. In a cesium vapor environment, a material containing beam ions served as the cathode, and a tantalum filament acted as the anode, creating cesium plasma by surface ionization. When cesium-positive ions collided with the cathode, atoms from the cathode surface were ejected as negative ions by the sputtering. The ejected negative ions had an energy of about 5 keV and subsequently accelerated. The facility has five beam lines. The P45 chamber was selected for our experiment.

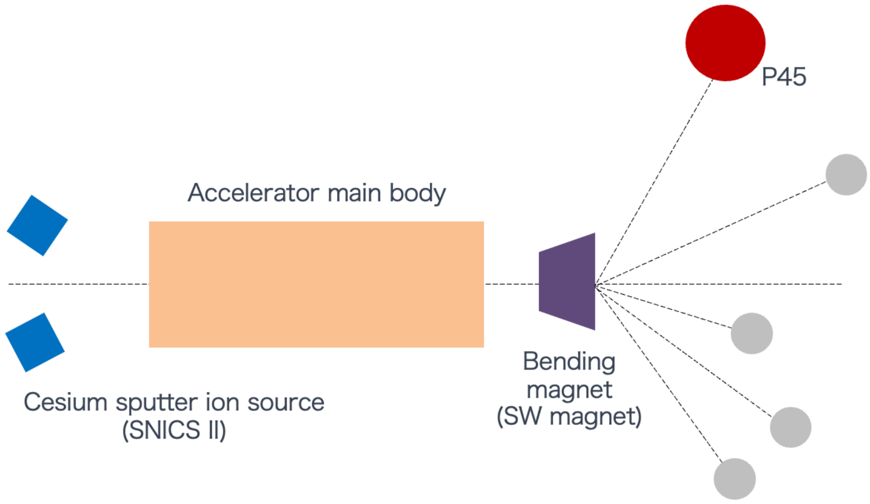

Fig. 3.1: The beam ions were generated by an ion source called SNICS II [33]. The beam ions were accelerated in tandem. The transported beam line was selected by the bending magnet (SW magnet). Our experiment was performed in the P45 chamber.

A 2.36 MeV proton beam was accelerated for the ^{7}Be target production (refer to 3.2 for the details). 1.6 and 0.6 MeV deuteron beams were produced for the $^7\mathrm{Be}(d, p)$ reaction cross-section measurements (refer to 3.4 for the details). The specification information is summarized in Table 3.1.

Table 3.1: The specification of the Tandem PELLETRON.

Maximum terminal voltage	1.7 MV
Beam energy	proton 3.4 MeV - heavy ion 10 MeV
Beam current	0.1 - 10 mA, depending on ion species
Number of the beam lines	5

3.2 $^7\mathrm{Be}$ Target Production

The first step was producing $^7\mathrm{Be}$ targets. The radioactive $^7\mathrm{Be}$ target were produced for the $^7\mathrm{Be}(d, p)^8\mathrm{Be}$ reaction measurement in normal kinematics.

3.2.1 $^7\mathrm{Be}$ Target Holding System

The target holding system was designed, and it kept the target and collimator relatively in the same positions. Fig. 3.2 shows the target holder.

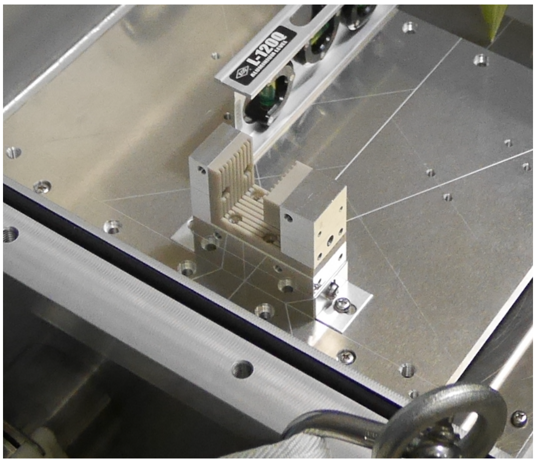

Fig. 3.2: A picture of the target holder. The inner gaps were for mounting the collimator, target, and suppressors.

The inner-bottom part of the target holder was finely grooved. The gap width was 1.1 ± 0.1 mm. It had nine gaps for holding the collimator, target, and suppressors for applying the voltage (refer to 3.4.3 for details about suppressors). The material of the gap part was ceramic, an insulation material, to prevent it from connecting electrically with the collimator and target. The current was read out separately from the collimator and target. Additionally, the voltage was applied independently to the suppressor.

3.2.2 $^7\mathrm{Be}$ Target Production Experiment

A schematic picture of the setup for the target production is shown in Fig. 3.3. A natural lithium target ($^7\mathrm{Li}$ abundance = 92.5%) was put in a target frame and placed at the target position as a host target to produce $^7\mathrm{Be}$ nuclei via the $^7\mathrm{Li}(p, n)^7\mathrm{Be}$ reaction. The thickness of the host lithium target was 1.60 $\mathrm{mg/cm^2}$ (= 30.0 μm). A collimator, made of copper with a thickness of 1.0 mm and a diameter of 2.0 mm, was placed in front of the host lithium target to define the position and area of the $^7\mathrm{Be}$ target production.

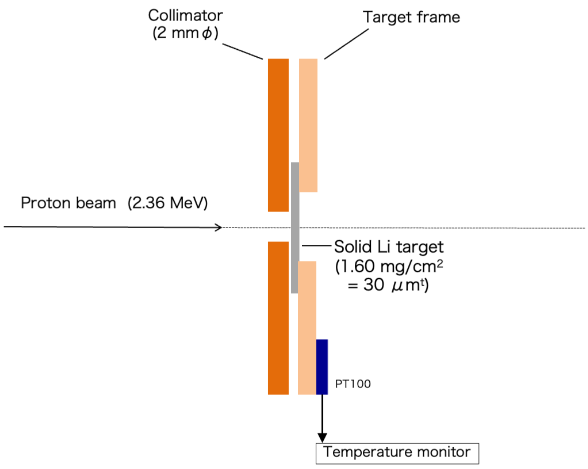

Fig. 3.3: A schematic picture of the ^{7}Be target production experiment. A copper collimator with a diameter of 2 mm was placed in front of the host Li target to define the position and area of the $^7\mathrm{Be}$ target. A platinum resistance temperature detector (PT100) was stuck on the target frame to monitor the target temperature.

The proton beam was accelerated to 2.36 MeV, and the average intensity was 400 nA. The average beam intensity was maintained for over two days to produce the $^7\mathrm{Be}$ target. A platinum resistance temperature detector (PT100) was stuck on the target frame to monitor the target temperature. The incident proton beam intensity was controlled to ensure the target temperature did not exceed 100°C.

3.3 Produced $^7\mathrm{Be}$ Target Measurement

After the ^{7}Be target production, the $^7\mathrm{Be}$ target particle number was measured. The produced $^7\mathrm{Be}$ target was kept in a small vacuum chamber since the host Li is easily oxidized and hydroxylated.

$^7\mathrm{Be}$ emits 477 keV gamma rays. The known branching ratio of the 477 keV gamma rays ($\gamma_{477} = 10.5\%$ [34]) allows for determining the number of $^7\mathrm{Be}$ nuclei by measuring the corresponding gamma-ray count. A 2-inch LaBr3 scintillation detector was used to detect the gamma rays. Fig. 3.4 shows the γ-ray measurement by a $\mathrm{LaBr_3}$ detector. The lithium-hosted $^7\mathrm{Be}$ target was treated under vacuum conditions due to lithium's characteristics of oxidation and hydroxylation. The $\mathrm{LaBr_3}$ detector was placed on the vacuum chamber, with a distance of 11 cm from the $^7\mathrm{Be}$ target to the $\mathrm{LaBr_3}$ detector surface. The chamber had a glass lid with a thickness of 1 cm.

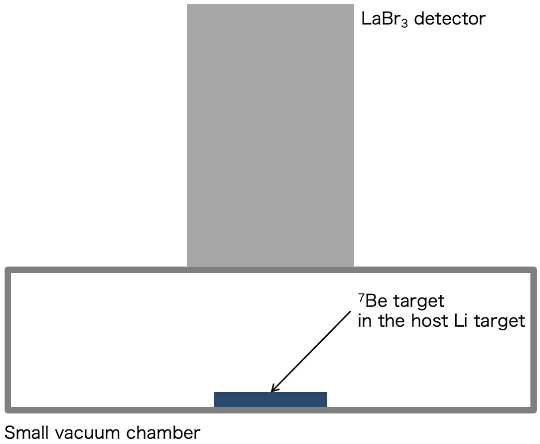

Fig. 3.4: The produced $^7\mathrm{Be}$ target was kept in a small vacuum chamber since the host Li is easily oxidized and hydroxylated. The $\mathrm{LaBr_3}$ detector was placed on the small vacuum chamber to measure the 477-keV γ-rays from $^7\mathrm{Be}$ particles.

The efficiency of the $\mathrm{LaBr_3}$ detector was calibrated using ^{137}Cs and ^{60}Co source measurements. Those checking sources and the $\mathrm{LaBr_3}$ detector were placed at the same position (within 1 mm accuracy) where the $^7\mathrm{Be}$ target measurement was performed to secure the geometrical efficiency.

The detailed evaluation is explained in 4.2.

3.4 $^7\mathrm{Be}(d,p)^8\mathrm{Be}$ Reaction Measurement

3.4.1 Silicon Detector Setup

The outgoing proton's energy and yields were measured by silicon detectors [1].

[1] A silicon detector is a type of semiconductor detector. When a charged particle with energy enters a silicon detector, the charged particle interacts with the silicon atoms, causing the electrons in the silicon atoms to gain energy and become excited, creating electron-hole pairs. The generated electrons and holes are separated by the electric field created by the voltage applied to the silicon detector. Electrons and holes move through the silicon crystal and reach the electrodes. Arriving electrons and holes cause a current flow and generate an electrical signal for the detector.

A schematic picture of the detector setup is shown in Fig. 3.5.

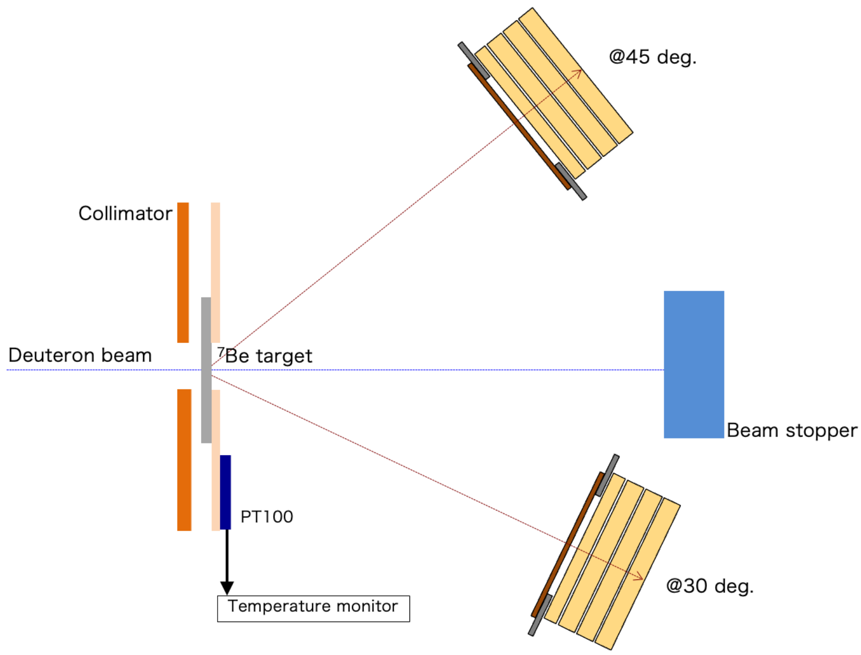

Fig. 3.5: Silicon detectors were placed at scattering angles (θ_{lab}) of 45° and 30°.

Four-layered silicon detectors were placed at scattering angles (θ_{lab}) of 45° and 30°. The angular coverage of the detectors was 23.7°–36.3° and 37.6°–52.3°. The thicknesses of the silicon detectors were 300 μm for the first layers and 500 μm for the subsequent layers. In total, eight silicon detectors were used for the measurement. The distance from the $^{7}\mathrm{Be}$ target center to the surface of the first layer silicon detector was 54 mm. In order to determine proton event numbers based on the dimensions of the fourth-layer detectors and their associated solid angles, collimators with a diameter of 12.0 mm were placed in front of the first-layer silicon detectors. 30 μm copper foils were placed in front of each detector collimator to avoid backgrounds induced by low-energy charged-particles, mainly protons, ($e.g.$, protons from $^{6}\mathrm{Li}(d,p)$, $^{16}\mathrm{O}(d,p)$ etc.) which can damage the detectors. The reaction Q-values for $^{7}\mathrm{Be}(d,p)$, $^{6}\mathrm{Li}(d,p)$, and $^{16}\mathrm{O}(d,p)$ reactions are 16.7, 5.03, and 1.92 MeV, respectively [35]. $^{7}\mathrm{Be}(d,p)^{8}\mathrm{Be}$ reaction have relatively high Q-value. An advantage of this measurement was distinguishing the proton events by its energy from other proton events caused by $^{6}\mathrm{Li}(d,p)$ and $^{16}\mathrm{O}(d,p)$ reactions. The detector names, detector layers, and detector angles were summarized in Table 3.2.

Table 3.2: The summary of the detector names, detector layers, and detector angles.

Detector names	Detector layers	Detector angles [θ_{lab}]
S1	First	45°
S2	Second	45°
S3	Third	45°
S4	Fourth	45°
S5	First	30°
S6	Second	30°
S7	Third	30°
S8	Fourth	30°

After the ^{7}Be target number measurement, the ^{7}Be target was placed back in the original target position. The beam was switched to deuteron after the proton irradiation for the target activation measurement. The incident deuteron beam energies (E_d) were accelerated to 0.6 and 1.6 MeV. A collimator made of copper with a thickness of 1.0 mm and a diameter of 3.0 mm was positioned in front of the lithium (^{7}Be) target to determine the deuteron beam position and area.

3.4.2 Energy Calibration

An ^{241}Am source was used for the energy calibration of the silicon detectors. The ^{241}Am source emitted alpha particles with an energy of 5.48 MeV. The ^{241}Am source was placed at the target position, and silicon detectors were placed at the detector position. The analysis of the energy calibration for the silicon detectors is explained in 5.1.

3.4.3 Beam Current Read Out and Electron Suppressors

The beam current was directly measured from the target and stopper using a current integrator with the model number ORTEC 439 (refer to Fig. A.1 for the detailed circuitry and connections). Electron suppressors were installed for the collimator and the target to correctly read out the beam current. When incident beam particles with energy collided with a material, electrons in the material were knocked out. As electrons were knocked out, the current read value was larger than the actual value. Fig. 3.6 schematically depicts the interaction when a beam particle collided with the material.

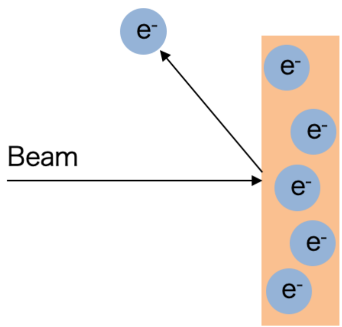

Fig. 3.6: Free electrons were knocked out when the beam particles, possessing kinetic energy, collided with the material.

A suppressor was implemented to prevent the measurement of a current higher than its actual value. The suppressor, constructed from a 1.0 mm thick copper plate, was subjected to a negative voltage (= -200 V). The collimator and target, the materials responsible for current measurement, were maintained at a voltage of $0\ \mathrm{V}$, resulting in a relatively higher potential when viewed from the suppressors. Consequently, an electric field was established from the collimator and target toward the suppressor. The electric field functioned by pushing the knockout electrons back to the collimator and target. The schematic representation of the suppressor's function is depicted in Fig. 3.7. Red arrows represent the effective electric field.

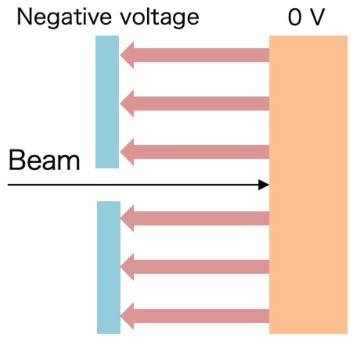

Fig. 3.7: Red arrows represent the electric field produced by the negative voltage applied to the suppressor. Consequently, escaping electrons were pushed back towards the target by this electric field.

Suppressors were installed for both the collimator and the target. When beam particles collided on either the collimator or the target, the electric field functioned to pull back the escaping electrons.

The beam passed through the target and reached the stopper at the ΔE_d = 1.6 MeV measurement, while the beam stopped inside the target at the ΔE_d = 0.6 MeV measurement. Consequently, the optimal voltage for both suppressors, one for the collimator and one for the target was separately adjusted to accommodate the different ΔE_d measurements.

The incident beam currents were 400 nA on average. The beam intensity was measured directly by current integrators from the target plate and the beam stopper placed downstream to determine the number of incident beam particles.

The incident deuteron beam intensity was maintained by the PT100 to ensure the target temperature did not exceed 100°C.

3.4.4 Data Acquisition

Data from two sets of four-layered silicon detectors were independently acquired. Eight silicon detectors, S1 to S8, were employed in total. Each silicon detector generated charge outputs directed to the MSI-8 module. The MSI-8 module served both as a timing filter and a shaping pre-amplifier. Subsequently, a discriminator, specifically the CF8000 model, differentiated signals based on the timing output of the MSI-8 module.

The discriminated signals were then processed by a logic unit module with the model number P756, generating a coincidence signal. The P756 module produced a trigger signal when signals were emitted by two out of the four silicon detectors, a mode referred to as the double coincidence mode. The charge outputs, containing energy information about the signals, were acquired by an ADC module with the model number HOSHIN ADC C008. CC/NET system were used for the data acquisition. The electronics circuit shown in Fig. 3.8 (refer to A.1 for more detailed electronics circuit).

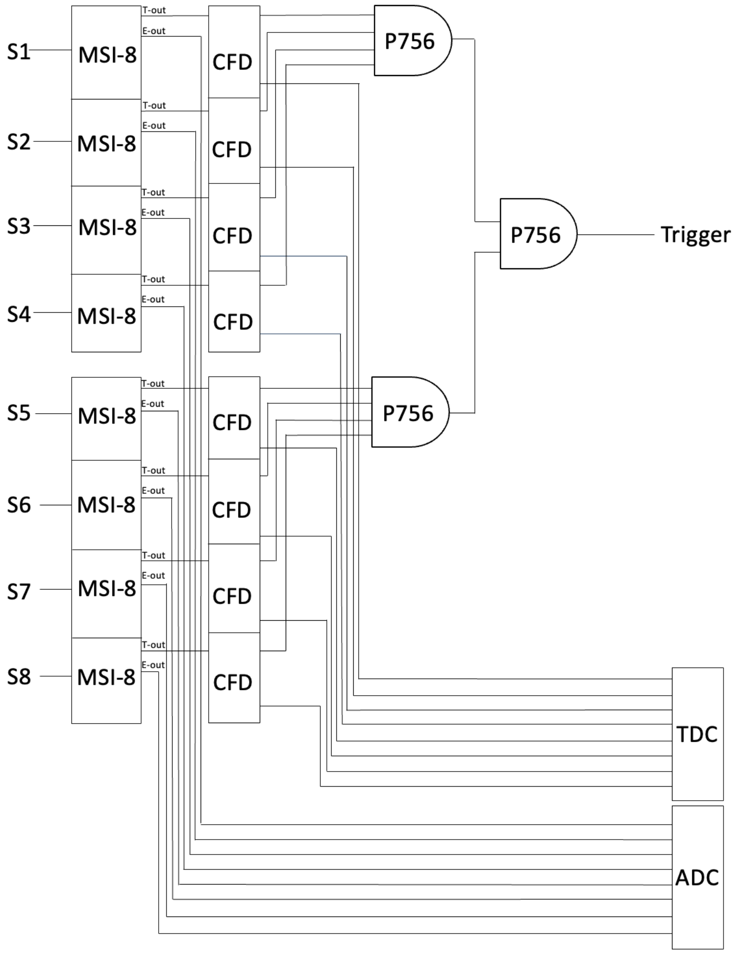

Fig. 3.8: Abbreviated electrical circuit diagram.

Chapter 4

Data Analysis of the Gamma-ray Measurement of ^{7}Be Target

4.1 $\mathrm{LaBr_3}$ Detector Efficiency

A $\mathrm{LaBr_3}$ scintillator detector was employed to measure gamma rays emitted from a $^{7}\mathrm{Be}$ target. $^{137}\mathrm{Cs}$ and $^{60}\mathrm{Co}$ sources were used to determine the efficiency of the $\mathrm{LaBr_3}$ detector. These sources' activities (i.e., the emitted gamma rays per second) were calibrated and known. The efficiency of the detector was obtained by comparing the detected number of gamma rays from sources by the $\mathrm{LaBr_3}$ detector with the calibrated source activities. The details of the checking sources for $^{137}\mathrm{Cs}$ and $^{60}\mathrm{Co}$ are summarized in Table 4.1.

Table 4.1: The details of the checking sources.

Nuclides	Half-life ($t_{1/2}$) [y]	Calibrated date [y/m/d]	Original activity [Bq]	Accuracy [%]
$^{137}\mathrm{Cs}$	30.07	1984/6/1	397380	3.7
$^{60}\mathrm{Co}$	5.27	1984/6/1	407370	1.9

In order to evaluate both the intrinsic detector efficiency and the geometrical efficiency simultaneously, the $\mathrm{LaBr_3}$ detector was positioned in the identical geometrical configuration (refer to Fig. 3.4) as used in the gamma-ray measurement from the $^{7}\mathrm{Be}$

target. The identical electronics and modules were employed for both gamma-ray measurements of sources and the $^{7}\mathrm{Be}$ target, ensuring consistency in the experimental setup.

Given an original source activity of N_0, a decay constant of λ, and an elapsed time denoted as T from the source calibration date to the day of the $^{7}\mathrm{Be}$ target measurement, the activity N_{current} on the $^{7}\mathrm{Be}$ target measurement date is determined using the following Eq. (4.1).

$$N_{\text{current}} = N_0 \cdot \exp(-\lambda T) \tag{4.1}$$

The decay constant λ was described as Eq. (4.2) with the half-life of the checking source $t_{1/2}$.

$$\lambda = \frac{\ln(2)}{t_{1/2}} \tag{4.2}$$

The net count of the detected gamma-ray photopeak from the source is denoted as N_{peak}. The efficiency of the $\mathrm{LaBr_3}$ detector, denoted as $\varepsilon_{\mathrm{LaBr_3}}$, is described by Eq. (4.3), utilizing the photopeak counts N_{peak} obtained from the sources $^{137}\mathrm{Cs}$ or $^{60}\mathrm{Co}$.

$$\varepsilon_{\mathrm{LaBr_3}} = \frac{N_{\text{peak}}}{N_{\text{current}}} \tag{4.3}$$

Efficiencies at three energies from $^{137}\mathrm{Cs}$ and $^{60}\mathrm{Co}$ were calculated. Fig. 4.1 shows the efficiency as the function of source photopeak energy.

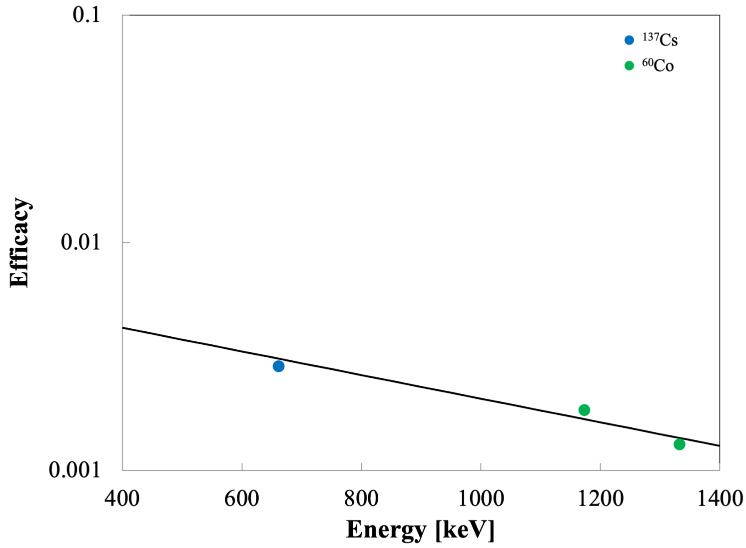

Fig. 4.1: The correlation between the efficiencies and energies.

The extrapolation of the fitted efficiency function of sources determined the efficiency at 477 keV. The efficiency was modeled as an exponential function of energies.

The fitting function $g(x)$ represented the logarithm of efficiencies. Eq. (4.4) demonstrates the fitting function with parameters n and m. Here, x was energy.

$$g(x) = m + n(x - 477) \tag{4.4}$$

The fitting result is shown by the solid line in Fig. 4.1.

As the result, the parameter m was -5.558. $\varepsilon_{\mathrm{LaBr_3}}$ was determined by following Eq. (4.5).

$$\varepsilon_{\mathrm{LaBr_3}} = \exp(m) \tag{4.5}$$

Substituting $m = -5.558$ into Eq. 4.5, efficiency $\varepsilon_{\mathrm{LaBr_3}}$ was 0.00389.

Additionally, the statistical errors in calculating efficiency were influenced by the fitting. The systematic error was estimated using the checking source accuracies (refer to Table 4.1). The activities of the $^{137}\mathrm{Cs}$ and $^{60}\mathrm{Co}$ sources were associated with uncertainties. The efficiency at 477 keV was determined by varying the activity of each source within its respective accuracy range. Systematic errors were derived individually from the analyses of both $^{137}\mathrm{Cs}$ and $^{60}\mathrm{Co}$. The overall systematic error, resulting from the analysis of source accuracies, was determined through error propagation, considering both errors originated from ^{137}Cs and ^{60}Cosource accuracies. The summary of statistical and systematic errors resulting from the verification of ^{137}Cs and ^{60}Co sources is presented in Table 4.2.

Table 4.2: The statistical and systematic errors of the $LaBr_3$ detector efficiency.

Statistical error [%]	Systematic error [%]
0.69	4.3

4.2 ^{7}Be **Target Number**

The 477 keV gamma ray was emitted during the electron capture process of ^{7}Be. Fig. 4.2 displays the gamma-ray spectra measured by the $LaBr_3$ detector. The blue solid line represents the spectrum obtained with the ^{7}Be target. The red solid line corresponds to the background spectrum acquired without the ^{7}Be target. The green solid line represents the background-subtracted spectrum, obtained by subtracting the spectrum acquired without the ^{7}Be target from the spectrum acquired with the ^{7}Be target.

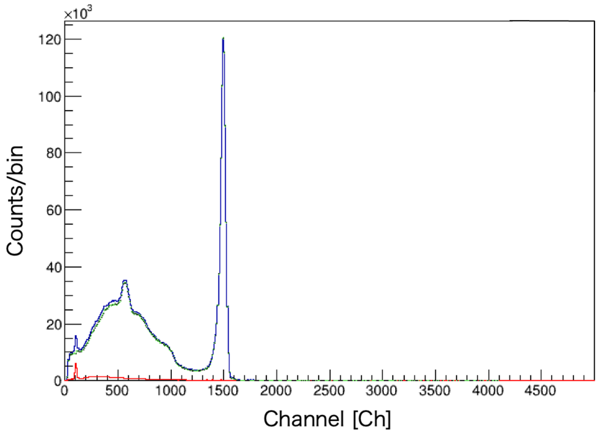

Fig. 4.2: The blue solid line represents the spectrum with the ^{7}Be target, and the red solid line represents the background spectrum without the ^{7}Be target. The green solid line represents the background subtracted.

The produced ^{7}Be number ($N_{^7\mathrm{Be}}$) was calculated by the following Eq. (4.6).

$$N_{^7\mathrm{Be}} = \frac{R \times T}{\varepsilon_{\mathrm{LaBr_3}} \times I_r \times \ln(2)} \tag{4.6}$$

R represents the ratio of the net counts in the gamma-ray photopeak to the actual measurement time. Here, the "net counts in the gamma-ray photopeak" refers to the actual counts measured in the photopeak region. T is the measurement time in seconds, $\varepsilon_{\mathrm{LaBr_3}}$ denotes the $\mathrm{LaBr_3}$ detector efficiency obtain in the analysis written in 4.1. I_r represents the probability of $^7\mathrm{Be}$ undergoing electron capture decay and subsequently emitting a 477 keV gamma ray via the excited state of $^7\mathrm{Li}$. I_r is 10.5% [34].

2.80×10^{13} $^7\mathrm{Be}$ nuclei were produced as the target after two days of proton irradiation.

Chapter 5

Data Analysis of $^{7}\mathrm{Be}(d,p)^{8}\mathrm{Be}$ Reaction Cross Section

5.1 Energy Calibration for Silicon Detectors

The silicon detectors were calibrated using a $^{241}\mathrm{Am}$ source. Energy spectra are shown in Fig. 5.1. The range from 0 to 50 channels represents the pedestal, indicating the offset level of the ADC in the absence of signals. The range from 2000 to 2200 channels corresponds to the energy deposited by 5.486 MeV alpha particles emitted by the $^{241}\mathrm{Am}$ source.

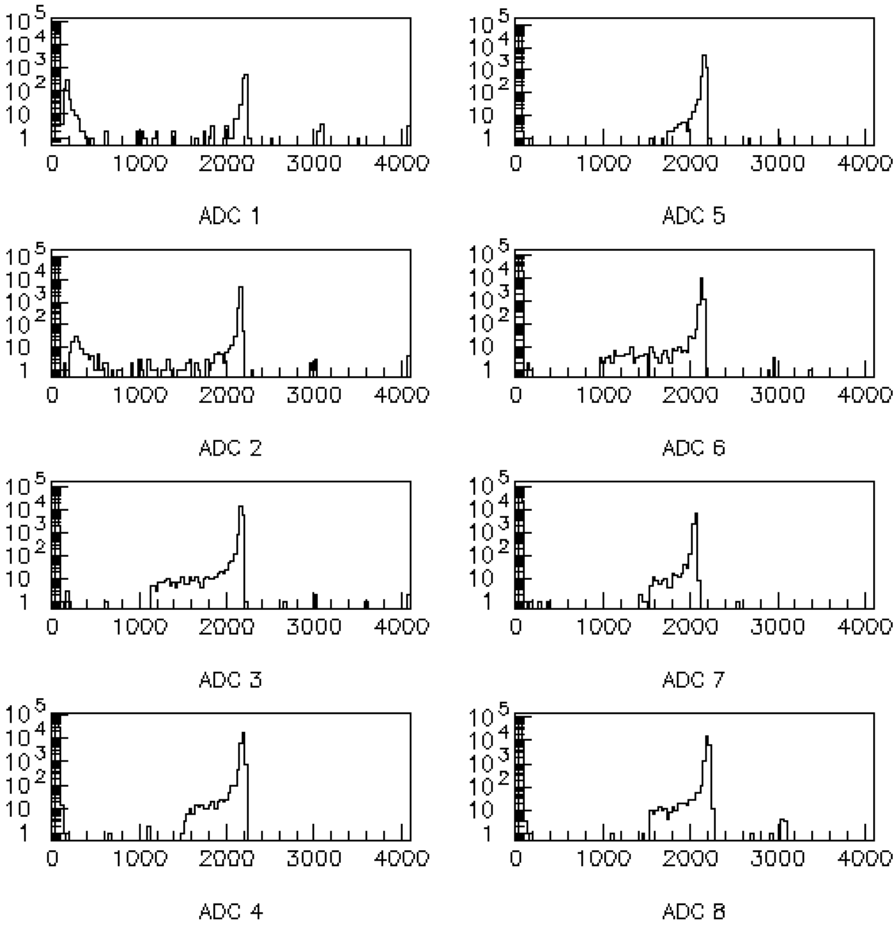

Fig. 5.1: Energy spectra taken by the ADC. ADC1 - ADC4 correspond to the first to fourth layer at 45-degree detectors. ADC5 - ADC8 correspond to the first to fourth layer at 30-degree detectors.

The ADC response was assumed to be linear between the pedestal and the 5.486 MeV peak. The calibrated energy ($E_{\text{cal.}}$) is described by the ADC channel (adc) using the following Eq. (5.1).

$$E_{\text{cal.}} = \frac{5.486}{ch_\alpha - ch_p} \times (adc - ch_p) \tag{5.1}$$

The pedestal channel is denoted as ch_p, and the 5.486 MeV alpha-ray peak channel is denoted as ch_α.

When expanding Eq. (5.1), slope a_1 and intercept a_0 are expressed as follows.

$$a_1 = \frac{5.486}{ch_\alpha - ch_p} \tag{5.2}$$

$$a_0 = \frac{5.486}{ch_\alpha - ch_p} \cdot ch_p \tag{5.3}$$

Calibration parameters a_1 and a_0 are summarized in Table 5.1. S1 - S4 correspond to the first to fourth layer at 45-degree detectors. S5 - S8 correspond to the first to fourth layer at 30-degree detectors. The errors in parameter fitting were negligibly minor compared to the desired energy resolution.

Table 5.1: The energy calibration parameters a_1 and a_0 for silicon detectors. S1 - S4 correspond to the first to fourth layer at 45-degree detectors. S5 - S8 correspond to the first to fourth layer at 30-degree detectors.

Detector	a_1	a_0
S1	0.00256	-0.167
S2	0.00261	-0.143
S3	0.00259	-0.132
S4	0.00258	-0.151
S5	0.00258	-0.0987
S6	0.00263	-0.119
S7	0.00274	-0.141
S8	0.00255	-0.135

5.2 Event Selection and Particle Identification

To determine the reaction cross section, the number of outgoing proton events from the $^7\mathrm{Be}(d,p)^8\mathrm{Be}$ reaction were counted. Timing gates were applied to select events that either arrived at the fourth layer or stopped at the third layer of silicon detectors. Detailed analyses of each experimental setup are explained separately below.

5.2.1 $E_d = 1.6\,\mathrm{MeV}, @45°$

Proton Events Arrived to the Fourth Layer

Fig. 5.2 depicts the energy deposit in the third layer (ΔE_3) vs. the second layer (ΔE_2) at the left panel and the fourth layer (ΔE_4) vs. the third layer (ΔE_3) at the right panel without any event selection. As Fig. 5.2 shows, the two-dimensional plots, which did not have timing gates applied, included a large number of accidental events. Since the data was recorded using the double coincidence mode (refer to 3.4.4), events were recorded when signals were simultaneously detected in two out of four detectors.

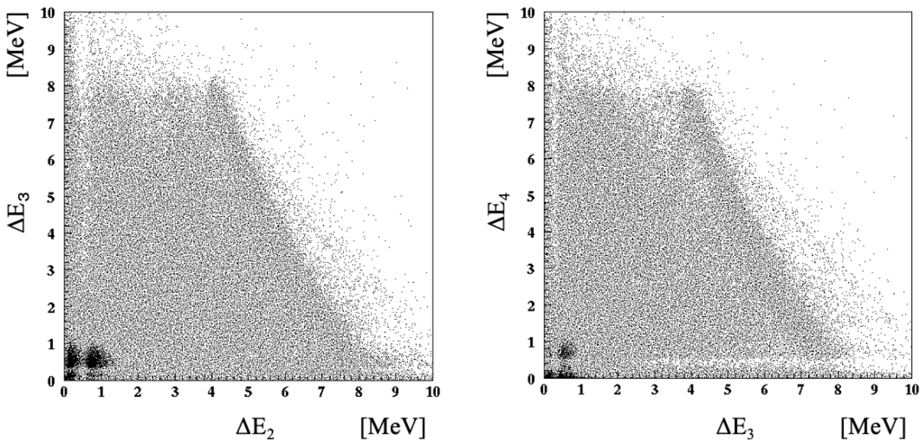

Fig. 5.2: Two-dimensional plots of energy deposits in the silicon detectors without timing gates. The left panel displays the energy deposit in the third-layer silicon detector plotted against that in the second-layer silicon detector. The right panel displays the energy deposit in the fourth-layer silicon detector plotted against that in the third-layer silicon detector.

The $^7\mathrm{Be}(d,p)^8\mathrm{Be}$ reaction has a relatively high Q-value of 16.7 MeV. This feature was beneficial as it resulted in significantly higher proton energies being emitted. Other reactions, such as $^7\mathrm{Li}(d,p)$ and $^{16}\mathrm{O}(d,p)$ reactions, which produced protons as contamination in this study, had lower Q-values of 5.03 and 1.92 MeV, respectively. The $^6\mathrm{Li}$ nuclei were in the Li host target, and the $^{16}\mathrm{O}$ nuclei were on the Li host target's surface due to the Li oxidation. These nuclei produced protons through the reactions with the deuteron beam. Hence, we could distinguish proton events based on the proton energy arising from the $^7\mathrm{Be}(d,p)^8\mathrm{Be}$ reaction. Only the proton events from the $^7\mathrm{Be}(d,p)^8\mathrm{Be}$ reaction could reach the fourth or third layers.

The timing differences were obtained by subtracting the first-layer silicon detector timing signal from each detector's TDC timing signals. The timing differences between the first and other layers were nearly zero when an event reached the fourth layer. Fig. 5.3 shows the timing differences between the first layer's timing signal and others. The top panel is the timing difference between the second and the first layer ($\mathrm{TDC2}-\mathrm{TDC1}$). The middle panel is the timing difference between the third and the first layer ($\mathrm{TDC3}-\mathrm{TDC1}$). The bottom panel is the timing difference between the fourth and the first layer ($\mathrm{TDC4}-\mathrm{TDC1}$). The events that arrived at the fourth layers were represented by the sharp peak at $0\ \mathrm{ns}$, and the timing difference was dispersed at $0\ \mathrm{ns}$.

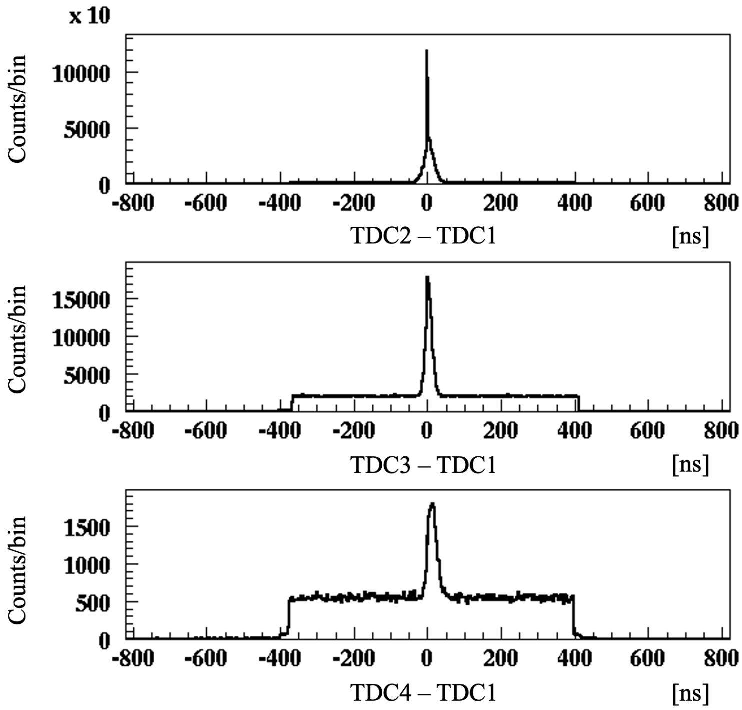

Fig. 5.3: The timing difference between the first layer's timing signal and other layers for 45° detectors.

The time-difference peaks were used to gate the energy in two-dimensional histograms, covering time ranges of -100 ns to 100 ns, to select proton events from the

$^7\mathrm{Be}(d,p)^8\mathrm{Be}$ reaction that arrived at the fourth layer.

Fig. 5.4 shows ΔE_3 - ΔE_2 and ΔE_4 - ΔE_3 two-dimensional histograms after the timing gates were applied. The proton loci corresponding to the $^7\mathrm{Be}(d,p)^8\mathrm{Be}$ reaction were highlighted.

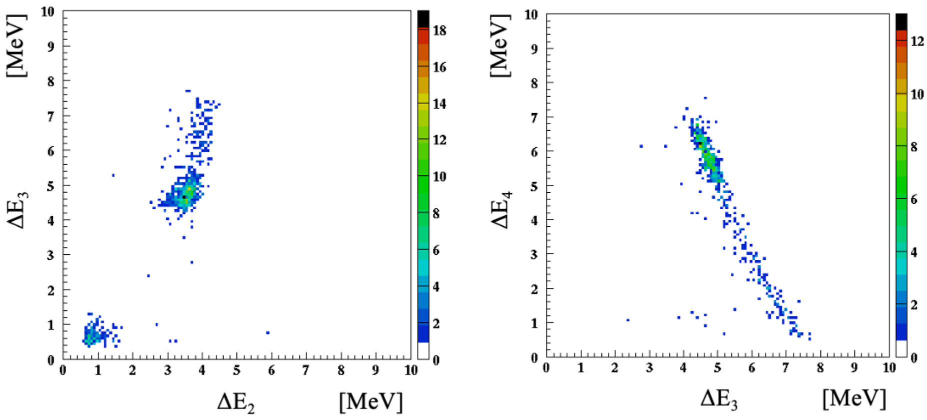

Fig. 5.4: Selected ΔE_3 - ΔE_2 and ΔE_4 - ΔE_3 plots at 45° from the silicon detectors. (Left) The third layer vs. The second layer; (Right) The fourth layer vs. The third layer.

Proton Events Stopped at the Third Layer

The proton events that reached and stopped at the third layer were also subject to analysis. Those proton events were stopped inside the third layer and did not proceed to the fourth layer. For this event selection, both $\mathrm{TDC2} - \mathrm{TDC1}$ and $\mathrm{TDC3} - \mathrm{TDC1}$ were selected to be within the range of -100 ns to 100 ns, while neither $\mathrm{TDC4} - \mathrm{TDC1}$ nor the range of -100 ns to 100 ns were considered.

Fig. 5.5 depicts the two-dimensional histogram ΔE_3 - ΔE_2 after the timing gates were applied.

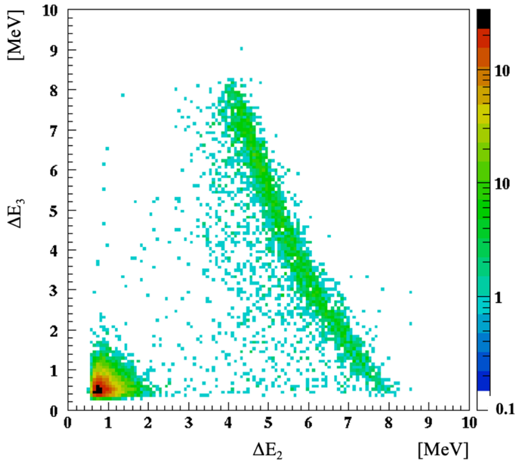

Fig. 5.5: The event selection was based on the TDC timing gate. The ΔE_3 - ΔE_2 plots at 45° from the silicon detectors.

The events detected in the first and second layers were unavailable for reconstructing the original proton energies, as those proton events originated from the other dp reaction channels. Therefore, total proton energies (E_p) were reconstructed using the energy loss function based on events detected by the third layer.

Proton Energy Spectrum by the Measurement at $E_d = 1.6$ MeV, @45°

Fig. 5.6 shows the proton energy spectrum reconstructed the energies detected by the fourth and third layer. Proton events arrived the fourth layer and stopped inside of the third layer were included.

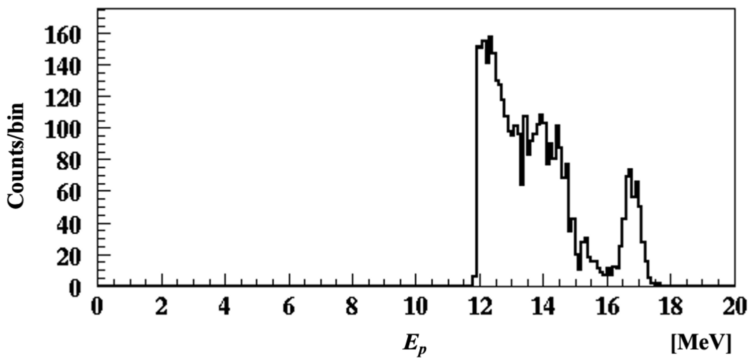

Fig. 5.6: The proton energy spectrum reconstructed by the fourth and third layers energies.

5.2.2 $E_d = 1.6\ \mathrm{MeV}, @30°$

The basic analysis followed the method outlined in (5.2.1). Without any event selection, Fig. 5.7 depicts the energy deposit in the third layer (ΔE_7) vs. the second layer (ΔE_6) in the left panel, and the fourth layer (ΔE_8) vs. the third layer (ΔE_7) in the right panel.

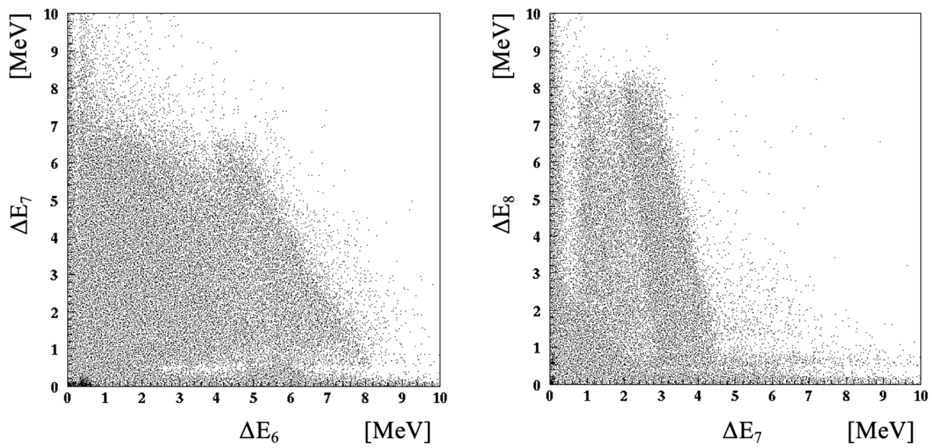

Fig. 5.7: The two-dimensional plots without timing gates.

The timing differences between the first layer's timing signal and others are displayed in Fig. 5.8. The top panel shows the timing difference between the second layer and the first layer (TDC6 − TDC5). The middle panel displays the timing difference between the third layer and the first layer (TDC7 − TDC5), while the bottom panel shows the timing difference between the fourth layer and the first layer (TDC8 − TDC5).

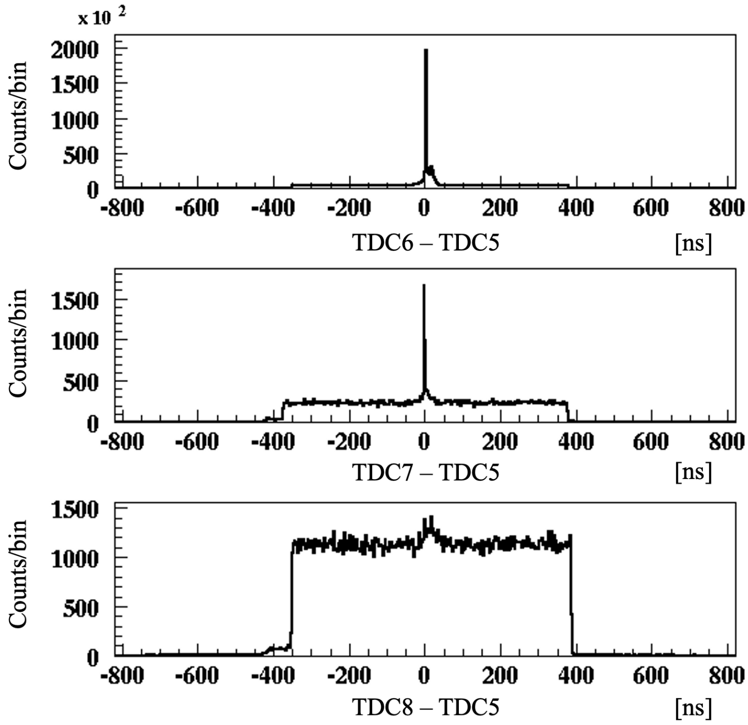

Fig. 5.8: The timing difference between the first layer's timing signal and others for 30° detectors.

The time-difference peaks were used to gate the energy in two-dimensional histograms, covering time ranges of -100 ns to 100 ns, to select proton events from the $^{7}\mathrm{Be}(d,p)^{8}\mathrm{Be}$ reaction that arrived the fourth layer.

Fig. 5.9 shows ΔE_7 - ΔE_6 and ΔE_8 - ΔE_7 two-dimensional histograms after applying the timing gates.

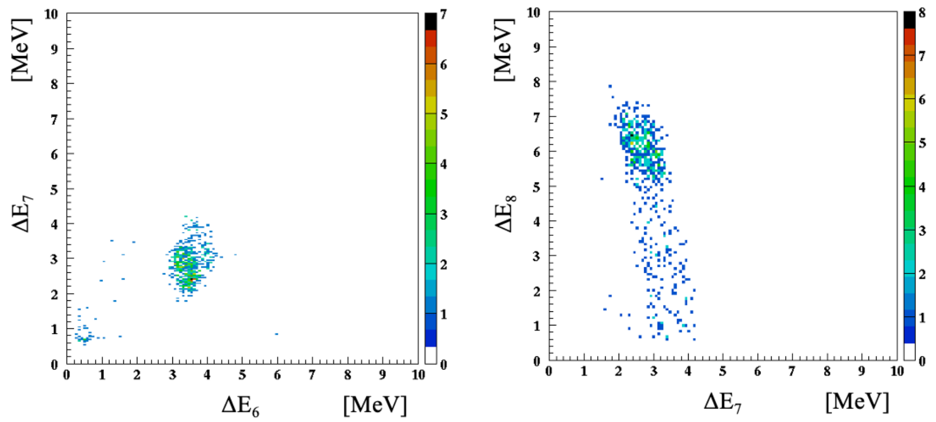

Fig. 5.9: Selected ΔE_7 - ΔE_6 and ΔE_8 - ΔE_7 plots at 30° from the silicon detectors. (Left) The third layer vs. The second layer; (Right) The fourth layer vs. The third layer. The gain shift appeared of the energy of the third layer (ΔE_7).

As demonstrated in the Fig. 5.9, a gain shift occurred at the energy of the third layer (ΔE_7). We suspected the energy shift might have occurred by neutrons from nuclear reaction processes, resulting in damage to the detector or a faulty connection in the silicon detector signal cable. However, no conclusive evidence was found.

Proton Energy Spectrum by the Measurement at $E_d = 1.6\ \mathrm{MeV}, @30°$

The total proton energy was calculated using the energy loss function. Due to the gain shift that occurred at the third-layer silicon detector, the proton energy was reconstructed, excluding the energy of the third layer and relying on the energy of the fourth layer. The proton energy spectrum is shown in Fig. 5.10.

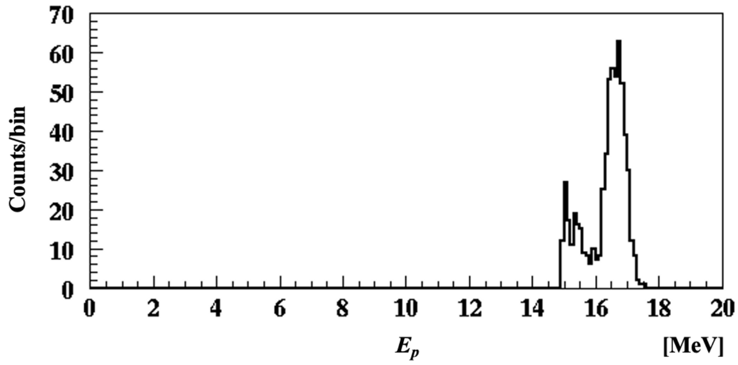

Fig. 5.10: The proton energy spectrum reconstructed by the fourth layer energy.

5.2.3 $E_d = 0.6$ MeV, @45°

Proton Events Arrived to the Fourth Layer

The data acquired at the incident deuteron energy (E_d) were 0.6 MeV, consistent with the relevant data within the Big Bang energy region. The energy band corresponding to Big Bang nucleosynthesis, $E_{\mathrm{C.M.}}$ = 0.1-0.4 MeV, corresponded to E_d = 0.6 MeV. Fig. 5.11 depicts the energy deposits without any event selection in the third layer (ΔE_3) vs. the second layer (ΔE_2) in the left panel and the fourth layer (ΔE_4) vs. the third layer (ΔE_3) in the right panel.

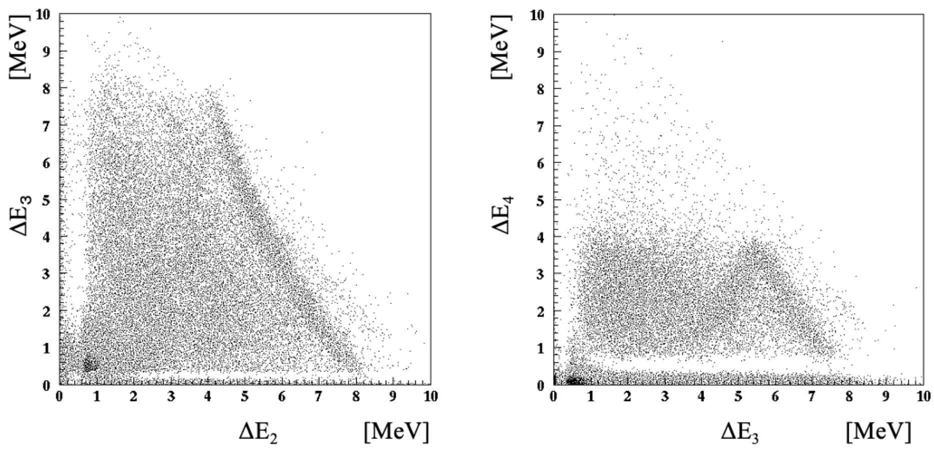

Fig. 5.11: Two-dimensional plots without timing gates.

Fig. 5.12 shows the timing differences between the first layer's timing signal and the signals from other layers. The top panel displays the timing difference between the second and the first layer ($\mathrm{TDC2} - \mathrm{TDC1}$). The middle panel shows the timing difference between the third and the first layer ($\mathrm{TDC3} - \mathrm{TDC1}$), while the bottom panel presents the timing difference between the fourth and the first layer ($\mathrm{TDC4} - \mathrm{TDC1}$).

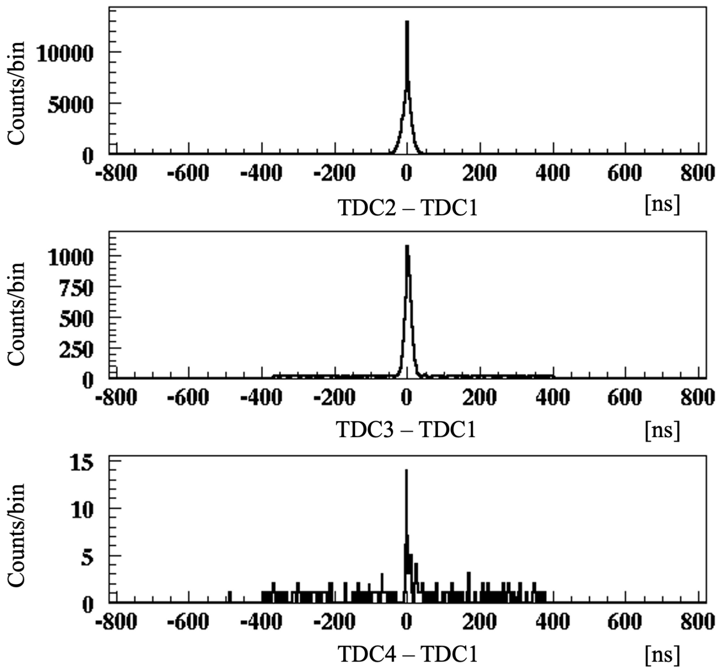

Fig. 5.12: The timing difference between the first layer's timing signal and other layers for 45° detectors.

The time-difference peaks were used to gate the energy in two-dimensional histograms, covering time ranges of -100 ns to 100 ns, to select proton events from the $^7\mathrm{Be}(d,p)^8\mathrm{Be}$ reaction that reached the fourth layer.

Fig. 5.13 displays ΔE_3 - ΔE_2 and ΔE_4 - ΔE_3 two-dimensional histograms after applying the timing gates.

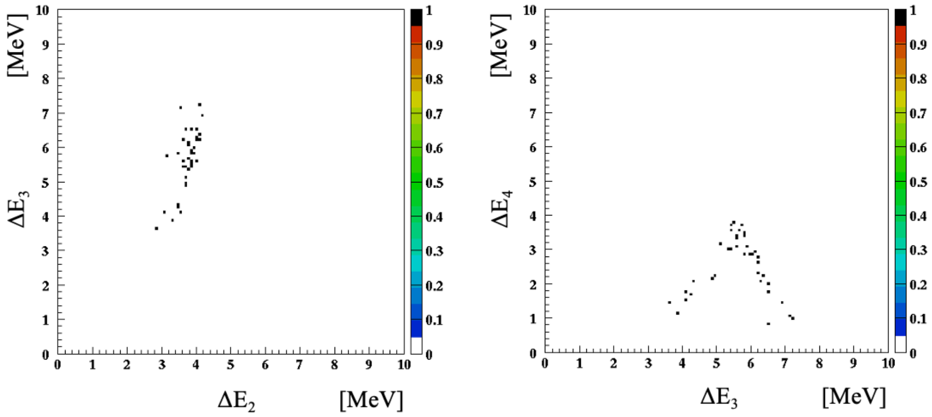

Fig. 5.13: Selected ΔE_3 - ΔE_2 and ΔE_4 - ΔE_3 plots at 45° from the silicon detectors. (Left) The third layer vs. The second layer; (Right) The fourth layer vs. The third layer.

As shown in Fig. 5.13, a gain shift occurred at the energy of the fourth layer at higher energies (>4 MeV). The measurement at E_d = 1.6 MeV, the third layer involving the third layer detector (SSD7) at 30° experienced an energy gain shift (refer to 5.2.2 and Fig. 5.9). After the measurement at E_d = 1.6 MeV, the positions of the third layer at 30° (SSD7) and the position of the fourth layer at 45° (SSD4) were swapped inadvertently when moving on to the measurement at E_d = 0.6 MeV. Thus, (SSD7) and (SSD4) were the same detectors but placed at different positions in those two measurements at E_d = 1.6 MeV and E_d = 0.6 MeV. These gain shifts were observed in the measurements of E_d = 1.6 and 0.6 MeV, and considered reasonable.

The energy of the fourth layer was not usable for reconstructing the total proton energy due to the observed gain shift. Since the third-layer detector was operating correctly, the total proton energy was calculated using the energy measured by the third layer. The proton energy was reconstructed by only using the detected energy in the third layer for two types of events: one stopped at the third layer, and the other penetrated the third layer and arrived at the fourth layer.

Fig. 5.14 shows the calculated energy deposit of the fourth layer vs. that measured in the third layer. One crucial note is that the proton energy resolution was only associated with the intrinsic energy of the third-layer detector for events that both stopped and penetrated the third layer.

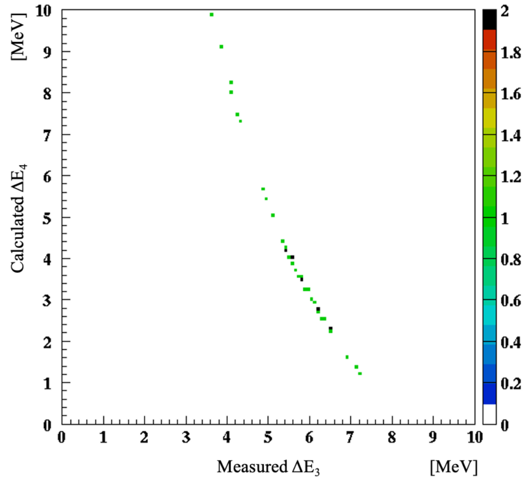

Fig. 5.14: The calculated ΔE_4 vs. measured ΔE_3.

Proton Events Stopped at the Third Layer

The proton events that arrived and stopped at the third layer were also analyzed. For this event selection, both $\mathrm{TDC2} - \mathrm{TDC1}$ and $\mathrm{TDC3} - \mathrm{TDC1}$ were selected to be within the range of -100 ns to 100 ns, while neither $\mathrm{TDC4} - \mathrm{TDC1}$ nor the range of -100 ns to 100 ns were considered.

Fig. 5.15 depicts the two-dimensional histogram ΔE_3 - ΔE_2 after applying the timing gates.

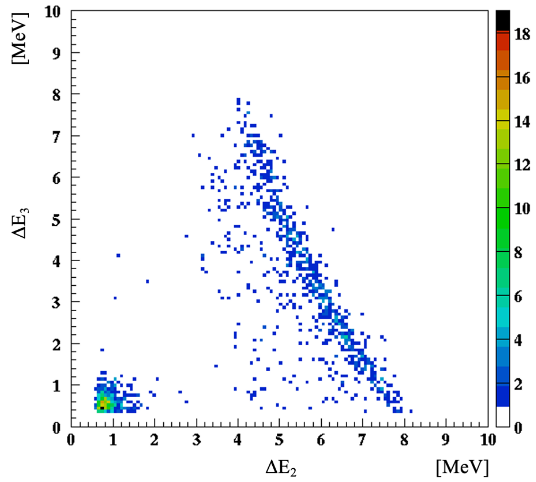

Fig. 5.15: Selected ΔE_3 - ΔE_2 plots at 45° from the silicon detectors.

Proton Energy Spectrum by the Measurement at $E_d = 0.6\,\mathrm{MeV}, @45°$

The total proton energy was reconstructed by the energy detected in the third layer using the energy loss function. Fig. 5.16 shows the proton energy spectrum.

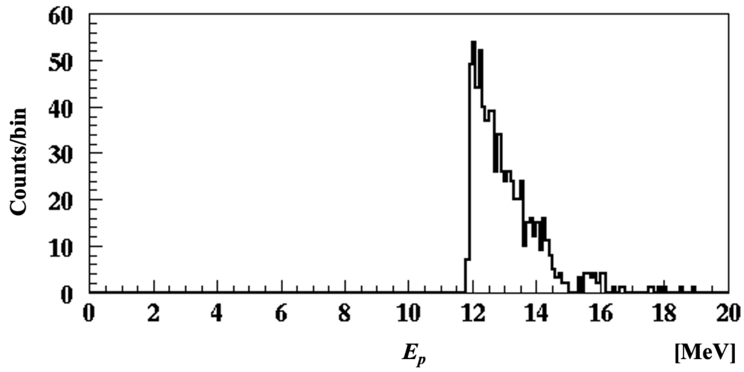

Fig. 5.16: The proton energy spectrum reconstructed by the energy detected in the third layer.

The proton events from the $^7\mathrm{Be}(d,p)^8\mathrm{Be}^{g.s.}$ reaction correspond to a proton energy of about 16.0 MeV. However, no prominent peaks from the $^7\mathrm{Be}(d,p)^8\mathrm{Be}^{1st}$ reaction, expected to be around 13.0 MeV, were observed.

5.2.4 $E_d = 0.6\,\mathrm{MeV}, @30°$

Fig. 5.17 shows the energy deposits without any event selection in the third layer (ΔE_7) vs. the second layer (ΔE_6) in the left panel and the fourth layer (ΔE_8) vs. the third layer (ΔE_7) in the right panel.

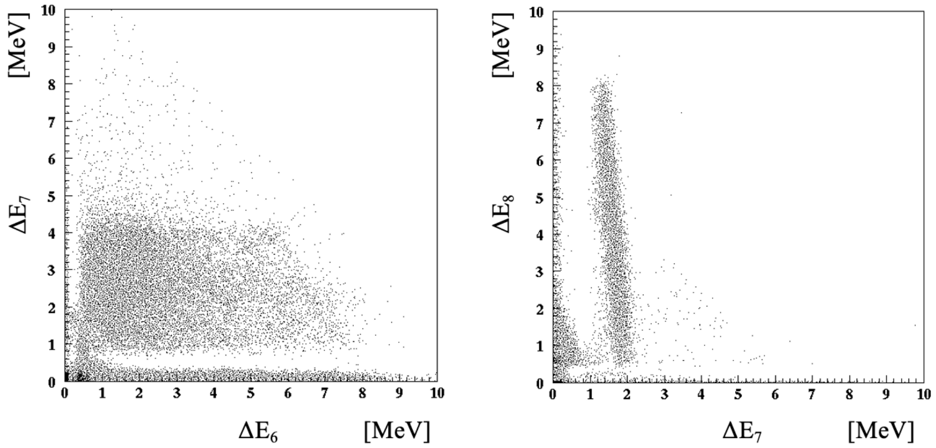

Fig. 5.17: Two-dimensional plots without timing gates.

Fig. 5.18 depicts the timing differences between the first layer's timing signal and signals from other layers. The top panel shows the timing difference between the second and the first layer ($\mathrm{TDC6} - \mathrm{TDC5}$). The middle panel displays the timing difference between the third and the first layer ($\mathrm{TDC7} - \mathrm{TDC5}$), while the bottom panel presents the timing difference between the fourth and the first layer ($\mathrm{TDC8} - \mathrm{TDC5}$).

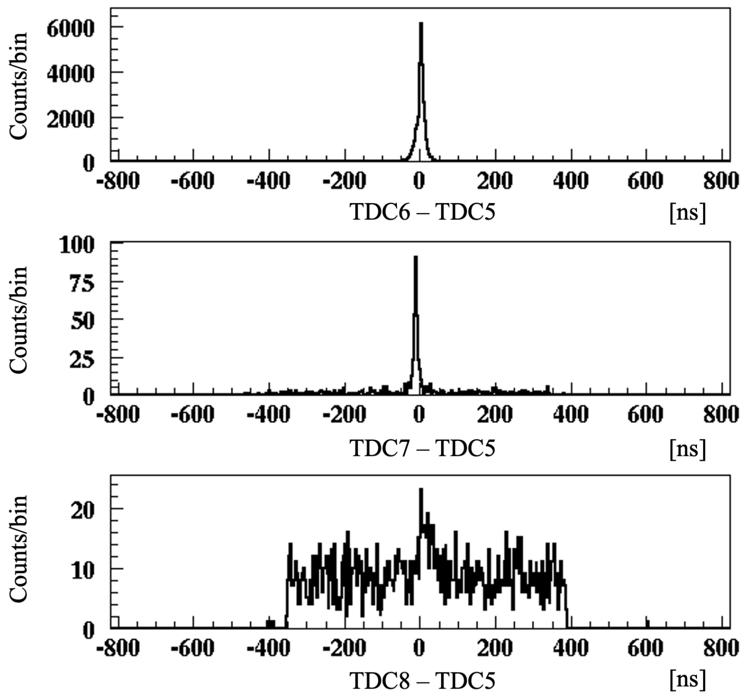

Fig. 5.18: The timing difference between the first layer's timing signal and other layers for 30° detectors.

The time-difference peaks were used to gate the energy in two-dimensional histograms, covering time ranges of -100 ns to 100 ns, to select proton events from the $^7\mathrm{Be}(d,p)^8\mathrm{Be}$ reaction that reached the fourth layer.

Fig. 5.19 depicts ΔE_7 - ΔE_6 and ΔE_8 - ΔE_7 two-dimensional histograms after applying the timing gates.

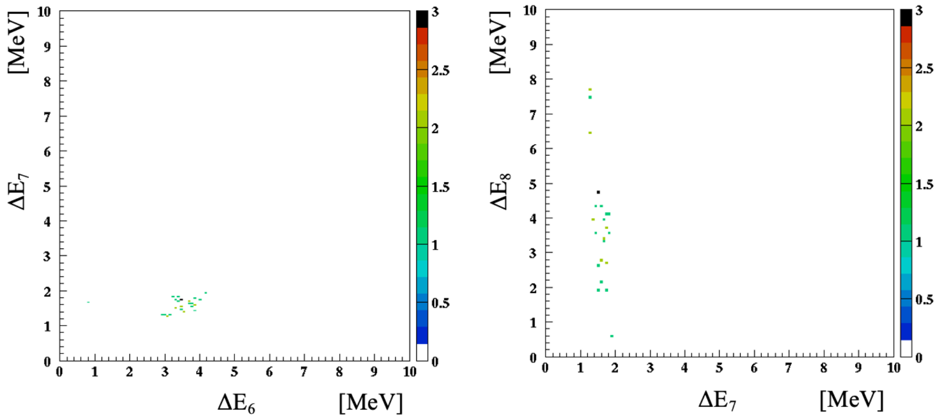

Fig. 5.19: Selected ΔE_7 - ΔE_6 and ΔE_8 - ΔE_7 plots at 30° from the silicon detectors. (Left) The third layer vs. The second layer; (Right) The fourth layer vs. The third layer.

As shown in Fig. 5.19, a gain shift occurred at the energy of the third layer at higher energy, despite the fourth layer energies being reasonable. The energy of the third layer was not usable to reconstruct the total proton energy.

Proton Energy Spectrum by the Measurement at $E_d = 0.6$ MeV, @30°

Fig. 5.20 depicts the reconstructed proton energy spectrum using the fourth layer energy.

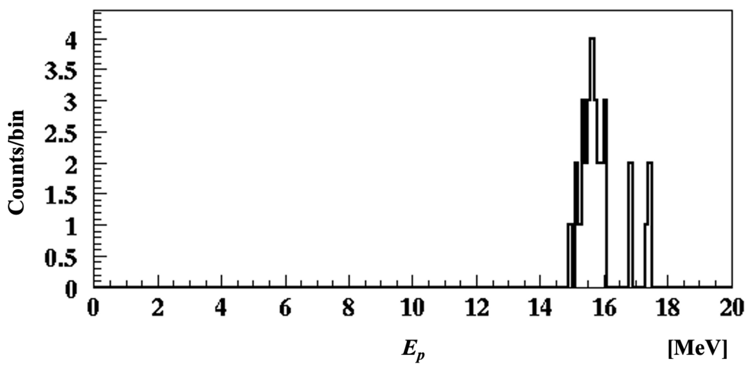

Fig. 5.20: The proton energy spectrum reconstructed by the fourth layer energy.

Chapter 6

Simulations of the $^{7}\mathrm{Be}(d,p)^{8}\mathrm{Be}$ Reaction and Fittings

6.1 Why the Simulations are Necessary?

In the typical case, the measured yield corresponds to the cross section, taking into account the beam current, the target number, and the solid angle. However, the $^{7}\mathrm{Be}(d,p)^{8}\mathrm{Be}$ reaction was measured by the thick target method. In the thick target method, the energy of the outgoing particle, protons in our measurement case, was measured in duplicate due to the finite energy of the incident beam. The finite energy of the incident beam corresponded to the energy loss in the thick target and the target depth. Thus, simulations were conducted to distinguish the proton spectra resulting from the multiple reactions at the different incident energies represented by the target thickness.

The thin target example was considered the initial step in explaining the simulation part before expanding the explanation to the thick target. The differential cross section is calculated by the following Eq. (6.1).

$$\frac{\mathrm{d}\sigma}{\mathrm{d}\Omega} = \frac{Y}{I_b N_t \Omega}. \tag{6.1}$$

Here, Y is the yield, Ω is the solid angle of the detector, I_b is the incident number of beam ions, and N_t is the number of the target nuclei. This experiment was performed using the thick target method. The detected yields per proton energy bin overlapped through the broad incident deuteron energy. Fig. 6.1 shows what happened during the experiment schematically. Those colored proton energy distributions were not separately measured; they were detected in one distribution.

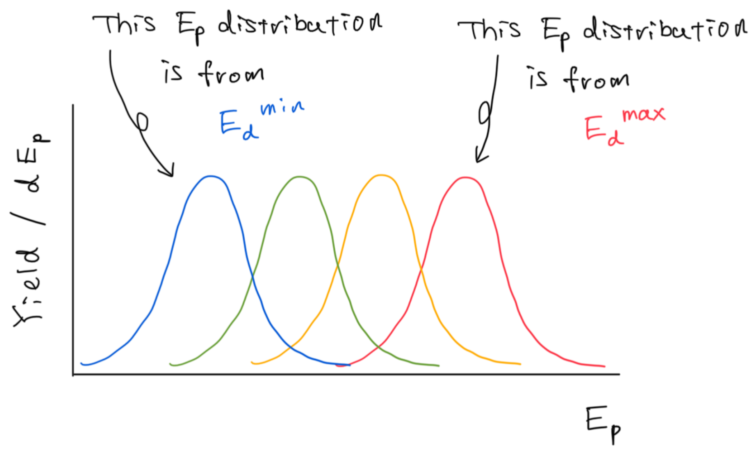

Fig. 6.1: The incident deuteron energy is from E_d^{min} to E_d^{max}. The detected proton energy (E_p) distribution will be overlapped by each colored E_p distribution from different incident deuteron energy (E_d).

If we want to obtain one cross section value in this broadened incident deuteron energy region, we can count the total yield in this proton energy distribution. However, if we want to obtain the cross section in each deuteron energy region, simulations are necessary to produce the fitting functions in the broadened incident deuteron energies. Those simulated distributions are the functions that fit the measured proton energy distribution to obtain separated cross sections in each deuteron energy region.

6.2 Outgoing Proton Energy Distribution $P(E_p)$

The outgoing proton energy (E_p) distribution of the yield is expressed as P. When the emitted proton energy is E_p, the number of protons per unit of energy is described by the following Eq. (6.2).

$$P\left(E_p\right) = \frac{dY_{total}}{dE_p}. \tag{6.2}$$

(6.2) transforms to next Eq. (6.3),

$$P(E_p) \cdot dE_p = dY_{total}. \tag{6.3}$$

The left side of Eq. (6.3) is the number of outgoing proton events measured in the tiny width dE_p. dY_{total} on the right side is a small yield. Let's consider the physical quantity of Eq. (6.3) and calculate the fitting function.

6.3 When the ^{7}Be Target is Very Thin and the Incident Deuteron Beam is a Single Energy

6.3.1 Outgoing Proton Yield

The yield Y_{total} of the outgoing proton event from the $^7\mathrm{Be}(d,p)^8\mathrm{Be}$ reaction is described below,

$$Y_{total} = I_d \times \frac{N_{^7Be}}{S_p} \times \sigma_{dp} \times \frac{\Omega}{4\pi}. \tag{6.4}$$

Here, I_d is the number of incident deuteron beams, $N_{^7\mathrm{Be}}$ is the number of $^7\mathrm{Be}$ targets, S_p is the area where ^{7}Be targets are distributed, Ω is the solid angle covered by the Si telescope detector, and σ_{dp} is the $^7\mathrm{Be}(d,p)^8\mathrm{Be}$ reaction cross section, assuming no dependence on E_d. ^{7}Be targets were produced via. $^7\mathrm{Li}(p,n)^8\mathrm{Be}$ reaction. S_p corresponds to the incident proton beam spot size during the target production.

One note is that the deuteron beam diameter was larger than the ^{7}Be target area. Thus, all ^{7}Be targets were used for the reaction; however, not all deuteron beam particles in the beam spot size were used.

Let the deuteron beam spot area be S_d, the total readout beam charge of deuterons be $C_d[\mathrm{C}]$, and the elementary charge $e[\mathrm{C}]$. Then, the number of deuteron beams I_d used in the reaction is described in the following Eq. (6.5).

$$I_d = \frac{C_d}{e} \cdot \frac{S_p}{S_d}. \tag{6.5}$$

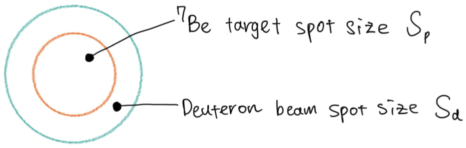

Fig. 6.2: Relationship between the ^{7}Be target diameter and deuteron beam diameter.

6.3.2 Excitation Energy Strength Function of the ^{8}Be

In the $^7\mathrm{Be}(d,p)^8\mathrm{Be}$ reaction, the emitted proton energy E_p is thought to have a distribution that reflects the strength function of the excitation energy of ^{8}Be. Here, we define the form of the intensity function of the excitation energy of ^{8}Be. When the strength function of excitation energy E_x has a center value μ and width Γ, the function can be expressed as follows.

$$f\left(E_x;\mu,\Gamma\right). \tag{6.6}$$

The reason why the detected proton energy E_p is being broadened is that the strength function of the excitation energy E_x of ^{8}Be has a range.
Also, the outgoing proton energy is obtained from the excitation energy E_x of ^{8}Be by solving the kinematics equation by giving the deuteron implantation energy E_d.

$$E_p = k\left(E_x;E_d\right). \tag{6.7}$$

Here, in the excitation energy intensity function of ^{8}Be, the probability that the excitation energy is within the range of $[E_x, E_x + dE_x]$ is given by the following Eq. (6.8).

$$f\left(E_x\right)\cdot dE_x. \tag{6.8}$$

There is a relationship (6.7) between the excitation energy E_x of ^{8}Be and the emitted proton energy E_p. Since E_x and E_p correspond when the excitation energy is within the range of $[E_x, E_x + dE_x]$, the expected exit proton energy in the range of E_p is dE_p. This is expressed in (6.9) using E_x.

$$dE_p = k\left(E_x + dE_x; E_d\right) - k\left(E_x; E_d\right). \tag{6.9}$$

6.3.3 Number of Outgoing Proton Events within the Range of Infinitesimal Energy dE_p and Fitting Function

When the probability is $f\left(E_x\right) dE_x$, the outgoing proton events measured in the range $dE_p\left(= \left[E_p, E_p + dE_p\right]\right)$ are shown in Eq. (6.10). This means the probability is multiplied by the total proton events Y_{total}.

$$P\left(E_p\right) \cdot dE_p = Y_{total} \times f\left(E_x\right) \cdot dE_x = I_d \times \frac{N_{^7Be}}{S_p} \times \sigma_{dp} \times \frac{\Omega}{4\pi} \times f\left(E_x\right) \cdot dE_x. \tag{6.10}$$

The right side of Eq. (6.10) is also transformed to the shape it is expressed as a function of the emitted proton energy E_p.

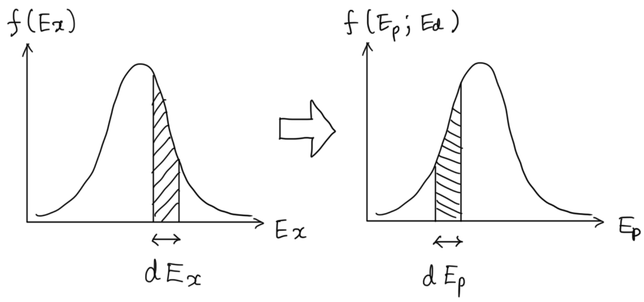

Fig. 6.3: Differentiation of small intervals.

The left side of Fig. (6.3) represents the probability density function at excitation energy E_x. The probability in a certain small interval dE_x is expressed as $f\left(E_x\right) \cdot dE_x$. According to Eq. (6.7), the excitation energy E_x is expressed by the proton energy E_p and the deuteron beam energy E_d. The minute interval dE_x corresponds to the minute interval dE_p. The intensity function $F\left(E_p; E_d\right)$ of proton energy E_p is defined as the following condition: the probability that events arrive in the infinitesimal interval dE_x and the probability that events arrive in the infinitesimal interval dE_p are the same. Then the following Eq. (6.11) holds.

$$f\left(E_x\right) \cdot dE_x = F\left(E_p; E_d\right) \cdot dE_p. \tag{6.11}$$

Substitute Eq. (6.11) for Eq. (6.10).

$$P\left(E_p\right) \cdot dE_p = Y_{total} \times f\left(E_x\right) \cdot dE_x = I_d \times \frac{N_{^7Be}}{S_p} \times \sigma_{dp} \times \frac{\Omega}{4\pi} \times F\left(E_p; E_d\right) \cdot dE_p. \tag{6.12}$$

The fitting function of the experimental results is defined as the distribution of the outgoing proton energy E_p in terms of the number of detected outgoing protons per unit energy (counts/ch). Take dE_p from both sides of Eq. (6.12).

$$P\left(E_p\right) = I_d \times \frac{N_{^7Be}}{S_p} \times \sigma_{dp} \times \frac{\Omega}{4\pi} \times F\left(E_p; E_d\right). \tag{6.13}$$

6.3.4 Thick Target Method

In the case of the thick target method, the ^{7}Be target has a distribution, and the incident deuteron beam energy is not single because the deuteron beam drops its energy while pathing through (or stopping) the host target. This situation must be included in the simulations.

6.3.5 ^{7}Be Target Distribution

The ^{7}Be targets have a distribution in the depth direction of the host target (nat. Li) and are not uniform. This is due to the production method of the ^{7}Be target. When the ^{7}Be target was produced, we selected the ^{7}Li(p, n)^{7}Be reaction. The proton beam irradiated on the nat. Li target, and the ^{7}Be target production was supposed to follow the cross-section distribution of the ^{7}Li(p, n)^{7}Be reaction. Assuming that the function of the ^{7}Li(p, n)^{7}Be reaction cross section is a function of the incident proton beam energy

E_p^{trg}, let it be $\sigma_{pn}\left(E_p^{trg}\right)$. E_p^{trg} is expressed as a function of depth (z) using the function of the proton energy loss in the Li host target, i.e. $\sigma_{pn}\left(E_p^{trg}(z)\right)$. This is written as $\sigma_{pn}(z)$ for simplicity.

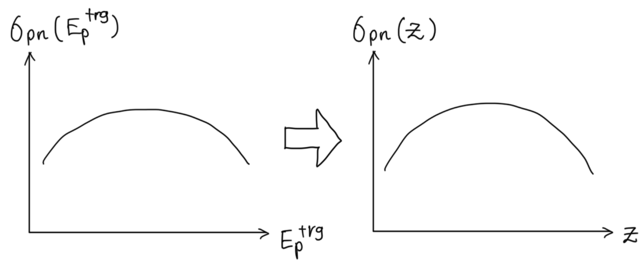

Fig. 6.4: The horizontal axis of the ^{7}Li$(p, n)^7$Be reaction cross-section function was transformed from the incident proton energy (E_p^{trg}) to the depth (z).

The volume of nat. Li is $\rho_{nat.Li}[\mathrm{g/cm^2}]$, the atomic weight of nat. Li is $g[\mathrm{g/mol}]$, the Avogadro number is N_A, and let $a_{^7Li}$ be the mass ratio of ^{7}Li. The number of ^{7}Li per unit volume $v_{^7Li}$ is expressed by Eq. (6.14).

$$v_{^7Li} = \rho_{\text{nat.Li}} \times \frac{1}{g} \times N_A \times a_{^7Li}. \tag{6.14}$$

The unit of $v_{^7Li}$ is $\mathrm{g/cm^3}$. When the number of incident protons is I_p, the number of $^7\mathrm{Be}$ per unit length $u_{^7Be}(z)$ is expressed by Eq. (6.15).

$$u_{^7Be}(z) = I_p \times v_{7Li} \times \sigma_{pn}(z). \tag{6.15}$$

The unit of $u_{^7Be}(z)$ is $\mathrm{g/cm}$. When the spot size of the proton beam is S_p, the volume density of ^{7}Be can be expressed as Eq. (6.16) using Eq. (6.14).

$$\frac{u_{^7Be}(z)}{S_p}. \tag{6.16}$$

Number of Outgoing Proton Events in the Range of Infinitesimal Energy dE_p and Fitting Function

If the thickness of the target is t, the areal density of the target is expressed as $\int_0^t \frac{u_{^7Be}(z)}{S_p} dz$. According to Eq. (6.12), $P\left(E_p\right) \cdot dE_p$ is expressed as Eq. (6.17), when the ^{7}Be target has a distribution in the depth direction.

$$P\left(E_p\right) \cdot dE_p = \int_0^t \left\{F\left(E_p; E_d\right) \cdot dE_p\right\} \cdot I_d \cdot \frac{u_{^7Be}\left(z\right)}{S_p} \cdot \sigma_{dp} dz. \tag{6.17}$$

The function $F\left(E_p; E_d\right)$ must be placed in $\int_0^t dz$, since the deuteron energy is also a function of the depth z.

The fitting function of the experimental results is expressed as Eq. (6.18), which is defined as the distribution of the outgoing proton energy E_p in terms of the number of detected emitted protons per unit energy (counts/ch).

$$P\left(E_p\right) = \int_0^t F\left(E_p; E_d\right) \cdot I_d \cdot \frac{u_{^7Be}\left(z\right)}{S_p} \cdot \sigma_{dp} dz. \tag{6.18}$$

The cross section is described as Eq. (6.19) using the astrophysical S-factor [36].

$$\sigma_{dp}(E_{c.m.}) = S(E_{c.m.}) \cdot \frac{1}{E_{c.m.}} \cdot \exp(-2\pi\eta). \tag{6.19}$$

The fitting functions (6.18) were simulated for each incident deuteron energy bin (ΔE_d).

6.4 Simulation Segmentation

The fitting function is shown in Eq. (6.18). The fitting functions were simulated based on a range segmented according to the ^{7}Be target sectors, considering the reaction that occurred at specific thicknesses of the ^{7}Be target. A simulation was performed, assuming the stacking of multiple thin targets. The thick target method employed an analytical approach to examine a thick target by treating the target as a superposition of several thin targets. The segmentation was determined based on the deuteron energy resolution. Deuteron energies for each target thickness were calculated using the detected proton energy. Thus, the proton energy resolution corresponded to the deuteron energy resolution. The proton energy resolution was attributed to two main effects: the intrinsic energy resolution of the silicon detectors $\Delta E_p^{res.}$ and the proton energy straggling within the silicon detectors and the Cu absorber $\Delta E_p^{str.}$. $\Delta E_p^{res.}$ and $\Delta E_p^{str.}$ were converted to represent the deuteron energy resolutions, $\Delta E_d^{res.}$ and $\Delta E_d^{str.}$. Another effect that caused deuteron energy spread was the uncertainty of the detected proton angle, attributed to the limited position sensitivity and angular resolution of the silicon detectors. While the deuteron energy was calculated based on the detected proton energy, the angular information was essential for solving the kinematics. The deuteron energy spread, denoted as $\Delta E_d^{ang.}$, was also simulated, taking into account the angular spread. $\Delta E_d^{res.}$, $\Delta E_d^{str.}$, and $\Delta E_d^{ang.}$ were considered separately and propagated. The details are presented below.

6.4.1 $\Delta E_d^{res.}$ from Intrinsic Energy Resolution of the Silicon Detectors $\Delta E_p^{res.}$

The original proton energy at the reaction point in the $^7\mathrm{Be}$ target was calculated based on the energy detected in the third and/or fourth-layer silicon detectors. Consequently, the proton energy resolution was attributed to the intrinsic energy resolution of either the third- or fourth-layer silicon detectors. The intrinsic resolutions of the silicon detectors were determined using proton two-dimensional spectra. The spread of the locus represented the energy resolution, encompassing contributions from both the third and fourth silicon detectors.

To determine the intrinsic energy resolution of the third and fourth silicon detectors, the ratio of resolutions between the third and fourth detectors was estimated using the alpha-checking source spectra. The same analysis method was applied to all silicon detectors, including the third and fourth ones, at both 45 and 30 degrees. The analysis for E_d = 1.6 MeV and 45-degree detectors is presented below as a typical example.

Figs. 6.5 and 6.6 display the alpha energy spectra obtained from energy calibration measurements of the third and fourth-layer silicon detectors at angles of 45 degrees.

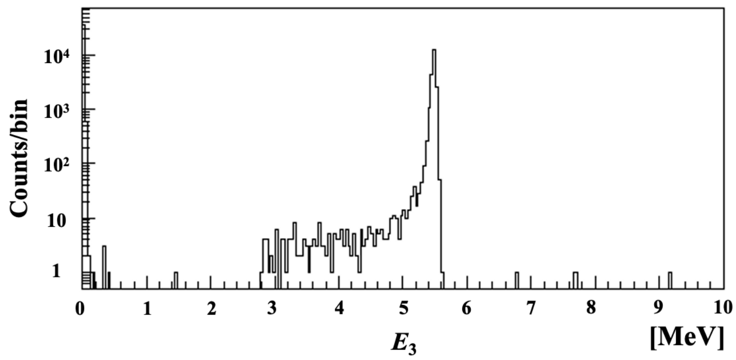

Fig. 6.5: The energy spectrum of the third-layer silicon detector obtained with the alpha-checking source.

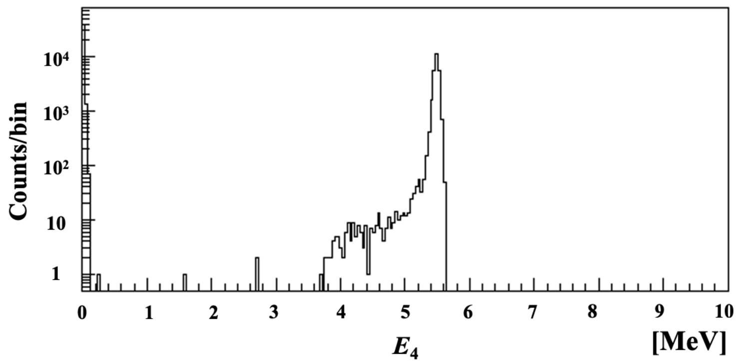

Fig. 6.6: The energy spectrum of the fourth-layer silicon detector obtained with the alpha-checking source.

The spectra were fitted with Gaussian functions, and the width in sigma of the energy peak for the third layer (ΔE_3) was 0.0252 MeV, while the width in sigma of the energy peak for the fourth layer (ΔE_4) was 0.0358. E_3 and E_4 represented the energy measurements from the third and fourth layers at 45 degrees, respectively. The relationship between ΔE_3 and ΔE_4 is expressed by the following Eq. (6.20).

$$\Delta E_4 = 1.420 \times \Delta E_3. \tag{6.20}$$

The ratio of ΔE_3 and ΔE_4 was assumed to maintain consistency across the proton energy.

Fig. 6.7 shows the locus of E_4 vs. E_3. The dashed line in Fig. 6.7 represents a linear function, $y = -2.15 \cdot x + 16$.

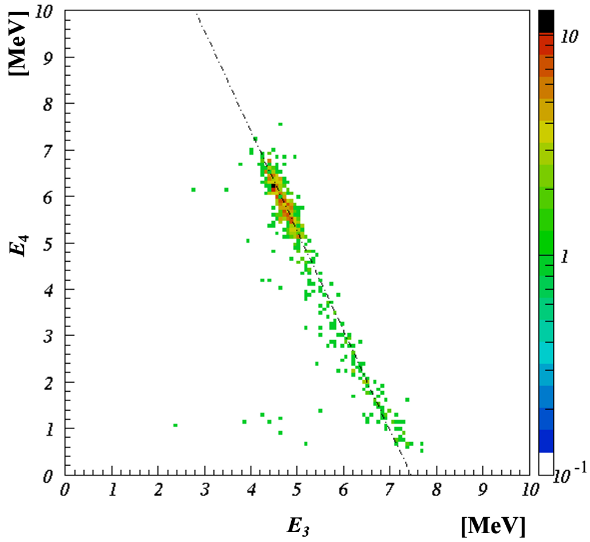

Fig. 6.7: E_4 vs. E_3 locus, and a linear function represents the locus.

The relationship between E_4 and E_3 was assumed to follow the linear function $y = -2.15 \cdot x + 16$. Therefore, E_4 is expressed by Eq. (6.21) below as a function of E_3.

$$E_4 = a_1^{E_d=1.6,45^\circ} \cdot E_3 + a_0^{E_d=1.6,45^\circ} \quad \left(a_1^{E_d=1.6,45^\circ} = -2.15, a_0^{E_d=1.6,45^\circ} = 16\right). \tag{6.21}$$

When Eq. (6.21) is transformed, Eq. (6.22) is obtained.

$$E_3 = \frac{E_4 - a_0^{E_d=1.6,45^\circ}}{a_1^{E_d=1.6,45^\circ}}. \tag{6.22}$$

In order to determine the width of the locus, a parallel projection was made perpendicular to the E_4 axis in the direction of the X-axis. The resulting X-axis projection was denoted as E_3'. E_3' is expressed by the following Eq. (6.23) using E_4 and E_3.

$$E_3' = E_3 - \left(\frac{E_4 - a_0^{E_d=1.6,45^\circ}}{a_1^{E_d=1.6,45^\circ}}\right). \tag{6.23}$$

Eq. (6.24) is obtained by transforming Eq. (6.23).

$$E_3' = E_3 - \frac{1}{a_1^{E_d=1.6,45^\circ}} \cdot E_4 + \frac{a_0^{E_d=1.6,45^\circ}}{a_1^{E_d=1.6,45^\circ}}. \tag{6.24}$$

E_3' represents the projection of the locus of E_4 vs. E_3 onto the X-axis, as depicts in Fig. 6.8.

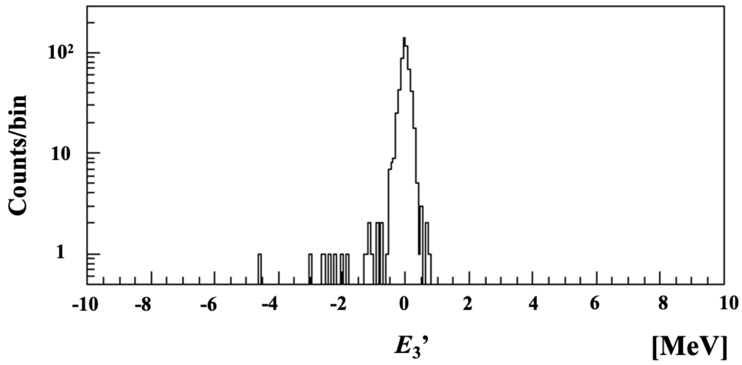

Fig. 6.8: E_3' 1-dimensional histogram.

The E_3' spectrum was fitted with Gaussian function, and the width in sigma of the energy peak $\Delta E_3'$ was 0.144 MeV.

In taking the total derivative of Eq. (6.23), Eq. (6.25) is obtained.

$$\begin{aligned}\Delta E_3' &= \sqrt{\left(\frac{\partial E_3'}{\partial E_3}\right)^2 \cdot (\Delta E_3)^2 + \left(\frac{\partial E_3'}{\partial E_3}\right)^2 \cdot \left(\frac{1}{a_1^{E_d=1.6,45}} \cdot \Delta E_4\right)^2} \\ &= \sqrt{(\Delta E_3)^2 + \left(\frac{1}{\left(a_1^{E_d=1.6,45^\circ}\right)^2}\right) \cdot (\Delta E_4)^2}.\end{aligned} \tag{6.25}$$

From the relationship in Eq. (6.20), then Eq. (6.25) is reformulated as Eq. (6.26).

$$\begin{aligned}\Delta E_3' &= \sqrt{(\Delta E_3)^2 + \left(\frac{1}{\left(a_1^{E_d=1.6,45}\right)^2}\right) \cdot (\Delta E_4)^2} \\ &= \sqrt{(\Delta E_3)^2 + \left(\frac{1}{\left(a_1^{E_d=1.6,45}\right)^2}\right) \cdot (1.420 \times \Delta E_3)^2} \\ &= \sqrt{\left(1 + \frac{1.420^2}{\left(a_1^{E_d=1.6,45}\right)^2}\right) \cdot (\Delta E_3)^2}.\end{aligned} \tag{6.26}$$

Then,

$$\Delta E_3 = \frac{\Delta E_3'}{\sqrt{\left(1 + \frac{1.420^2}{a_1^{E_d=1.6,45^\circ 2}}\right)}}. \tag{6.27}$$

$\Delta E_3'$ in sigma was obtained by the fitting (= 0.144 MeV), and $a_1^{E_d=1.6,45^\circ} = -2.15$. When ΔE_3 is calculated, ΔE_4 is also obtained by Eq. (6.20).

ΔE_4 and ΔE_3 were converted to the proton resolution.

Figs. 6.9 and 6.10 depict the relationship between E_p and E_3, as well as E_p and E_4. In Fig. 6.9, the green line represents stopped proton events within the third-layer silicon detector, while the orange line signifies penetration proton events in the third-layer silicon detector. Fig. 6.10 shows the blue line, illustrating stopped events in the fourth layer. The loci were fitted by polynomial functions, and the results are shown below.

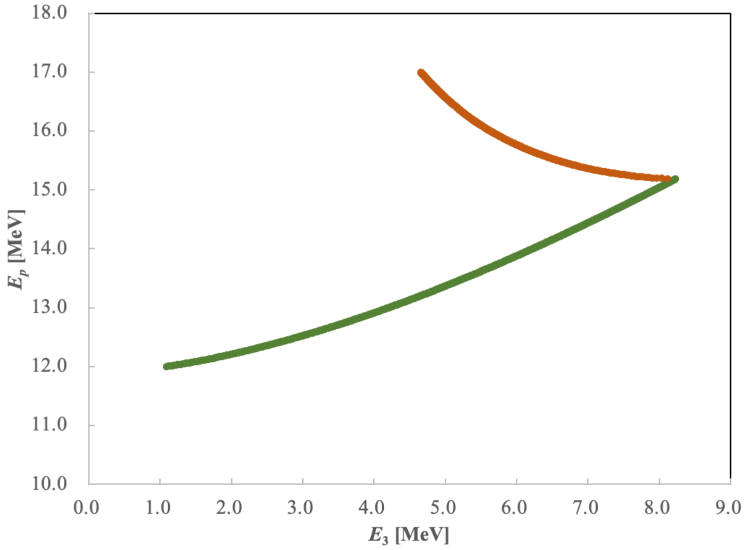

Fig. 6.9: Simulated function of E_p vs. E_3 energy deposit.

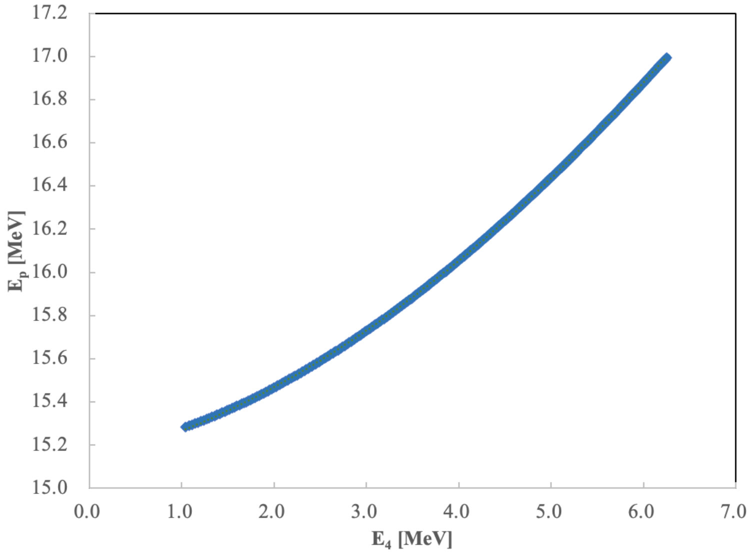

Fig. 6.10: Simulated function of E_p vs. E_4 energy deposit.

The fitting results of events that stopped at the third layer (green), the fitting result of events that penetrated the third layer (orange), and the fitting result of events that stopped at the fourth layer (blue) are shown in Eqs. (6.28), (6.29), and (6.30).

$$E_p = 0.0295 \cdot E_3^2 + 0.179 \cdot E_3 + 11.7. \tag{6.28}$$

$$E_p = 0.192 \cdot E_3^2 + 2.92 \cdot E_3 + 26.4. \tag{6.29}$$

$$E_p = 0.0300 \cdot E_4^2 + 0.112 \cdot E_4 + 15.1. \tag{6.30}$$

When determining the variation in E_p from E_3 or E_4, these were obtained by evaluating the first-order derivatives of Eqs. (6.28), (6.29), and 6.30. The expressions for the first-order derivatives are given by Eqs. (6.31), (6.32), and (6.33), respectively.

$$\Delta E_p = 0.0295 \cdot \Delta E_3 + 0.179. \tag{6.31}$$

$$\Delta E_p = 0.192 \cdot \Delta E_3 + 2.92. \tag{6.32}$$

$$\Delta E_p = 0.0300 \cdot \Delta E_4 + 0.112. \tag{6.33}$$

Eqs. (6.31), (6.32), and (6.33) represent the Jacobians converting E_3 or E_4 to E_p. The proton resolution calculated by E_4 is denoted $\Delta E_p^{res,E4}$, and by E_3 is denoted $\Delta E_p^{res,E3}$. Tables 6.1 and 6.2 display the proton energy resolution in all measurement setups calculated by the intrinsic third or fourth silicon detector. The alpha-energy calibration data were obtained for different deuteron incident energies.

Table 6.1: The proton energy resolution $\Delta E_p^{res.}$ converted from the intrinsic third- and fourth-layer detector resolution.

E_d [MeV]	Detector angle [deg.]	ΔE_3 [MeV]	ΔE_4 [MeV]	$\Delta E_p^{res,E_3}$ [MeV]	$\Delta E_p^{res,E_4}$ [MeV]
1.6	45	0.120	0.171	0.0393	0.0397
0.6	45	0.120	0.144	0.0393	0.283

Table 6.2: Summary of the silicon detector efficiencies.

E_d [MeV]	Detector angle [deg.]	ΔE_7 [MeV]	ΔE_8 [MeV]	$\Delta E_p^{res,E_7}$ [MeV]	$\Delta E_p^{res,E_8}$ [MeV]
1.6	30	0.645	0.822	0.2256	0.197
0.6	30	0.171	0.231	0.0597	0.0554

Figs. 6.11 and 6.12 show the relationship between E_d vs. E_p considering the dp_0 reaction and E_d vs. E_p considering dp_1. Most of the proton energies that reached the fourth-layer silicon detector corresponded to the dp_0 reaction, while those stopped at the third-layer silicon detector were considered to correspond to the dp_1 reaction.

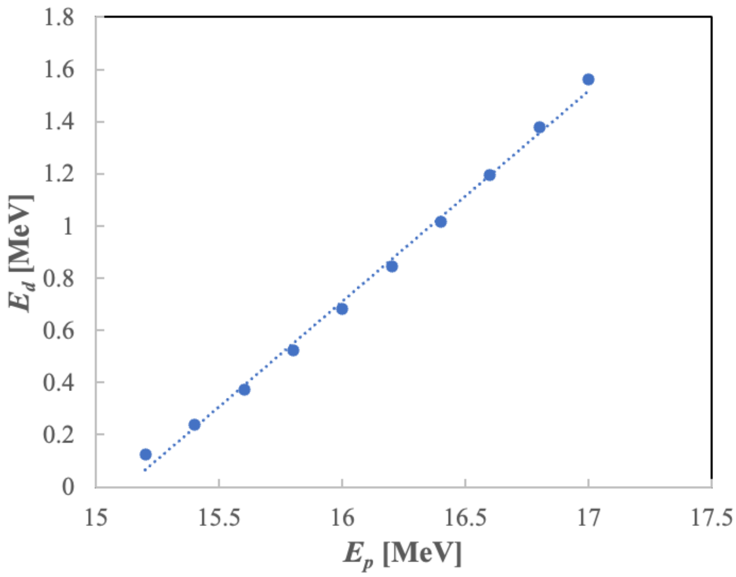

Fig. 6.11: The kinematical relation ship between E_p and E_d assuming the dp_0 reaction.

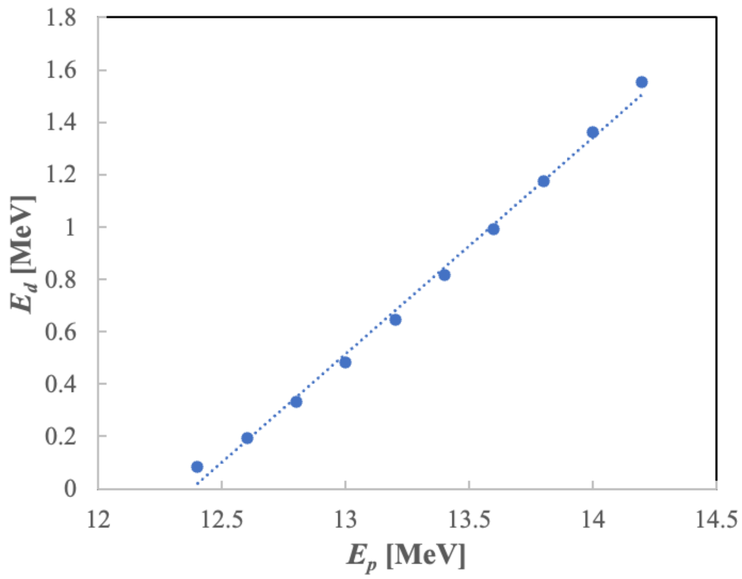

Fig. 6.12: The kinematical relation ship between E_p and E_d assuming the dp_1 reaction.

Eqs. (6.34) and (6.35) expresse the fitted E_d as polynomial functions of E_p.

$$E_d = 0.807 \cdot E_p - 12.2. \tag{6.34}$$

$$E_d = 0.827 \cdot E_p - 10.2. \tag{6.35}$$

The first-order derivatives of Eqs. 6.34 and 6.35 are given by Eqs. (6.36) and (6.37), representing the Jacobian conversions from ΔE_p to ΔE_d.

$$(\frac{dE_d}{dE_p})_{dp_0} = 0.807. \tag{6.36}$$

$$(\frac{dE_d}{dE_p})_{dp_1} = 0.827. \tag{6.37}$$

Using the Jacobians in Eqs. (6.36) and (6.37), $\Delta E_p^{res.}$ values were converted to $\Delta E_d^{res.}$ for both events arrived at the fourth layer and stopped in the third layer of silicon detectors. The resulting $\Delta E_p^{res.}$ and $\Delta E_d^{res.}$ in case of the conversion from E_3 to E_p and E_4 to E_p values are summarized in Table 6.3. The events that arrived in the fourth layer silicon detector represented *Fourth*, and the events stopped at the third layer of silicon detector represented *Third* to make the display short in the table.

Table 6.3: The deuteron energy resolution $\Delta E_d^{res.}$ converted from the proton energy resolution $\Delta E_p^{res.}$.

Incident E_d [MeV]	Detector angle [deg.]	Event type	Expected reaction	ΔE_p^{res} [MeV]	ΔE_d^{res} [MeV]
1.6	45	*Fourth*	dp_0	0.0397	0.0321
		Third	dp_1	0.0393	0.0325
0.6	45	*Fourth*	dp_0	0.2826	0.228
		Third	dp_1	0.0393	0.0325
1.6	30	*Fourth*	dp_0	0.197	0.159
		Third	dp_1	0.226	0.187
0.6	30	*Fourth*	dp_0	0.0554	0.0447
		Third	dp_1	0.0597	0.0494

6.4.2 $\Delta E_d^{str.}$ from Proton Energy Straggling $\Delta E_p^{str.}$

The proton energy straggling was calculated using LISE++ [37, 38]. Both straggling effects were considered, accounting for the Cu absorber placed just before the detector and the straggling within the silicon detectors. The straggling values for events stopping at the third layer, with a typical value of 14.0 MeV, and for events stopping at the fourth layer, with a typical value of 16.5 MeV, are summarized in Table 6.4.

Table 6.4: The proton straggling $\Delta E_p^{str.}$s calculated by LISE++ [37, 38].

Typical E_p [MeV]	Straggling [MeV]
14.0	0.163
16.5	0.261

The proton energy spread, accounting for proton straggling, was transformed into deuteron energy spread using the Jacobians presented in Eqs. (6.36) and (6.37). The resulting $\Delta E_p^{str.}$ and $\Delta E_d^{str.}$ for events involving protons that either arrived at the fourth layer or stopped at the third layer are tabulated in Table 6.5. The designations *Fourth* and *Third* are used to represent events that arrived at the fourth-layer silicon detector and those that stopped at the third-layer silicon detector, respectively, for a concise presentation in the table.

Table 6.5: The deuteron energy spread considering the proton straggling in the detector.

Event type	Expected reaction	ΔE_p^{res} [MeV]	ΔE_d^{res} [MeV]
Fourth	dp_0	0.261	0.211
Third	dp_1	0.163	0.135

6.4.3 Deuteron Energy Spread $\Delta E_d^{ang.}$ Caused by Detector Angular Uncertainty

The uncertainty in determining the deuteron energy for proton events stopping at the third and fourth layers arose from the uncertainty in the detection angle of protons in the third- and fourth-layer silicon detectors. The original proton energy from the $^7\mathrm{Be}(d,p)^8\mathrm{Be}$ reaction occurring in the target was calculated based on the energy deposit at the third or/and fourth layer, taking into account the energy loss processes with materials before reaching the third- and fourth-layer silicon detector. Kinematic calculations were employed to convert the original proton energy into deuteron energy, with the angle introducing inherent uncertainty. The angular uncertainty was modeled in a way that the detected proton angle by the silicon detector followed a uniform distribution between the minimum and maximum angles of the detector. When calculating deuteron energy from proton energy at the reaction point, the spread of deuteron energy was simulated by introducing the detector installation angler distribution.

The detector's angular distributions (angular coverage) are depicted in both Figs. 6.13 and 6.14, represented in both degrees and radians.

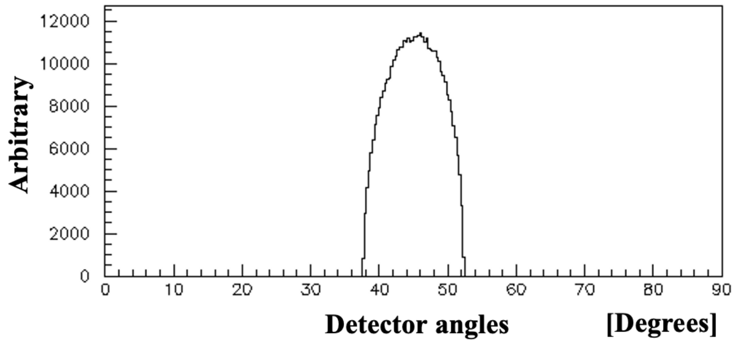

Fig. 6.13: The 45 ° detector angular distribution in degrees.

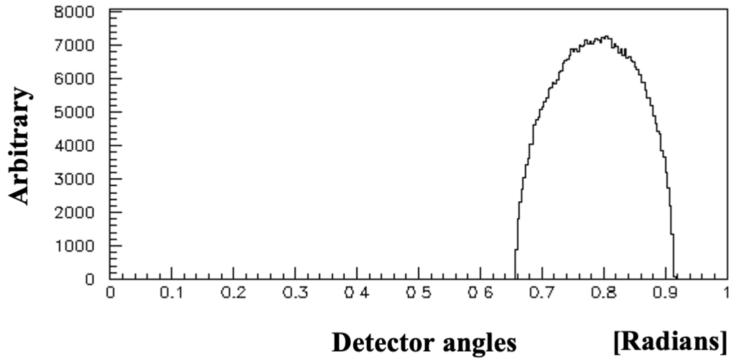

Fig. 6.14: The 45 ° detector angular distribution in radians.

Most of the proton energies reaching the fourth-layer silicon detector corresponded to the dp_0 reaction, while those stopped at the third-layer silicon detector were considered to correspond to the dp_1 reaction. Consequently, proton events that reached the fourth layer and stopped at the third layer were simulated separately, allowing for the calculation of the spread of deuteron energy. The detectors at 45 degrees and 30 degrees had distinct solid angles, necessitating separate simulations for their angular distributions. Fig. 6.15 depicts the deuteron spread resulting from proton events that reached the fourth layer at 45 degrees. Fig. 6.16 depicts the deuteron spread from proton events that stopped at the third layer at 45 degrees. Similarly, Fig. 6.17 displays the deuteron spread from proton events that reached the fourth layer at 30 degrees, and Fig. 6.18 shows the deuteron spread from proton events that stopped at the third layer at 30 degrees.

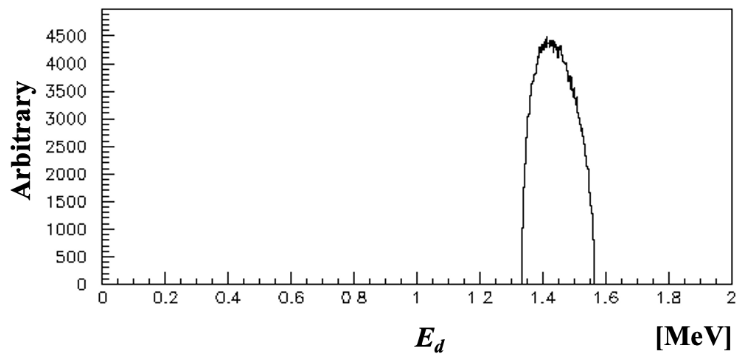

Fig. 6.15: Simulated incident energy spread E_d in case the outgoing proton was detected in the fourth layer at 45° detector.

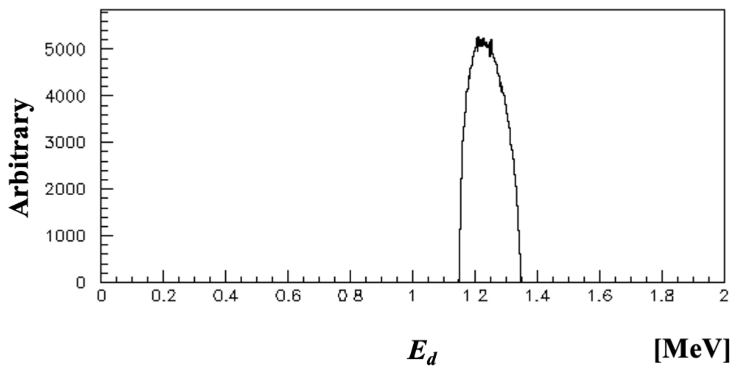

Fig. 6.16: Simulated incident energy spread E_d in case the outgoing proton was detected in the third layer at 45° detector.

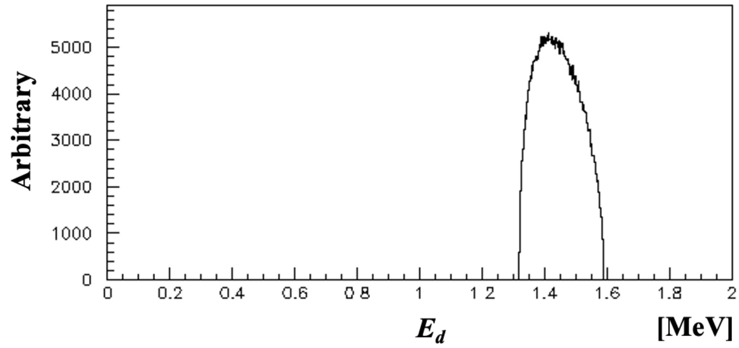

Fig. 6.17: Simulated incident energy spread E_d in case the outgoing proton was detected in the fourth layer at 30° detector.

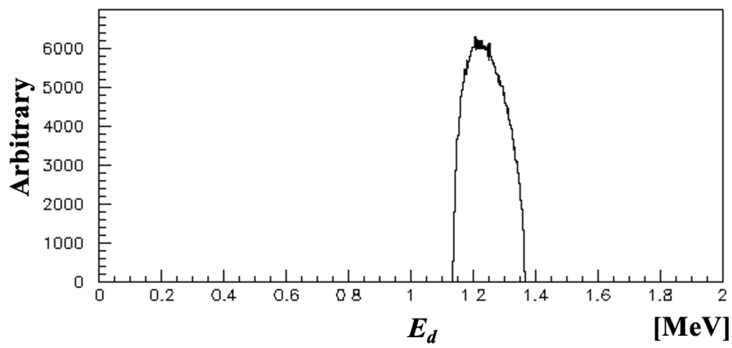

Fig. 6.18: Simulated incident energy spread E_d in case the outgoing proton was detected in the third layer at 30° detector.

The detector angle, expected excited energy (of ^{8}Be), and the deuteron energy angular spread are summarized in Table 6.6.

Table 6.6: The deuteron energy angular spread.

Theta angle [Degrees]	Excited energy of ^{8}Be [MeV]	$\Delta E_d^{ang.}$
45	0.0	0.0871
45	3.03	0.0697
30	0.0	0.0658
30	3.03	0.0401

6.4.4 Total Deuteron Energy Spread ΔE_d^{total}

$\Delta E_d^{res.}$, $\Delta E_d^{str.}$, and $\Delta E_d^{ang.}$ were treated as independent. Consequently, the total energy spread of the deuteron, ΔE_d^{total} was computed by propagating the errors of $\Delta E_d^{res.}$, $\Delta E_d^{str.}$, and $\Delta E_d^{ang.}$. The values are summarized in Table 6.7, presenting the ultimate deuteron energy spread for each experimental setup.

Table 6.7: The summary of total deuteron energy spreads $\Delta E_p^{res.}$ for each measurement setup.

Incident E_d [MeV]	Detector angle [deg.]	Event type	Expected reaction	ΔE_d^{total} [MeV]
1.6	45	*Fourth*	dp_0	0.230
		Third	dp_1	0.156
0.6	45	*Fourth*	dp_0	0.273
		Third	dp_1	0.156
1.6	30	*Fourth*	dp_0	0.272
		Third	dp_1	0.234
0.6	30	*Fourth*	dp_0	0.225
		Third	dp_1	0.149

In comparing the results of ΔE_d^{total} in each experimental setup with the values at each incident deuteron energy E_d, the number of simulation segments ranged between 2 and 3.

6.5 Fitting Functions

The simulations for calculating the fitting functions were consistently conducted for each deuteron energy ($E_d = 1.6$ and 0.6MeV) and detector angles (at 45 and 30 degrees). Here, the simulation for the measurements at $E_d = 1.6$ MeV and at 45 degrees are shown below as typical cases.

In 6.4, deuteron energy spreads were estimated, and simulation segmentations were defined. In Table 1, the deuteron energy spread was 0.230 MeV for the dp_0 reaction and 0.156 MeV for the dp_1 reaction at $E_d = 1.6$ MeV and a measurement angle of 45 degrees. When the incident deuteron energy was 1.6 MeV, the deuteron beam penetrated the $^7\mathrm{Be}$ target, resulting in an energy deposit of $0.46\ \mathrm{MeV}$. Consequently, segmentations should be two for the dp_0 reaction and three for the dp_1 reaction. However, the segmentation was ultimately decided to be three for both dp_0 and dp_1 reactions. The deuteron energy spread was assumed to be $0.15\ \mathrm{MeV}$ when the segmentation was set to three. The $^7\mathrm{Be}$ thickness was segmented into three regions: *Region 1*, *Region 2*, and *Region 3*. The simulation was conducted with a specific $^7\mathrm{Be}$ target thickness, with the depth z of the target being the variable. Deuteron energies were converted to the depth of the $^7\mathrm{Be}$ target using the energy loss and range function shown in Fig. 6.19.

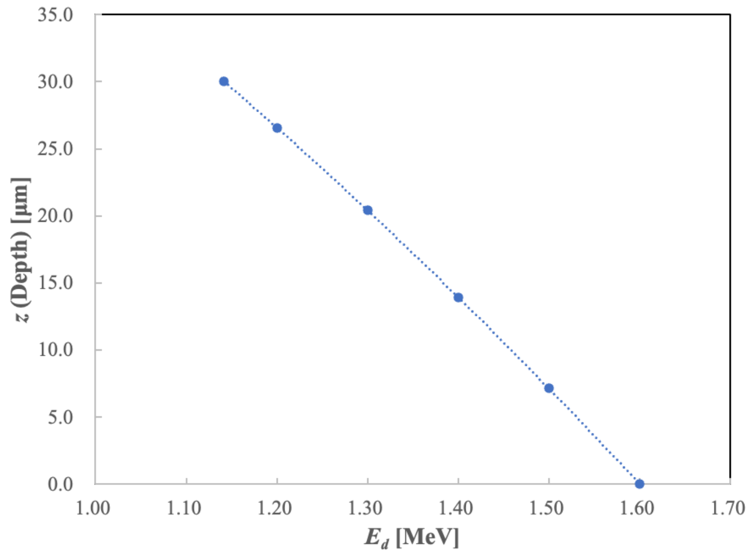

Fig. 6.19: The relationship between the depth z and the incident deuteron beam energy E_d.

The curve of z vs. E_d depicted in Fig. 6.19 was fitted with a second-order polynomial 6.38.

$$z = -16.0 \cdot E_d^2 - 21.5 \cdot E_d + 75.5. \tag{6.38}$$

Using Eq. (6.38), the deuteron energies in the target were converted to the depth z. Table 6.8 summarizes the relationship between deuteron energy and the corresponding depth z with the $^7\mathrm{Be}$ regions.

Table 6.8: Correspondence between the depth z and the incident deuteron beam energy E_d.

Region	Incident E_d [MeV]	$z[\mu m]$
Region 1	1.60	0.00
	1.45	10.8
Region 2	1.45	10.8
	1.29	20.8
Region 3	1.29	20.8
	1.14	30.0

The $^7\mathrm{Be}$ target distributions in each region were also considered and are depicted in Figs. 6.20, 6.21, and 6.22 for Regions 1, 2, and 3, respectively.

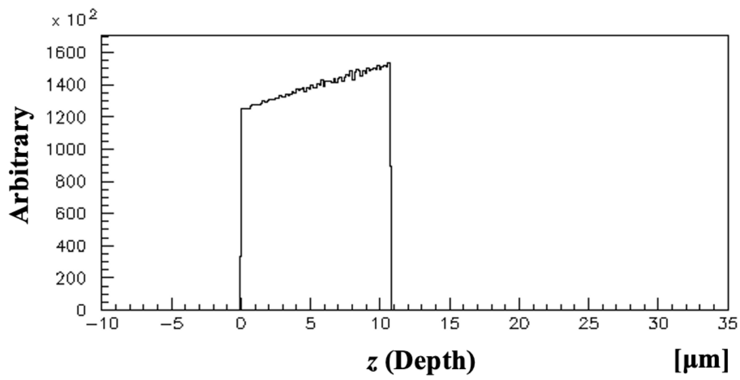

Fig. 6.20: The $^7\mathrm{Be}$ target distribution in the simulation region 1.

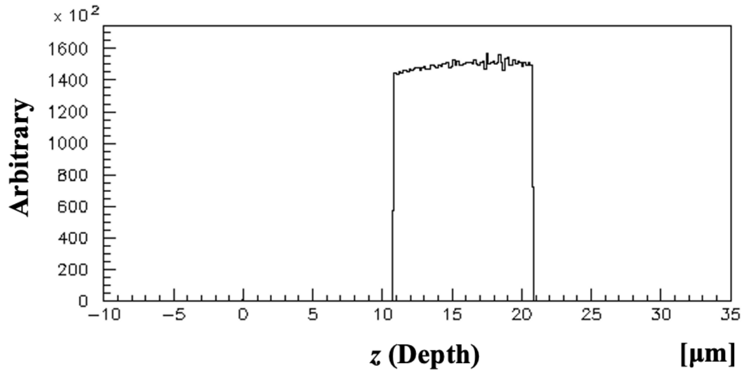

Fig. 6.21: The ^{7}Be target distribution in the simulation region 2.

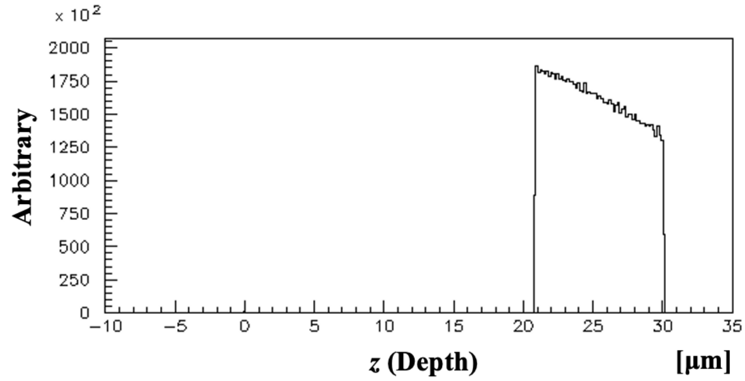

Fig. 6.22: The ^{7}Be target distribution in the simulation region 3.

Figs. 6.23 and 6.24 represent the simulation results for the dp_0 and dp_1 reactions, respectively. The simulation encompassed the experimental setup, incorporating details such as detector and target geometry, expected proton energies, distributions of ^{7}Be, proton energy resolutions, and proton energy straggling.

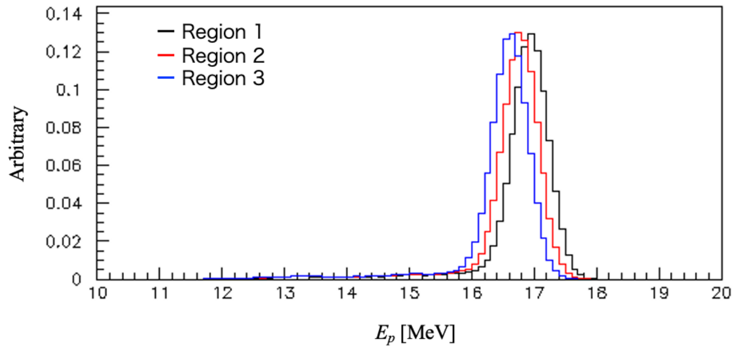

Fig. 6.23: The simulation result for the dp_0 reaction at the measurement of $E_d = 1.6$ MeV at 45° detector.

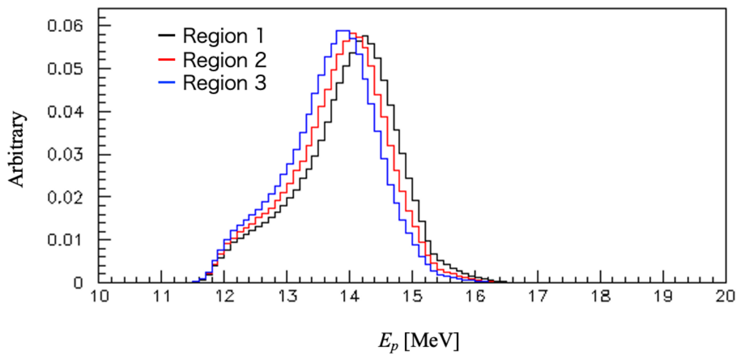

Fig. 6.24: The simulation result for the dp_1 reaction at the measurement of $E_d = 1.6$ MeV at 45° detector.

6.6 Fitting Results

The fitting results corresponding to the experimental setups $E_d = 1.6$ MeV at 45 degrees, $E_d = 1.6$ MeV at 30 degrees, $E_d = 0.6$ MeV at 45 degrees, and $E_d = 0.6$ MeV at 30 degrees are shown in Figs. 6.25, 6.26, 6.27, and 6.28, respectively.

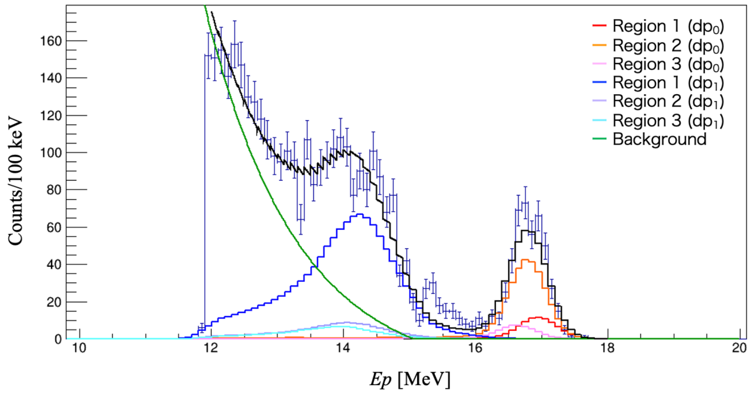

Fig. 6.25: Fitting result for the measurement of $E_d = 1.6$ MeV at 45° detector.

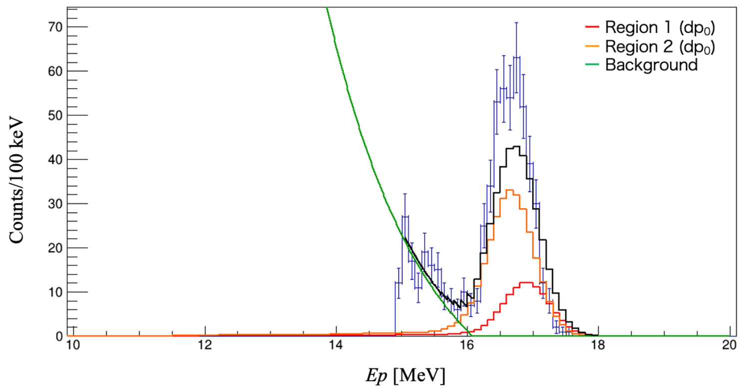

Fig. 6.26: Fitting result for the measurement of $E_d = 1.6$ MeV at 30° detector.

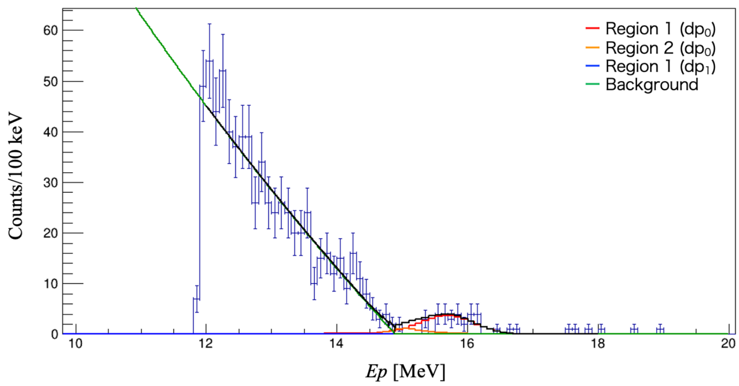

Fig. 6.27: Fitting result for the measurement of $E_d = 0.6$ MeV at 45° detector.

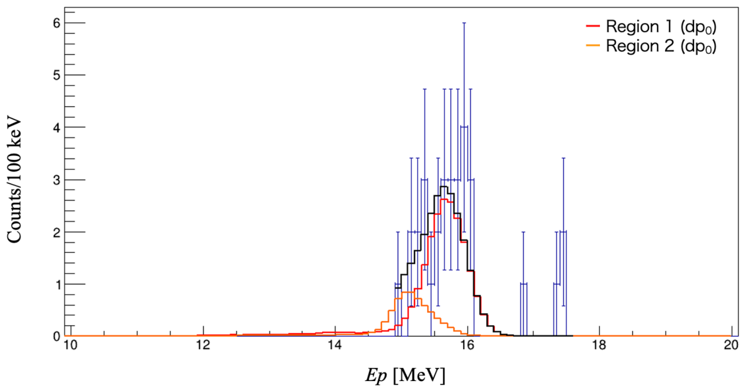

Fig. 6.28: Fitting result for the measurement of $E_d = 0.6\ \mathrm{MeV}$ at 30° detector.

Chapter 7

Systematic Errors

Systematic errors affecting the measured quantities necessary to obtain the cross sections were assessed.

7.1 Beam Current

The beam currents were read directly from the target and stopper. The electron knockout was prevented by suppressors. The function of the suppressor was confirmed by applying the various voltages to the suppressor.

7.1.1 Suppressor Voltages Optimization for the ΔE_d = 1.6 MeV Measurement

Collimator Suppressor Voltage

The voltage for the collimator suppressor was optimized. The voltage for the target was kept at -200 V. Fig. 7.1 shows the current value of the target by changing the suppressor voltage.

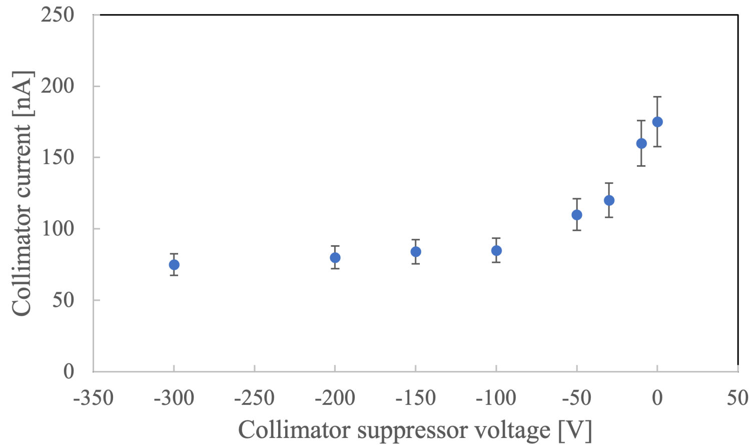

Fig. 7.1: The collimator current stabilized when the suppressor voltage exceeded -100 V.

Without applying the voltage to the collimator suppressor, the collimator current was relatively larger due to the electron escape effect. The collimator current decreased as bias was increased and stabilized when the suppressor voltage exceeded -100 V.

Figs. 7.2 and 7.3 show the target current and the stopper current with different applied voltages for the collimator suppressor.

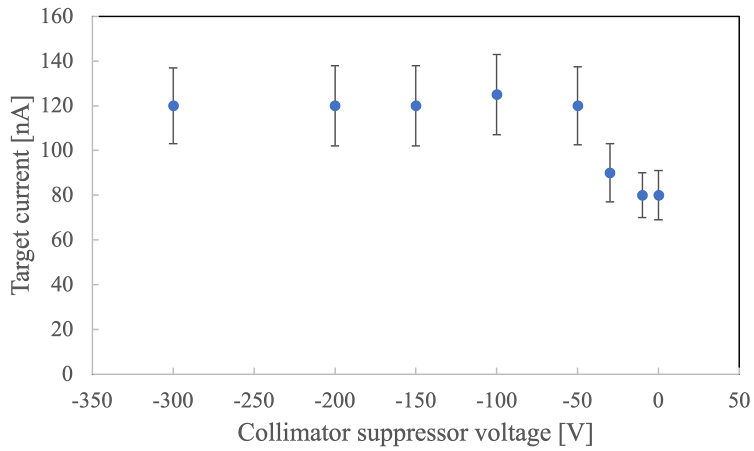

Fig. 7.2: The target current vs. the collimator suppressor voltage at ΔE_d = 1.6 MeV.

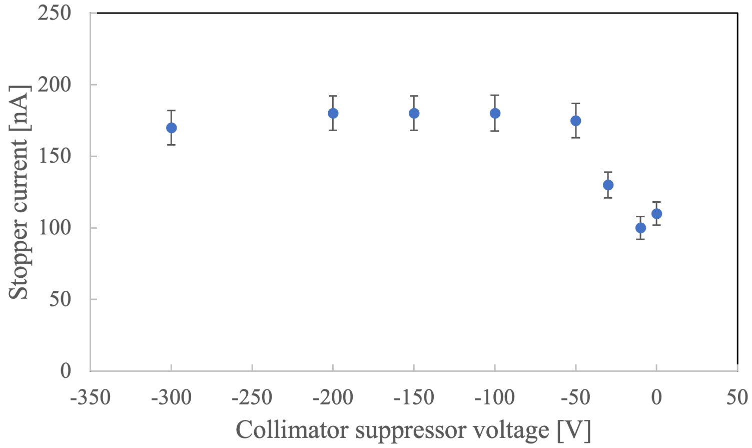

Fig. 7.3: The stopper current vs. the collimator suppressor voltage ΔE_d = 1.6 MeV.

When the collimator suppressor voltage was zero or low, both target and stopper currents exhibited higher readings. This resulted from escaping electrons originating from the collimator reaching the target and the stopper, where they were subsequently absorbed. The majority of the beam was collimated at the collimator. The collimator was most affected by the beam. The number of escaping electrons decreased as the collimator suppressor voltage was increased. A voltage of -200 V was determined as the appropriate value for the collimator suppressor.

Target Suppressor Voltage

The voltage for the collimator suppressor was maintained at -200 V, while the target suppressor voltage was varied. Fig. 7.4 shows the target current with different applied voltages for the target suppressor.

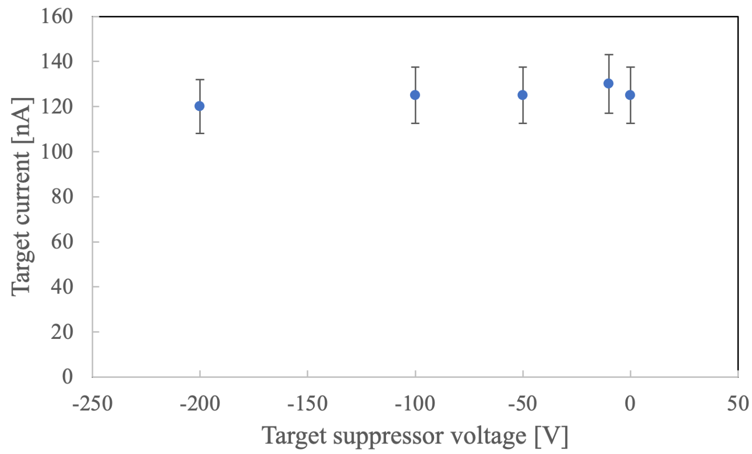

Fig. 7.4: The target current vs. the target suppressor voltage ΔE_d = 1.6 MeV.

The target current was almost unaffected by changes in the target suppressor voltage. This was attributed to the fact that the collimator bore the most significant impact from escaping electrons resulting from beam collisions, while the collisions on the target and the stopper had minimal effect. Figs. 7.5 and 7.6 depict the collimator and stopper currents.

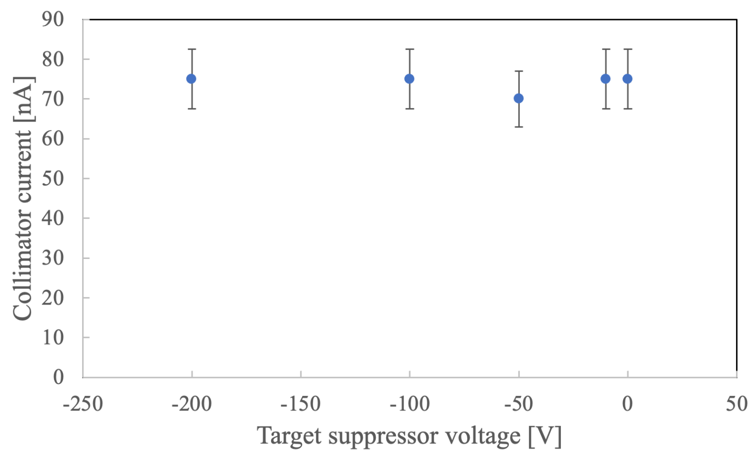

Fig. 7.5: The collimator current vs. the target suppressor voltage.

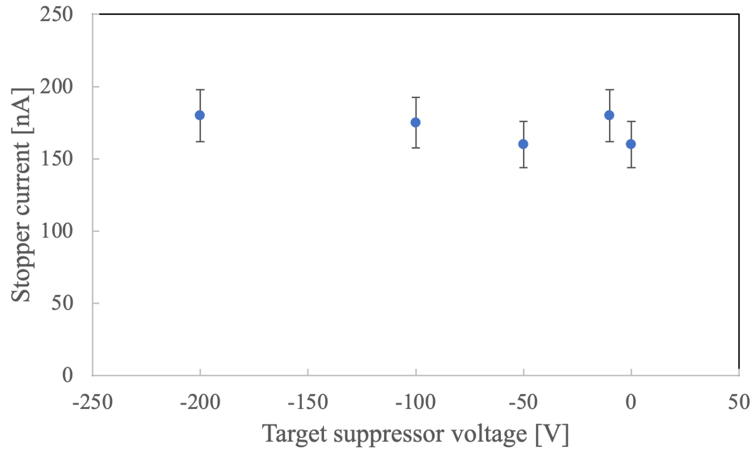

Fig. 7.6: The stopper current vs. the target suppressor voltage ΔE_d = 1.6 MeV.

The voltage was optimized at -200 V with varying applied voltages for the target suppressor. Both the collimator and stopper currents were not significantly influenced by changes in the target suppressor voltage. A voltage of -200 V was determined as the appropriate value for the target suppressor.

7.1.2 Suppressor Voltages Optimization for the ΔE_d = 0.6 MeV Measurement

The beam particles stopped inside the target at the ΔE_d = 0.6 MeV measurement. The current at the stopper was not expected. Optimization was performed only for the target suppressor. The collimator suppressor was maintained at -200 V while the target suppressor voltage was optimized.

Fig. 7.7 shows the target current with different applied voltages for the target suppressor.

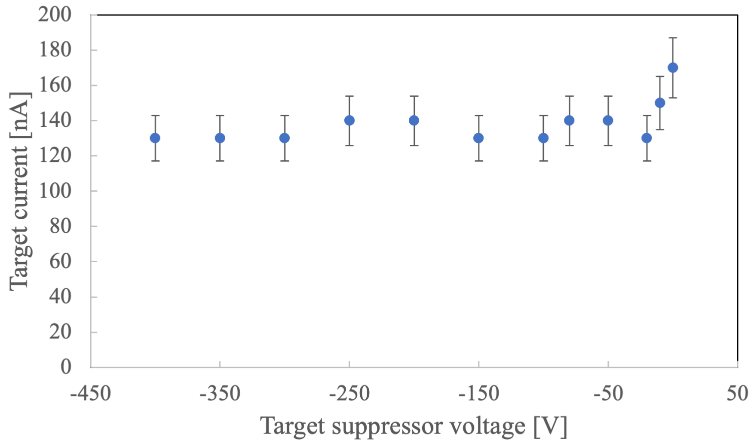

Fig. 7.7: The target current vs. the target suppressor voltage ΔE_d = 0.6 MeV.

The beam collided with the target, resulting in the escape of free electrons. Consequently, the current was recorded higher when the applied voltage to the target suppressor was insufficient. Fig. 7.8 shows the collimator current during the optimization of the target suppressor voltage. As depicted in Fig. 7.8, the collimator current was relatively lower when the target suppressor voltage was insufficiently applied. This phenomenon occurred because escaping electrons from the target were absorbed into the collimator when the target suppressor voltage was not adequately applied. However, the collimator current became stable when a higher negative voltage was applied to the target suppressor. The target suppressor voltage was set at -200 V to prevent electrons from escaping from the target.

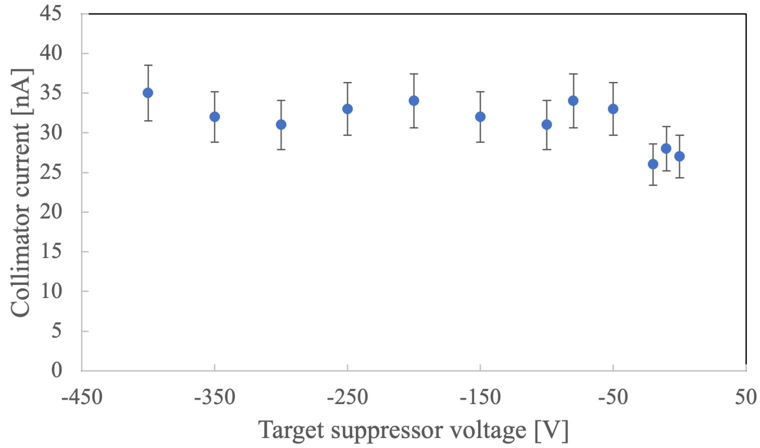

Fig. 7.8: The collimator current vs. the target suppressor voltage ΔE_d = 0.6 MeV.

7.1.3 Conclusion of the Suppressor and Systematic Error on the Beam Current

Both the collimator and target suppressors were optimized and set at -200 V. The electric fields were assumed to be sufficiently effective in pulling back escaping electrons. The systematic errors in reading the beam current were estimated at 10%, accounting for fluctuations in the current integrator reading values.

7.2 ^{7}Be Target Number

7.2.1 ^{7}Be Target Counts by the $\mathrm{LaBr_3}$ Detector

The statistical error and systematic error were estimated as 0.69% and 4.3%, respectively. These estimations were conducted through the ^{137}Cs and ^{60}Co checking source calibration. The details are in 4.1.

7.2.2 ^{7}Be Target Areal Distribution

The ^{7}Be target production area, denoted as S_p, was designed with a 1.0 mm radius. Concurrently, the deuteron beam was collimated into a $1.5-$ mm radius, and the area was denoted as S_d. All produced targets were employed in the reaction, and the deuteron beam irradiated in the reaction with an area ratio denoted as S_p/S_d to the target.

After the experiment, the $^7\mathrm{Be}$ target distribution was measured using lead slits and the $\mathrm{LaBr_3}$ detector. Fig. 7.9 shows the schematic side view of the $^7\mathrm{Be}$ target distribution measurements. The $\mathrm{LaBr_3}$ detector was securely fixed on the stable table, while the $^7\mathrm{Be}$ target was positioned on the XY-movable stage beneath the $\mathrm{LaBr_3}$ detector. Lead slits with a 1 mm gap were positioned on the $^7\mathrm{Be}$ target to collimate the gamma rays. The $^7\mathrm{Be}$ target was then horizontally moved from right to left to scan the gamma ray counts originating from the target.

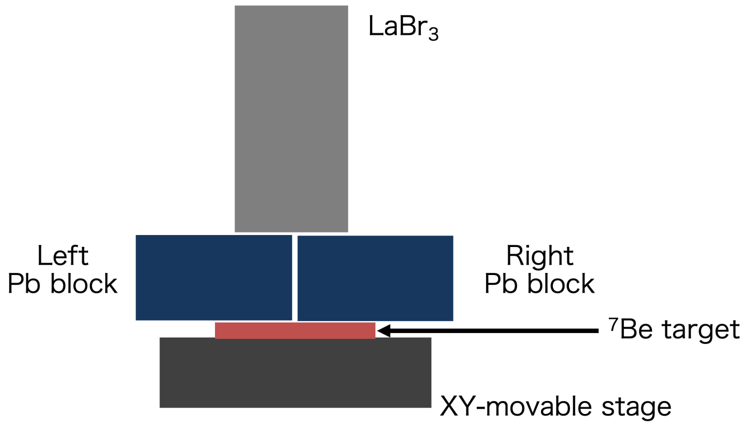

Fig. 7.9: The schematic sideview of the gamma-ray measurement to determine the $^7\mathrm{Be}$ target distribution.

Fig. 7.10 displays the measured counts obtained by moving the lead (Pb) slits, along with the fitted results. The X-axis represents the distance from the left slit's edge to the target center, and the Y-axis is gamma-ray counts per 1-mm slit.

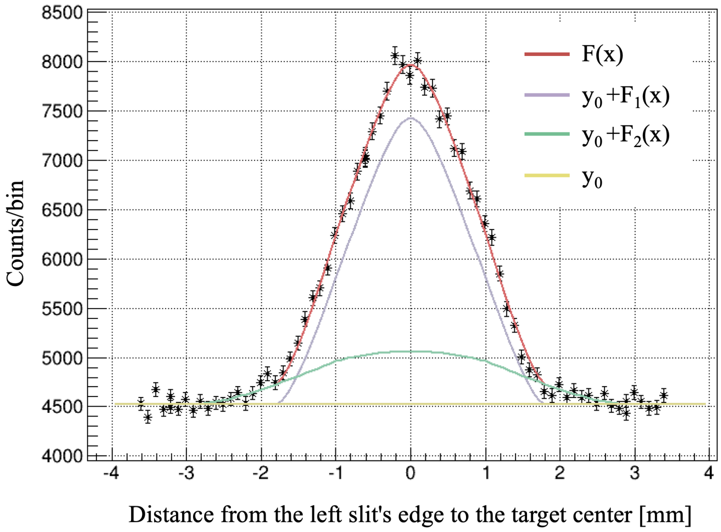

Fig. 7.10: The measured counts obtained by moving the lead (Pb) slits and fitted functions.

Eq. (7.1) presents the fitting function, where the ^{7}Be distribution was modeled to include two peaks.

$$
\begin{aligned}
F(x) &= y_0 + F_1(x) + F_2(x) \\
&= y_0 + A_1 \times 2 \times \int \sqrt{R_1^2 - (x - x_0)^2} dx + A_2 \times 2 \times \int \sqrt{R_2^2 - (x - x_0)^2} dx
\end{aligned}
\tag{7.1}
$$

Here, R_1 and R_2 represent the anticipated diameters of the ^{7}Be target. A_1 and A_2 denote the amplitudes of the two components, while y_0 corresponds to the baseline of the function. x_0 represents the offset of the target center.

Table 7.1 provides information on the fitting parameters, their associated physical quantities, and the corresponding fitted values.

Table 7.1: Fitting results to determine the target distribution.

Parameters	Physical quantities	Values
R_1	Radius of the $^7\mathrm{Be}$ target distribution 1	0.870
R_2	Radius of the $^7\mathrm{Be}$ target distribution 2	1.952
A_1	Amplitude of the the $^7\mathrm{Be}$ target distribution 1	1218.2
A_2	Amplitude of the the $^7\mathrm{Be}$ target distribution 2	77.5
y_0	Function base line	4522.8

The number of gamma rays at each measurement point was determined by extracting the spectrum obtained by subtracting the background from the gamma-ray measurement. However, the background was measured only once for all measurements. The gamma-ray measurement values were compared to a single background data set. Thus, the errors on the counted gamma ray were expected to be significantly large. However, the errors associated with background subtraction have not been thoroughly estimated. Despite this, the approximate value used to estimate the radius of the $^7\mathrm{Be}$ target distribution remained meaningful for calculating the final target number.

Following the fitting results, the measured $^7\mathrm{Be}$ distributions, the anticipated $^7\mathrm{Be}$ target distribution, and the deuteron beam distribution are illustrated in Fig. 7.11. The expected radius of the $^7\mathrm{Be}$ target was set at $1.0\,\mathrm{mm}$, given that a $1.0\,\mathrm{mm}$ collimator was positioned in front of the target to define the target area. However, two distributions were measured with two different radii. Two reasons were considered to explain this observed distribution.

1. $^6\mathrm{Li}(d,n)^7\mathrm{Be}$ reaction produced $^7\mathrm{Be}$ target during the $^7\mathrm{Be}(d,p)^8\mathrm{Be}$ reaction measurement.

2. The $^7\mathrm{Be}$ target diffusion during the experiment or/and after the experiment.

Possibility 1. was dismissed because the $^7\mathrm{Li}(p,n)^7\mathrm{Be}$ reaction, which was the $^7\mathrm{Be}$ target production process, produced 190 times more $^7\mathrm{Be}$ target nuclei than the $^6\mathrm{Li}(d,n)^7\mathrm{Be}$ reaction during the $^7\mathrm{Be}(d,p)^7\mathrm{Be}$ reaction measurement. The $^7\mathrm{Be}$ target numbers produced by the $^7\mathrm{Li}(p,n)^7\mathrm{Be}$ and the $^6\mathrm{Li}(d,n)^7\mathrm{Be}$ reactions were compared considering the $^7\mathrm{Li}(p,n)^7\mathrm{Be}$ and the $^6\mathrm{Li}(d,n)^7\mathrm{Be}$ reaction cross sections, the number of

^{7}Li and ^{6}Li nuclei, and the irradiation time of the beam current. Therefore, the amount of ^{7}Be generated by the ^{6}Li$(d,n)^7$Be reaction was deemed negligible.

Possibility 2. was attributed to ^{7}Be diffusion. However, determining whether the diffusion occurred during or after the experiment was challenging, as the distribution measurement was conducted approximately six months later. Here, diffusion was considered to have occurred during the experiment, and the maximum systematic error attributable to diffusion was anticipated.

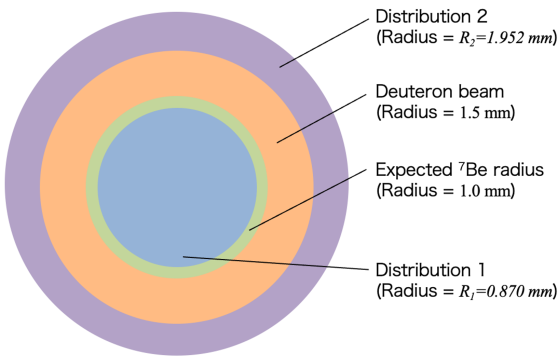

Fig. 7.11: A schematic picture of measured and expected ^{7}Be target distribution, and the deuteron beam area.

In the calculation to obtain the ^{7}Be$(d,p)^8$Be cross section, all of the produced ^{7}Be target was used. However, if diffusion ^{7}Be targets exceeded the expected ^{7}Be target area (> 1.0 mm), the diffused ^{7}Be targets were not used for the reaction. Based on the fitted results, the ratio of the area outside $r = 1.0$ mm was 22%, representing the portion of the total ^{7}Be target excluded from the cross-section calculation.

In the case where diffusion was considered, the ^{7}Be target number was expected to be 22% smaller, consequently leading to an anticipated 22% increase in the ^{7}Be$(d,p)^8$Be cross section.

7.3 Detector Geometry and Solid Angle

The accuracy of the detector installation position was expected to be influenced by the machining accuracy, which was ±1.0 mm. The detector installation location was assumed to deviate by ± 1.0 mm from the designed position relative to the target center. The solid angle Ω was then calculated using Eq. (7.2), as detailed below.

$$\Omega = \frac{\pi r^2}{l^2}. \tag{7.2}$$

Here, r represents the radius of the detector, and l denotes the distance from the target to the center of the detector. When l deviated by ± 1.0 mm, the solid angle Ω experienced a deviation of ± 0.0012 steradians. Consequently, the deviation in the solid angle represents a systematic uncertainty of $\pm 2.2\%$ in the reaction yield.

7.4 Systematic Errors Summary

The systematic errors are summarized in Table 7.2.

Table 7.2: The summary of the systematic errors.

Factor	Error [%]
Beam current reading	± 10
$LaBr_3$ gamma-ray counting to determine the ^7Be target number	± 4.3
The ^7Be target diffusion and deuteron beam number correction	$+22$
Detector geometry	± 2.2

Chapter 8

Results and Discussions

8.1 Astrophysical S-factors and Cross sections

As indicated in 6, simulations were performed for each experimental setup, and fitting functions were calculated. The E_p spectra from the experimental data were then fitted using these calculated functions, with the fitting parameters corresponding to the astrophysical S-factors. The astrophysical S-factors vs. center-of-mass energies are shown in Fig. 8.1. The orange-filled circles represent the astrophysical S-factors of the $^7\mathrm{Be}(d,p)^8\mathrm{Be}^{g.s.}$ reaction (dp_0) at the 45-degree detectors. The blue triangles correspond to the astrophysical S-factors of the $^7\mathrm{Be}(d,p)^8\mathrm{Be}^{1st}$ reaction (dp_1) at the 45-degree detectors. The green plus signs represent the combined astrophysical S-factors of dp_0+dp_1 at the 45-degree detectors. The orange-ringed circles correspond to the astrophysical S-factors of the $^7\mathrm{Be}(d,p)^8\mathrm{Be}^{g.s.}$ reaction (dp_0) measured at the 30-degree detectors. The plots around $E_{c.m.}$ = 0.2 MeV correspond to the measurement at E_d = 0.6 MeV. The red-filled circles represent the astrophysical S-factors of the $^7\mathrm{Be}(d,p)^8\mathrm{Be}^{g.s.}$ reaction (dp_0) at the 45-degree detectors. The red-ringed circles correspond to the astrophysical S-factors of the $^7\mathrm{Be}(d,p)^8\mathrm{Be}^{g.s.}$ reaction (dp_0) measured at the 30-degree detectors.

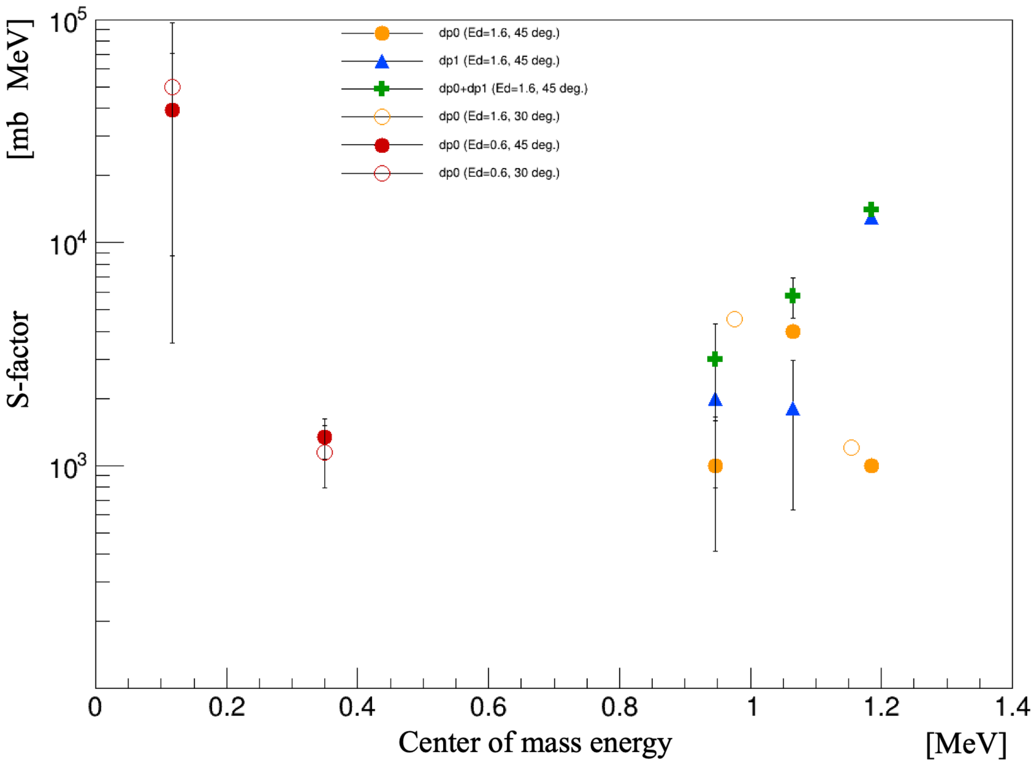

Fig. 8.1: The astrophysical S-factors vs. center-of-mass energies.

Cross sections were obtained using Eq. 6.18 based on astrophysical S-factors. The cross sections were initially calculated as single values at each incident deuteron energy. The resulting cross sections vs. center-of-mass energies are presented in Fig. 8.2.

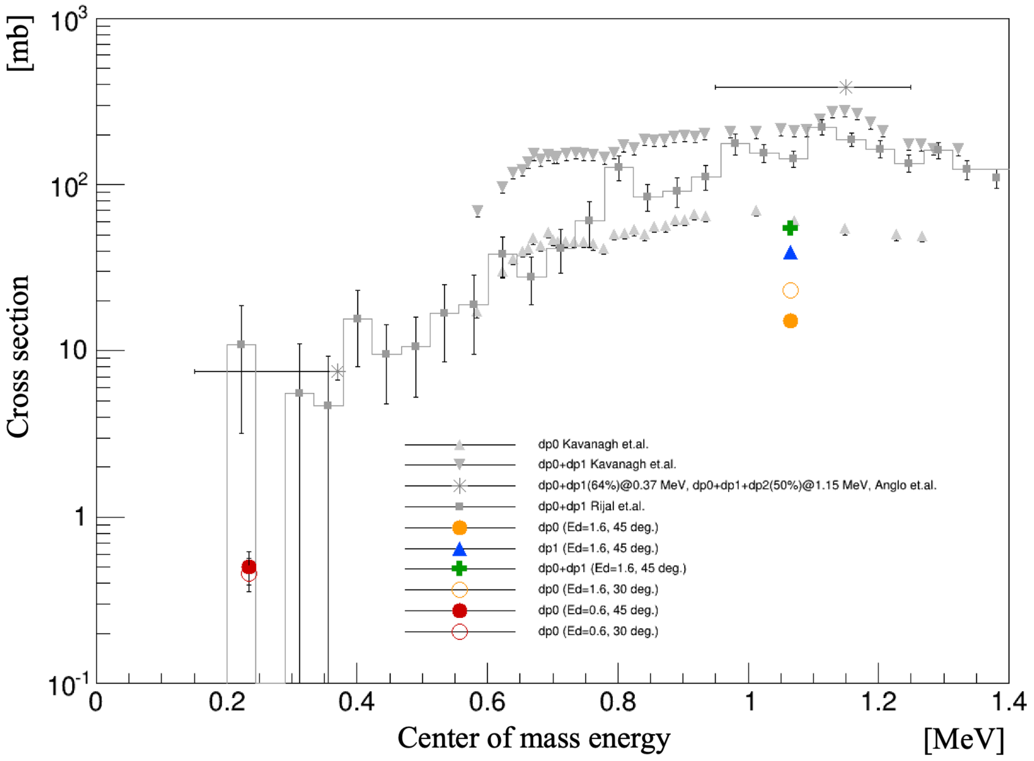

Fig. 8.2: The cross sections vs. center of mass energies. Only statistical errors are shown.

The results of this experiment are shown in colors. The plots around $E_{c.m.}$ = 1.1 MeV correspond to the measurement at E_d = 1.6 MeV. In particular, the orange-filled circle represents the cross section of the ${}^7\mathrm{Be}(d,p){}^8\mathrm{Be}^{g.s.}$ reaction (dp_0) at the 45-degree detectors. The blue triangle corresponds to the cross section of the ${}^7\mathrm{Be}(d,p){}^8\mathrm{Be}^{1st}$ reaction (dp_1) at the 45-degree detectors. The green plus sign represents the combined cross section of $dp_0 + dp_1$ at the 45-degree detectors. The orange-ringed circle corresponds to the cross section of the ${}^7\mathrm{Be}(d,p){}^8\mathrm{Be}^{g.s.}$ reaction (dp_0) measured at the 30-degree detectors. The plots around $E_{c.m.}$ = 0.2 MeV correspond to the measurement at E_d = 0.6 MeV. The red-filled circle represents the cross section of the ${}^7\mathrm{Be}(d,p){}^8\mathrm{Be}^{g.s.}$ reaction (dp_0) at the 45-degree detectors. The red-ringed circle corresponds to the cross section of the ${}^7\mathrm{Be}(d,p){}^8\mathrm{Be}^{g.s.}$ reaction (dp_0) measured at the 30-degree detectors.

The analysis for the thick target method was employed to divide the data. The astrophysical S-factor was supposed to be a constant within each divided incident deuteron energy region ΔE_d corresponding to the depth segments of the ${}^7\mathrm{Be}$ target. The results, presenting cross sections vs. center-of-mass energy for this experiment, are presented in Fig. 8.3.

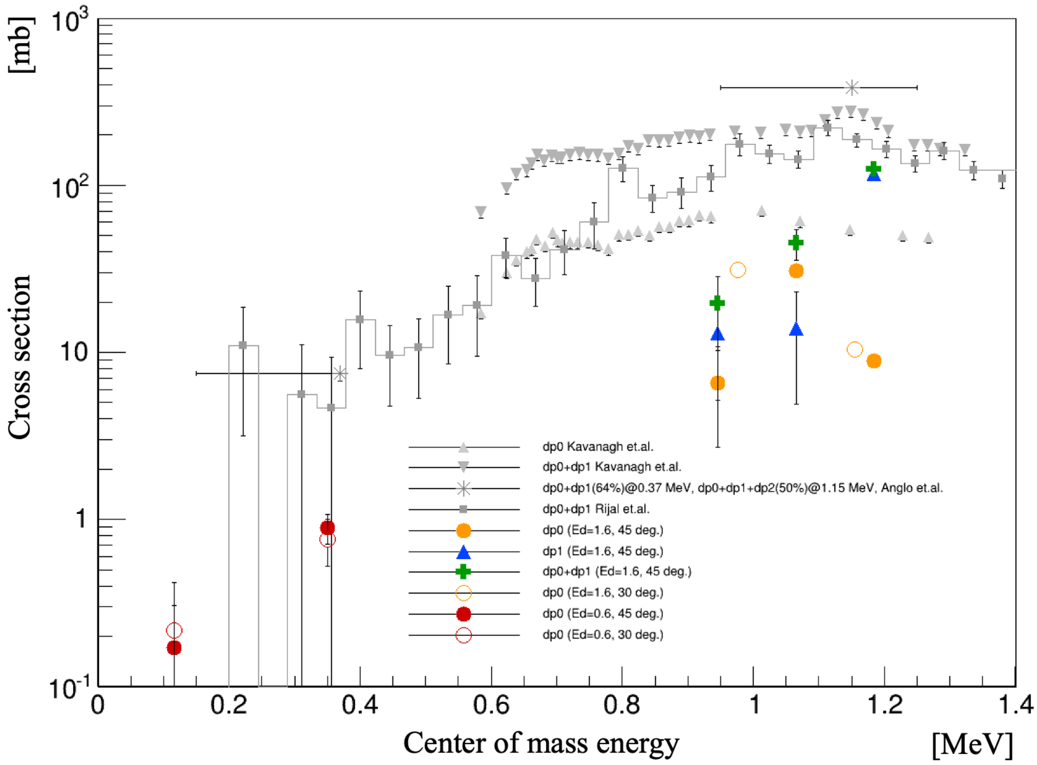

Fig. 8.3: The cross sections were calculated separately, assuming the astrophysical S-factors are constant at each incident deuteron energy bin (ΔE_d). Only statistical errors are shown. For systematic errors, refer to Table 7.2.

The data presented by Anglo *et al.* [3] and Rijal *et al.* [4] in the energy region of Big Bang nucleosynthesis included contributions from both dp_0 and dp_1. In contrast, our results in the same energy region exclusively represent the pure cross sections of dp_0. Therefore, the absolute cross section values were not comparable with the reference results. For the discussion of its impact on the CLP regarding the reaction cross sections of the dp reaction in the Big Bang nucleosynthesis's energy region, it is irrelevant which state of $^8\mathrm{Be}$ was selected after the $^7\mathrm{Be}(d,p)$ reaction occurred. Any channels were acceptable for the destruction of $^7\mathrm{Be}$ nuclei. Our results contributed specifically to the understanding of dp_0. Additionally, our cross section was obtained at the lowest energy of $E_{c.m.} = 0.12$ MeV with the highest sensitivity when compared to the available data [2, 3, 4].

8.2 Astrophysical Impact and Future Prospect

The abundances of light nuclei are typically expressed as ratios to the abundance of hydrogen (H). The study by Rijal *et al.* [4] examined the ^{7}Li abundance ratio to H (^{7}Li/H), both with and without the $d + {}^7\mathrm{Be}$ reaction. The reported results indicated that $^7\mathrm{Li/H}$ = 5.05 − 5.08 $\times 10^{-10}$ without the $d + {}^7\mathrm{Be}$ reaction, while with the $d + {}^7\mathrm{Be}$ reaction, it was $^7\mathrm{Li/H}$ = 4.24 − 4.61 $\times 10^{-10}$. The $d + {}^7\mathrm{Be}$ reaction reduced the abundance ratio of $^7\mathrm{Li/H}$ by approximately 14% compared to the scenario without the reaction. In their study, the $d + {}^7\mathrm{Be}$ reaction encompassed both $^7\mathrm{Be}(d, p)$ and $^7\mathrm{Be}(d, \alpha)$ reactions. [39] recalculated the impact of the reduction in Li abundance using the reaction rate from [4]'s measurement of the $d + {}^7\mathrm{Be}$ reaction. They revised the final $^7\mathrm{Li/H}$ reduction to 0.7%.

Our results regarding the $^7\mathrm{Be}(d, p)^8\mathrm{Be}$ reaction cross sections at the Big Bang nucleosynthesis energy region were nearly a factor of 10 smaller than those reported cross sections of the $d + {}^7\mathrm{Be}$ reaction by [4]. [4]'s cross section results of the $^7\mathrm{Be}(d, p)^8\mathrm{Be}$ reaction accounted for $dp_0 + dp_1$, whereas ours specifically represented the pure dp_0. Upon comparison, our obtained $^7\mathrm{Be}(d, p)$ cross sections were relatively lower. Thus, its impact on the CLP was determined to be minor. In conclusion, the $^7\mathrm{Be}(d, p_0)$ reaction was not a solution to the CLP.

Chapter 9

Summary

We conducted measurements of the $^7\mathrm{Be}(d,p)^8\mathrm{Be}$ reaction in the Big Bang nucleosynthesis energy region ($E_{c.m.} = 0.1 - 0.4$ keV) to determine its cross sections in efforts to address the Cosmological Lithium Problem (CLP). A notable challenge in this experiment was the production of the radioactive $^7\mathrm{Be}$ target. Following the completion of the development, we successfully generated 2.80×10^{13} $^7\mathrm{Be}$ nuclei using the activation method. The outgoing proton energy and yield from the $^7\mathrm{Be}(d,p)^8\mathrm{Be}$ reactions were measured with the produced $^7\mathrm{Be}$ target at $E_d = 1.6$ and 0.6 MeV.

The analysis involved performing simulations to derive the fitting function for the outgoing proton energy spectra. The cross sections were not directly calculated from the yield due to the thick target method. Consequently, the $^7\mathrm{Be}(d,p)^8\mathrm{Be}$ cross sections were obtained by fittings. However, it was found to produce a limiting impact on the CLP compared to [2, 3, 4], though the $^7\mathrm{Be}(d,p)^8\mathrm{Be}$ reaction may not be the solution to the CLP based on those reference studies, including my result.

On the other hand, we conducted a novel measurement employing a radioactive $^7\mathrm{Be}$ target, achieving precision within the energy range of Big Bang nucleosynthesis. The cross section was obtained at the lowest energy of $E_{c.m.} = 0.12$ MeV with the highest sensitivity compared to the available data [2, 3, 4]. Despite these advancements, the CLP remains a mysterious and fascinating problem in primordial nucleosynthesis. Addressing the CLP requires consideration from various perspectives, particularly through astrophysical observations.

In future experiments, it is beneficial to measure the cross section from reactions corresponding to the higher excited states of $^{8}\mathrm{Be}$, such as the $^{7}\mathrm{Be}(d,p)^{8}\mathrm{Be}^{2nd}$ reaction. Due to the high Q-value, the $^{7}\mathrm{Be}(d,p)^{8}\mathrm{Be}^{2nd}$ reaction could also occur in the Big Bang energy region. Our experiment was explicitly designed to measure only those two reactions, the $^{7}\mathrm{Be}(d,p)^{8}\mathrm{Be}^{g.s.}$ and the $^{7}\mathrm{Be}(d,p)^{8}\mathrm{Be}^{1st}$. Therefore, lower proton energies corresponding to the higher excited states of $^{8}\mathrm{Be}$ could not be captured. If we perform the following experiment, it is excellent to measure lower proton energies to explore the cross section associated with the higher excited state of $^{8}\mathrm{Be}$. Consequently, an update to the detector design and system will be necessary.

Acknowledgement

Firstly, I would like to express my gratitude to Prof. A. Tamii for his supervision and for introducing me to this fascinating research subject. My sincere thanks also go to Prof. N. Kobayashi. I might not have achieved especially the analysis part without his support. I would like to express my profound thanks to Prof. H. Yamaguchi and Dr. S. Hayakawa, who consistently provided strong support throughout our projects. I would like to show my gratitude to Dr. H. Makii and Dr. M. Asai, who offered significant support, especially in the developmental phase of our projects. I am obliged to everyone who supported both me and our beam time at CNS at the University of Tokyo and the Tandem Accelerator at JAEA.

I would like to convey my thanks to all the excellent collaborators who participated in the experiments at Kobe University, especially Prof. T. Shima, Prof. Y. Maeda, Dr. D. T. Tran, Dr. L. Yang, Dr. Z. Yang, Mr. H. Shimizu, Mr. X. Wang, Prof. A. Taniike, Mr. T. Yokose, Ms. C. Komiyama, and Dr. Y. Mori.

I greatly thank Prof. S. Ota for the valuable discussions. I express my great gratitude to Prof. H. Sakaguchi, who has provided constant encouragement during my research since my master's studies. I am grateful to Prof. T. Nakano, who has kept an eye on my progress and supported me.

I am also thankful to Prof. P. von Neumann-Cosel, Dr. D. Kahl, Dr. K. C. W. Li, and Dr. T. Chillery for their meaningful discussions and warm support.

Thanks to all the individuals who have been part of and supported me throughout my research journey.

Finally, my gratitude would be incomplete without acknowledging my parents. Their unwavering trust and significant support have been my constant pillars. Thank you.

Appendix A

Detailed Electronics Circuit

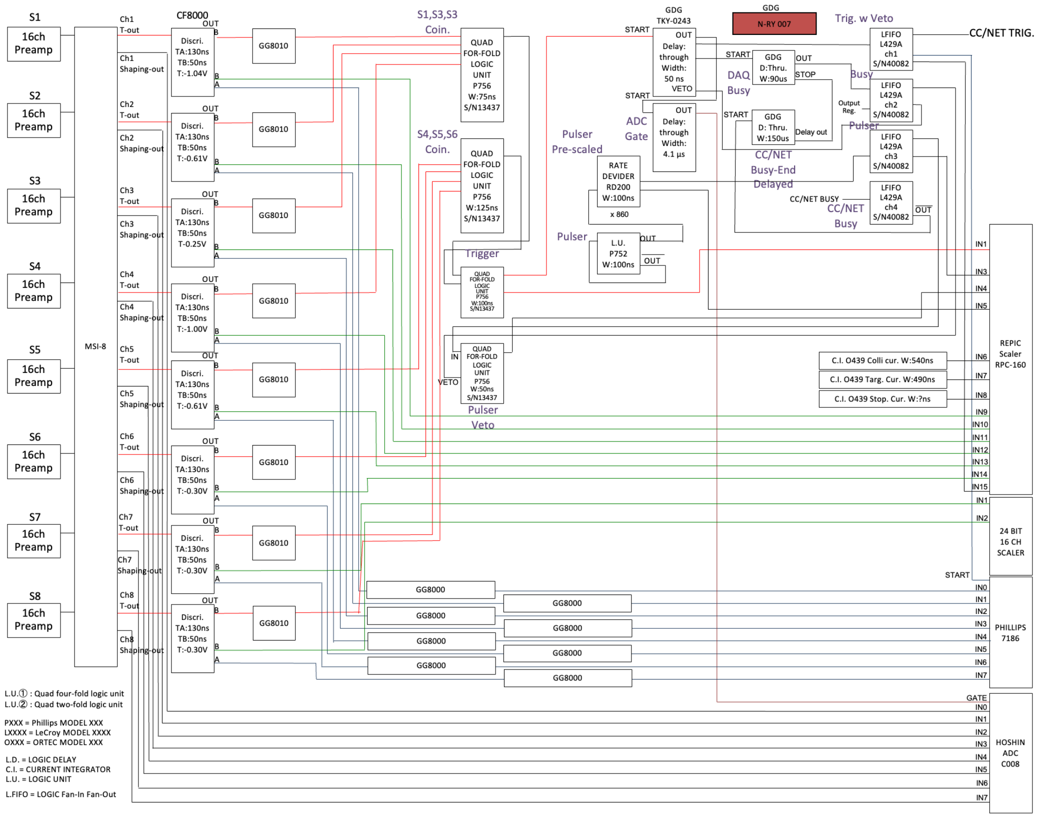

Fig. A.1: Electronics details.

Appendix B

Accidental Coincidence Background Subtraction Method for the Four Layered Silicon Detector

To select the proton events from the $^7\mathrm{Be}(d,p)^8\mathrm{Be}$ reaction, the detector time difference was applied as a gate (refer to 5.2 for the details). The time differences between the detectors were determined by using the first layer as a time reference, and calculating the time differences between the second, third, and fourth layers. Eqs. B.1, B.2, and B.3 represent time differences.

$$T2' = T2 - T1. \tag{B.1}$$

$$T3' = T3 - T1. \tag{B.2}$$

$$T4' = T4 - T1. \tag{B.3}$$

Each time difference has a structure as shown in Fig. B.1.

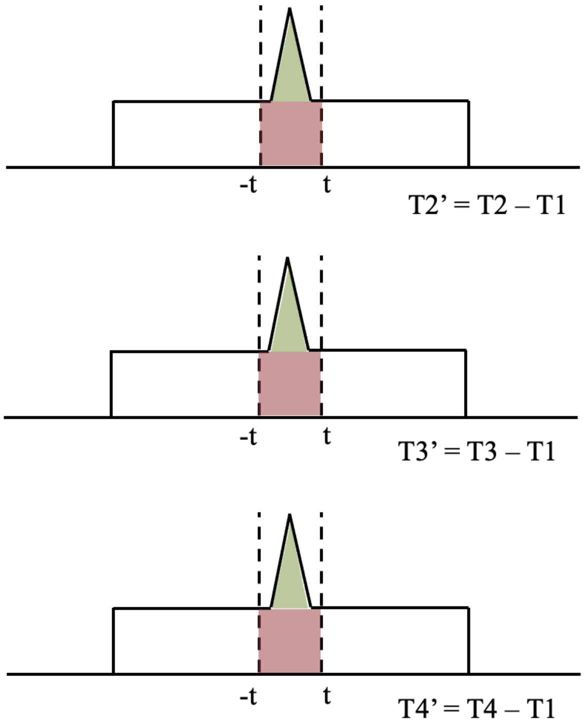

Fig. B.1: The timing differences.

The true events were within the green peak centered at time difference 0 at the three time differences in Fig. B.1. The gates were set from time $-t$ to t in Fig. B.1. However, when these time differences were applied as gates, accidental coincidence events, represented by red squares, in Fig. B.1 were selected simultaneously as the background. To estimate the number of accidental coincidence events, we performed the background subtraction of accidental coincidence events.

All the phenomena, including the true signal and background signal (= accidental coincidence events), were expected in five types of cases, as one to four of the four detectors had a signal, and those were assumed to be the following five types of A to E.

A: All four detectors have random signals and different timings.

B: Two of the four detectors had the same signal; the other two had random signals.

C: Two of the four detectors have the same signal; the other two have another signal.

D: Three of the four detectors have the same signal; another detector had an accidental coincidence.

E: All four detectors have the same signal at the same time.

Table B.1 shows the event types. For convenience, symbol names starting with M were given for, specifically, how many layers of detectors have signals. Brackets () indicate that the timing is simultaneous in detectors. (eg. (T1, T2) represents that the first and second layer detectors had a simultaneous signal.)

Table B.1: Types of events.

A	T1, T2, T3, T4	M_o
B	(T1, T2), T3, T4	$M_{(12)}$
	T1, (T2, T3), T4	$M_{(23)}$
	T1, T2, (T3, T4)	$M_{(34)}$
	(T1, T3), T2, T4	$M_{(13)}$
	(T1, T4), T2, T3	$M_{(14)}$
	(T2, T4), T1, T3	$M_{(24)}$
C	(T1, T2), (T3, T4)	$M_{(12)(34)}$
	(T1, T3), (T2, T4)	$M_{(13)(24)}$
	(T1, T4), (T2, T3)	$M_{(14)(23)}$
D	(T1, T2, T3), T4	$M_{(123)}$
	T1, (T2, T3, T4)	$M_{(234)}$
	(T1, T3, T4), T2	$M_{(134)}$
	(T1, T2, T4), T3	$M_{(124)}$
E	(T1, T2, T3, T4)	$M_{(1234)}$

To visualize the timing structure, a cube in Fig. B.2 was prepared.

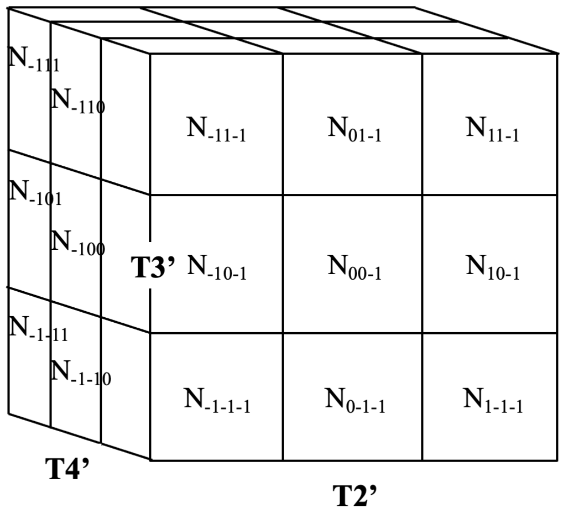

Fig. B.2: The cube for visualizing the structure of the timing differences.

The cube has three axes, and those axes represent three variables for timing differences (T2', T3', and T4'). The three vertical (horizontal) sections on one side of the cube indicate the following three timing differences: an area where the timing difference between $-$ t and t was 0, and areas on the left and right sides show completely random signal regions. To add one more explanation, it helps to imagine a three-dimensional version of the three-timing axes in Fig. B.1. The symbol names starting with N were given for gate types. The three numbers in the argument of N indicate the position of the timing difference in Fig. B.1, and T2 ', T3 ', and T4 ', respectively, with the left random event being represented as -1, the peak as 0, and the right random event as 1.

The correspondence between M and gate type N is shown in Fig. B.3 below. Those M and N notations indicate which kind of accidental coincidence event corresponds to which timing differences of the four detectors, T2', T3', and T4'.

M_o : N_{-1-1-1}, N_{0-1-1}, N_{1-1-1}, N_{-1-10}, N_{0-10}, N_{1-10}, N_{-1-11}, N_{0-11}, N_{1-11},
N_{-10-1}, N_{00-1}, N_{10-1}, N_{-100}, N_{000}, N_{100}, N_{-101}, N_{001}, N_{101},
N_{-11-1}, N_{01-1}, N_{11-1}, N_{-110}, N_{010}, N_{110}, N_{-111}, N_{011}, N_{111},

$M_{(12)}$: N_{0-1-1}, N_{0-10}, N_{0-11}, N_{00-1}, N_{000}, N_{001}, N_{01-1}, N_{010}, N_{011}
$M_{(23)}$: N_{-1-1-1}, N_{-1-10}, N_{-1-11}, N_{00-1}, N_{000}, N_{001}, N_{11-1}, N_{110}, N_{111}
$M_{(34)}$: N_{-1-1-1}, N_{0-1-1}, N_{1-1-1}, N_{-100}, N_{000}, N_{100}, N_{-111}, N_{011}, N_{111}
$M_{(13)}$: N_{-10-1}, N_{00-1}, N_{10-1}, N_{-100}, N_{000}, N_{100}, N_{-101}, N_{001}, N_{101}
$M_{(14)}$: N_{-1-10}, N_{0-10}, N_{1-10}, N_{-100}, N_{000}, N_{100}, N_{-110}, N_{010}, N_{110}
$M_{(24)}$: N_{-1-1-1}, N_{0-10}, N_{1-11}, N_{-10-1}, N_{000}, N_{101}, N_{-11-1}, N_{010}, N_{111}

$M_{(12)(34)}$: N_{0-1-1}, N_{000}, N_{011}
$M_{(13)(24)}$: N_{-10-1}, N_{000}, N_{101}
$M_{(14)(23)}$: N_{-1-10}, N_{000}, N_{110}

$M_{(123)}$: N_{00-1}, N_{000}, N_{001}
$M_{(234)}$: N_{-1-1-1}, N_{000}, N_{111}
$M_{(134)}$: N_{-100}, N_{000}, N_{100}
$M_{(124)}$: N_{0-10}, N_{000}, N_{010}

$M_{(1234)}$: N_{000}

Fig. B.3: The correspondence between M and gate type N.

Gate types represented N describes the accidental coincidence event timing M as shown following Eqs. (B.4) to (B.30).

$$N_{-1-1-1} = M_o + M_{(23)} + M_{(34)} + M_{(24)} + M_{(234)}. \tag{B.4}$$

$$N_{0-1-1} = M_o + M_{(12)} + M_{(34)} + M_{(12)(34)}. \tag{B.5}$$

$$N_{1-1-1} = M_o + M_{(34)}. \tag{B.6}$$

$$N_{-1-10} = M_o + M_{(23)} + M_{(14)} + M_{(14)(23)}. \tag{B.7}$$

$$N_{0-10} = M_o + M_{(12)} + M_{(14)} + M_{(24)} + M_{(124)}. \tag{B.8}$$

$$N_{1-10} = M_o + M_{(14)}. \tag{B.9}$$

$$N_{-1-11} = M_o + M_{(23)}. \tag{B.10}$$

$$N_{0-11} = M_o + M_{(12)}. \tag{B.11}$$

$$N_{1-11} = M_o + M_{(24)}. \tag{B.12}$$

$$N_{-10-1} = M_o + M_{(13)} + M_{(24)} + M_{(13)(24)}. \tag{B.13}$$

$$N_{00-1} = M_o + M_{(12)} + M_{(23)} + M_{(13)} + M_{(123)}. \tag{B.14}$$

$$N_{10-1} = M_o + M_{(13)}. \tag{B.15}$$

$$N_{-100} = M_o + M_{(34)} + M_{(13)} + M_{(14)} + M_{(134)}. \tag{B.16}$$

$$\begin{aligned} N_{000} = M_o + M_{(12)} + M_{(23)} + M_{(34)} + M_{(13)} + M_{(14)} \\ +M_{(24)} + M_{(12)(34)} + M_{(13)(24)} + M_{(14)(23)} \\ +M_{(123)} + M_{(234)} + M_{(134)} + M_{(124)} + M_{(1234)}. \end{aligned} \tag{B.17}$$

$$N_{100} = M_o + M_{(34)} + M_{(13)} + M_{(14)} + M_{(134)}. \tag{B.18}$$

$$N_{-101} = M_o + M_{(13)}. \tag{B.19}$$

$$N_{001} = M_o + M_{(12)} + M_{(23)} + M_{(13)} + M_{(123)}. \tag{B.20}$$

$$N_{101} = M_o + M_{(13)} + M_{(24)} + M_{(13)(24)}. \tag{B.21}$$

$$N_{-11-1} = M_o + M_{(24)}. \tag{B.22}$$

$$N_{01-1} = M_o + M_{(12)}. \tag{B.23}$$

$$N_{11-1} = M_o + M_{(23)}. \tag{B.24}$$

$$N_{-110} = M_o + M_{(14)}. \tag{B.25}$$

$$N_{010} = M_o + M_{(12)} + M_{(14)} + M_{(24)} + M_{(124)}. \tag{B.26}$$

$$N_{110} = M_o + M_{(23)} + M_{(14)} + M_{(14)(23)}. \tag{B.27}$$

$$N_{-111} = M_o + M_{(34)}. \tag{B.28}$$

$$N_{011} = M_o + M_{(12)} + M_{(34)} + M_{(12)(34)}. \tag{B.29}$$

$$N_{111} = M_o + M_{(23)} + M_{(34)} + M_{(24)} + M_{(234)}. \tag{B.30}$$

Summarizing Eqs. (B.4) to (B.30), then Eqs. (B.31) to (B.44) are obtained.

$$\left(N_{-1-1-1} + N_{111}\right)/2 = M_0 + M_{(23)} + M_{(34)} + M_{(24)} + M_{(234)}. \tag{B.31}$$

$$\left(N_{0-1-1} + N_{011}\right)/2 = M_0 + M_{(12)} + M_{(34)} + M_{(12)(34)}. \tag{B.32}$$

$$\left(N_{1-1-1} + N_{-111}\right)/2 = M_0 + M_{(34)}. \tag{B.33}$$

$$\left(N_{-1-10} + N_{110}\right)/2 = M_0 + M_{(23)} + M_{(14)} + M_{(14)(23)}. \tag{B.34}$$

$$\left(N_{0-10} + N_{010}\right)/2 = M_0 + M_{(12)} + M_{(14)} + M_{(24)} + M_{(124)}. \tag{B.35}$$

$$\left(N_{1-10} + N_{-110}\right)/2 = M_0 + M_{(14)}. \tag{B.36}$$

$$\left(N_{-1-11} + N_{11-1}\right)/2 = M_0 + M_{(23)}. \tag{B.37}$$

$$\left(N_{0-11}+N_{01-1}\right)/2=M_0+M_{(12)}. \tag{B.38}$$

$$\left(N_{1-11}+N_{-11-1}\right)/2=M_0+M_{(24)}. \tag{B.39}$$

$$\left(N_{-10-1}+N_{101}\right)/2=M_0+M_{(13)}+M_{(24)}+M_{(13)(24)}. \tag{B.40}$$

$$\left(N_{00-1}+N_{001}\right)/2=M_0+M_{(12)}+M_{(23)}+M_{(13)}+M_{(123)}. \tag{B.41}$$

$$\left(N_{10-1}+N_{-101}\right)/2=M_0+M_{(13)}. \tag{B.42}$$

$$\left(N_{-100}+N_{100}\right)/2=M_0+M_{(34)}+M_{(13)}+M_{(14)}+M_{(134)}. \tag{B.43}$$

$$\begin{aligned}N_{000}=M_0&+M_{(12)}+M_{(23)}+M_{(34)}+M_{(13)}+M_{(14)}+M_{(24)}\\&+M_{(12)(34)}+M_{(13)(24)}+M_{(14)(23)}\\&+M_{(123)}+M_{(234)}+M_{(134)}+M_{(124)}\\&+M_{(1234)}.\end{aligned} \tag{B.44}$$

$M_{(1234)}$ represents the complete random events where four detectors have signals simultaneously, but not the true events like proton penetration. Solve Eqs. (B.31) to (B.44), then $M_{(1234)}$ obtained below,

$$\begin{aligned}M_{(1234)}=&N_{(000)}-\frac{1}{2}\cdot\left(N_{-1-1-1}+N_{111}\right)\\&-\frac{1}{2}\cdot\left(N_{0-1-1}+N_{011}\right)-\frac{1}{2}\cdot\left(N_{-1-10}+N_{110}\right)\\&-\frac{1}{2}\cdot\left(N_{0-10}+N_{010}\right)-\frac{1}{2}\cdot\left(N_{-10-1}+N_{101}\right)\\&-\frac{1}{2}\cdot\left(N_{00-1}+N_{001}\right)-\frac{1}{2}\cdot\left(N_{-100}+N_{100}\right)\\&+\left(N_{1-1-1}+N_{-111}\right)+\left(N_{1-10}+N_{-110}\right)+\left(N_{-1-11}+N_{11-1}\right)\\&+\left(N_{0-11}+N_{01-1}\right)+\left(N_{1-11}+N_{-11-1}\right)+\left(N_{10-1}+N_{-101}\right)-6\cdot M_0.\end{aligned} \tag{B.45}$$

Here, $M_{(1234)}$ is the number of the event after the background subtraction. $N_{(000)}$ includes both true signals and the accidental coincidence events (= background), which had the same timing difference of T2', T3', and T4 within $-t$ to t. Other terms on the right side of Eq. (B.45) represent accidental coincidence events.

Taking the measurement of $E_d = 1.6$ MeV at 45° as an example, the analysis results of the background subtraction are shown below. Table B.2 shows the event numbers for each timing gate.

Table B.2: The event numbers of each timing gates.

Gate types	Event number
N_{-1-1-1}	23
N_{0-1-1}	0
N_{1-1-1}	0
N_{-1-10}	1
N_{0-10}	1
N_{1-10}	0
N_{-1-11}	0
N_{0-11}	0
N_{1-11}	0
N_{-10-1}	0
N_{00-1}	2
N_{10-1}	0
N_{-100}	0
N_{000}	262
N_{100}	1
N_{-101}	0
N_{001}	6
N_{101}	2
N_{-11-1}	0
N_{01-1}	0
N_{11-1}	0
N_{-110}	0
N_{010}	1
N_{110}	0
N_{-111}	1
N_{011}	0
N_{111}	17

By substituting the number of events at each timing gate shown in Table B.2 into Eq. (B.45), the number of events after background subtraction was obtained. The accidental coincidence event rate was 10%. The main sources of accidental coincidence events were low-energy electrons. By using energy information, background subtraction processing was applied only to the proton locus (proton events from the $^{7}\mathrm{Be}(d,p)^{8}\mathrm{Be}$ reaction), and the accidental coincidence events for proton events were less than 3%.

Bibliography

[1] S. Hou *et al.*, *Physical Review C* **91**, no. 5, 055802, (2015).

[2] R. Kavanagh, *Nuclear Physics* **18**, pp. 492–501, (1960).

[3] C. Angulo *et al.*, *The Astrophysical Journal* **630**, no. 2, L105, (2005).

[4] N. Rijal *et al.*, *Physical Review Letters* **122**, no. 18, 182701, (2019).

[5] E. Hubble, *Proceedings of the national academy of sciences* **15**, no. 3, pp. 168–173, (1929).

[6] G. Gamow, *Reviews of Modern Physics* **21**, no. 3, 367, (1949).

[7] C. O'Raifeartaigh and S. Mitton, *arXiv preprint arXiv:1506.01651* (2015).

[8] A. Penzias and R. Wilson, *The Astrophysical Journal* **142**, 419, (1965).

[9] D. Fixsen *et al.*, *The Astrophysical Journal, Part 1 (ISSN 0004-637X), vol. 420, no. 2, p. 445-449* **420**, pp. 445–449, (1994).

[10] D. Fixsen *et al.*, *The Astrophysical Journal* **473**, no. 2, 576, (1996).

[11] F.-K. Thielemann *et al.*, *Nuclear Physics A* **570**, no. 1-2, pp. 329–343, (1994).

[12] G. J. Mathews *et al.*, *The Astrophysical Journal* **727**, no. 1, 10, (2010).

[13] E. Aver *et al.*, *Journal of Cosmology and Astroparticle Physics* **2012**, no. 04, 004, (2012).

[14] E. Aver *et al.*, *Journal of Cosmology and Astroparticle Physics* **2015**, no. 07, 011, (2015).

[15] Y. Izotov *et al.*, *Astronomy & Astrophysics* **558**, A57, (2013).

[16] Y. I. Izotov *et al.*, *Monthly Notices of the Royal Astronomical Society* **445**, no. 1, pp. 778–793, (2014).

[17] R. H. Cyburt *et al.*, *Reviews of Modern Physics* **88**, no. 1, 015004, (2016).

[18] M. Pettini and R. Cooke, *Monthly Notices of the Royal Astronomical Society* **425**, no. 4, pp. 2477–2486, (2012).

[19] F. Spite and M. Spite, *Astronomy and Astrophysics, vol. 115, no. 2, Nov. 1982, p. 357-366. Research supported by the Centre National de la Recherche Scientifique.* **115**, pp. 357–366, (1982).

[20] L. Sbordone *et al.*, *Astronomy & astrophysics* **522**, A26, (2010).

[21] M. Asplund *et al.*, *The Astrophysical Journal* **644**, no. 1, 229, (2006).

[22] D. N. Spergel *et al.*, *The astrophysical journal supplement series* **170**, no. 2, 377, (2007).

[23] P. Ade *et al.*, *Astronomy & Astrophysics/Astronomie et Astrophysique* **594**, (2016).

[24] A. Coc, *Journal of Physics: Conference Series*, vol. 665, 012001, IOP Publishing, (2016).

[25] R. H. Cyburt *et al.*, *Journal of Cosmology and Astroparticle Physics* **2008**, no. 11, 012, (2008).

[26] F. Kondev *et al.*, *Chinese Physics C* **45**, no. 3, 030001, (2021).

[27] M. Barbagallo *et al.*, *Physical review letters* **117**, no. 15, 152701, (2016).

[28] T. Kawabata *et al.*, *Physical review letters* **118**, no. 5, 052701, (2017).

[29] L. Damone *et al.*, *Physical review letters* **121**, no. 4, 042701, (2018).

[30] S. Hayakawa *et al.*, *The Astrophysical Journal Letters* **915**, no. 1, L13, (2021).

[31] I. Y. Barit *et al.*, *Journal of radioanalytical and nuclear chemistry* **97**, pp. 97–105, (1986).

[32] K. Sekharan *et al.*, *Nuclear Instruments and Methods* **133**, no. 2, pp. 253–257, (1976).

[33] A. Taniike *et al.*, *Plasma and Fusion Research* **8**, pp. 2401087–2401087, (2013).

[34] A. Hermanne *et al.*, *Applied Radiation and Isotopes* **70**, no. 12, pp. 2763–2772, (2012).

[35] F. Kondev and S. Naimi, *Chinese Physics C* **41**, no. 3, 030003, (2017).

[36] C. E. Rolfs and W. S. Rodney, *Cauldrons in the Cosmos: Nuclear astrophysics*. University of Chicago press, (1988).

[37] H. Weick *et al.*, *GSI Scientific Report* pp. 2018–1, (2017).

[38] J. F. ZIEGLER and J. P. BIERSACK, *Treatise on Heavy-Ion Science: Volume 6: Astrophysics, Chemistry, and Condensed Matter* 95, (1985).

[39] A. Coc and B. Davids, *arXiv preprint arXiv:1912.03933* (2019).

List of Figures

List of Tables